METAL-RICH

MAGNETOCALORIC PHASES

METAL-RICH
MAGNETOCALORIC PHASES

By

VOLODYMYR SVITLYK, B.Sc., M.Sc.

A Thesis

Submitted to the School of Graduate Studies

in Partial Fulfilment of the Requirements

for the Degree

Doctor of Philosophy

McMaster University

DOCTOR OF PHILOSOPHY (2010) McMaster University

(Chemistry) Hamilton, Ontario

TITLE: Metal-Rich Magnetocaloric Phases

AUTHOR: Volodymyr Svitlyk, B.Sc., M.Sc.

(Ivan Franko National University of Lviv, Lviv, Ukraine)

SUPERVISOR: Professor Y. Mozharivskyj

NUMBER OF PAGES: xviii, 182

Abstract

New metal-rich Gd_5T_4 magnetocaloric phases (T – p-element) were designed, synthesized and characterized. These phases exhibit a close relationship between the valence electron count, size effect, crystal structure and physical properties. The targeted cleavage of the interslab T-T dimers was achieved in the $Gd_5Si_{4-x}P_x$, $Gd_5Si_{4-x}Sb_x$ and $Gd_5Si_{4-x}Bi_x$ systems. While in the $Gd_5Si_{4-x}P_x$ system only a change in the valence electron count was employed for the desired structural transformations, in the $Gd_5Si_{4-x}Sb_x$ and $Gd_5Si_{4-x}Bi_x$ systems both the valence electron count and size effect were used to break the interslab dimers. Incorporation of large Bi atoms into the Gd_5Si_4 phase resulted in the complete cleavage of the interslab T-T bonds and lead to novel slab stacking sequences accompanied by stacking faults.

The $Gd_5Si_{4-x}P_x$ and $Gd_5Si_{4-x}Sb_x$ phases undergo ferromagnetic transitions within a wide temperature range. Values of the corresponding magnetic entropy changes indicate the presence of a conventional magnetocaloric effect. This is likely due to the temperature stability of the structures with the broken dimers which hinders first-order coupled magnetostructural transitions.

Metal-rich ferromagnetic phases of the $RE_5Ni_xT_{3-x}$ composition with RE = Gd, Dy, Lu, T = Sb, Bi were derived from the parent RE_5T_3 binaries. Incorporation of nickel stabilizes the orthorhombic Yb_5Sb_3-type structures at 800 °C. The $Gd_5Ni_{0.96}Sb_{2.04}$, $Gd_5Ni_{0.71}Bi_{2.29}$ and $Dy_5Ni_{0.66}Bi_{2.34}$ phases show relatively low values of magnetocaloric effect.

Acknowledgements

I thank my supervisor Dr. Yurij Mozharivskyj for his great help and teaching. I acknowledge my committee members Dr. Jacques Barbier and Dr. John Greedan for useful discussions. I thank my group members Janice Cheung, Peng Wang and Scott Forbes. I thank McMaster University, BIMR and collaborators.

Finally I thank my family for support and encouragement.

Table of Contents

List of Tables

List of Figures

Chapter 1. Introduction

1.1 Magnetism

1.1.1 Phenomena of magnetism

Magnetism is a property intrinsic to all materials. It exhibits itself during an interaction of matter with a special medium called a magnetic field. There are plenty of natural sources of magnetic fields, with our planet Earth being one of them. While Earth's magnetic field is considered to be relatively weak, the planet possesses other, much stronger local sources of it, such as the magnetite ores.

Different types of interactions of materials with a magnetic field are indicative of various macroscopic magnetic states of matter. For instance, a magnetic field attracts iron metal, in contrast to copper metal, which appears to be magnetically benign. To understand the macroscopic magnetic behavior of a system, the microscopic origin of the magnetism has to be known.

All substances consist of atoms, which in turn are built of nuclei with electrons orbiting around them. Although both species contribute to the magnetism, the nuclear contribution to the total magnetic response is negligible. In most cases, including this work, electrons are viewed as the only source of magnetism in matter.

1.1.2 Magnetic poles and magnetic field

The pivoting bar of a magnetic material (i.e. magnetite), which is commonly called a bar magnet, orients itself along the Earth's meridian. The side of the bar magnet pointing towards the geographic North Pole is called the north-seeking pole or the north

pole. Correspondingly, the opposite side of the magnet is called the south pole. Following this notation, the magnetic field, which can be represented as magnetic lines, is set to originate from the north pole of the magnet and flow towards the south pole (Fig. 1.1.1).

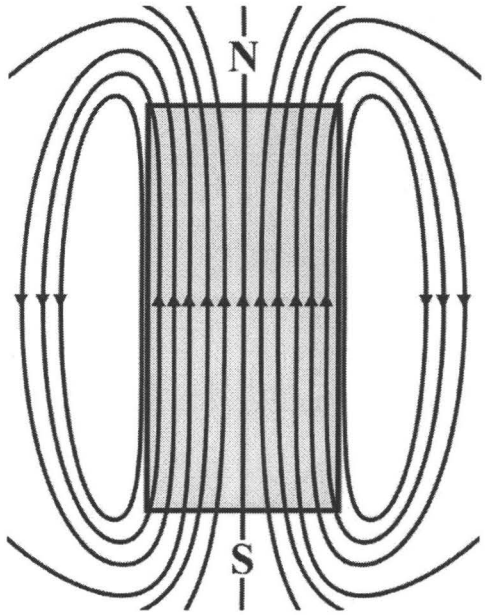

Figure 1.1.1. Magnetic lines propagating from the north to the south pole of a bar magnet

This shape of magnetic lines can be easily verified experimentally. By exposing a layer of tiny iron metal needles to a magnetic field generated by a bar magnet, they orient themselves in a manner shown in Figure 1.1.1.

The north and south poles of the magnet exert force on each other. This force is proportional to the product of the pole strengths, p, and inversely proportional to the square of the interpolar distance, r:

$$F = \frac{p_1 p_2}{4\pi\mu_0 r^2} \tag{1.1.1}$$

where μ_0 is the permeability of free space.

It is easy to see, that the magnetic field, H, generated by the pole p_1 is equal to

$$H = \frac{p_1}{4\pi\mu_0 r^2} \tag{1.1.2}$$

therefore the force, F, which is exerted by pole p_1 on p_2 is

$$F = Hp_2 \tag{1.1.3}$$

It is possible to generate a magnetic field without magnetic materials. One such method is to run an electric current through a wire. According to Ampère's law, a field H generated at a distance r from an infinite wire with a running current I is

$$H = \frac{I}{2\pi r}. \tag{1.1.4}$$

The unit of magnetic field strength in SI (Système International) is a direct derivative of this equation and is equal to the amperes per meter (A/m). However, the more commonly used unit is Oe (CGS system).

1.1.3 Macroscopic magnetic moment, magnetization and induction

If a bar magnet is placed in a magnetic field H at an angle θ to its direction (Fig. 1.1.2), the forces acting on the poles of the magnet are equal to $F = pH$ (eq. 1.1.3).

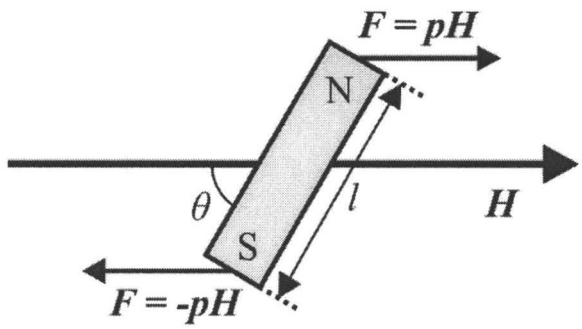

Figure 1.1.2. Forces acting on a bar magnet in a magnetic field

The torque exerted on the bar magnet is equal to

$$pH\frac{l}{2}sin\theta \; + \; pH\frac{l}{2}sin\theta \; = \; pHlsin\theta = mHsin\theta \tag{1.1.5}$$

where $m = pl$ is the magnetic moment. When the size of the magnet is reduced to the limit of a small length, but with a finite moment, its magnetic moment m is called a magnetic dipole. The energy of a magnetic moment/dipole in a magnetic field H is the negative dot product of the m and H vectors:

$$E = -\mu_0 \boldsymbol{m} \cdot \boldsymbol{H}. \tag{1.1.6}$$

Magnetic materials, e.g. bulk magnets, can be viewed as being composed of many tiny magnets or magnetic moments.

The magnetization of a material is the sum of all its magnetic moment vectors $\boldsymbol{m}$

$$\boldsymbol{M} = \sum \boldsymbol{m}. \tag{1.1.7}$$

The SI unit of magnetization is the same as for magnetic field (A/m). Again, the most commonly used unit is *emu* from the CGS system. Usually, magnetization is normalized to the quantity of a material, i.e. number of moles or mass. In the latter case, magnetization has units of emu/g.

Upon application of a magnetic field on a system with randomly oriented magnetic moments, they decrease their magnetic energy by aligning in the direction of the field (eq. 1.1.6). The total response of the material to the applied field includes induced magnetization, $\boldsymbol{M}$, and applied field, $\boldsymbol{H}$, and is called magnetic induction $\boldsymbol{B}$:

$$\boldsymbol{B} = \mu_0(\boldsymbol{H} + \boldsymbol{M}) \tag{1.1.8}$$

in SI units.

1.1.4 Magnetic susceptibility and basic magnetic states

The response of the magnetization of a material to an applied external field is called magnetic susceptibility, χ:

$$\chi = \frac{M}{H} \tag{1.1.9}$$

It can have either a positive or negative sign. In the latter case, the material is said to have a diamagnetic behaviour. This indicates that the system does not possess free magnetic moments, i.e. no unpaired electrons. Since every substance has core energy shells with all electrons being paired, a phenomenon of diamagnetism is intrinsic to all materials (except atomic Hydrogen). Diamagnetism emerges due to the induced currents, which generates a magnetic field opposing the external field (Lenz's law).

When a system possesses free magnetic moments, i.e. unpaired electrons, magnetic susceptibility is positive. Four distinct basic magnetic states are possible in this case: paramagnetic, ferromagnetic, antiferromagnetic and ferrimagnetic (Fig. 1.1.3).

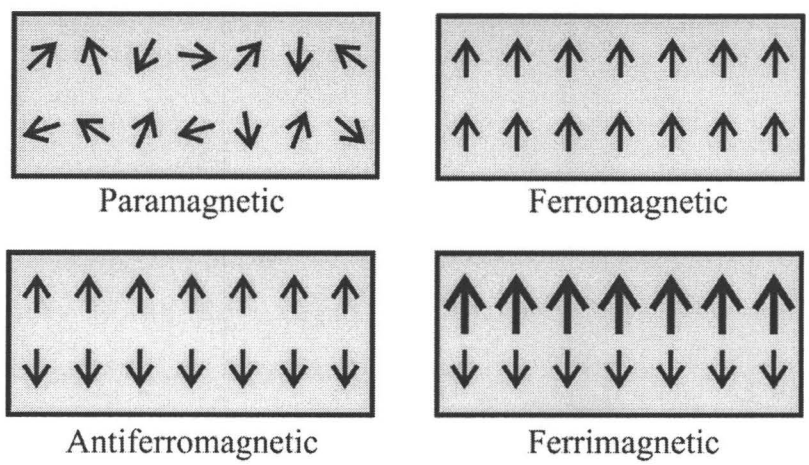

Figure 1.1.3. Basic magnetic states with positive susceptibility

Here, magnetic moments are represented by arrows, whose relative directions and magnitudes are assumed to represent those of the magnetic moments in a material. This notation will be followed further.

Paramagnetism is a state with all magnetic moments randomly oriented (Fig. 1.1.3, top left). All materials with positive magnetic susceptibility, χ, are paramagnets either throughout all temperatures (Na, Al, Sc) or at higher temperatures. Upon cooling, many paramagnetic phases can undergo magnetic ordering. If all moments are aligned along one direction (Fig. 1.1.3, top right), this state is called ferromagnetic (Fe, Co, Ni,[1] Gd,[2] $SmCo_5$,[3] $Nd_2Fe_{14}B$[4]). The corresponding ordering temperature is called Curie temperature, T_c. The magnetic susceptibility of ferromagnetic materials is several orders higher than that of paramagnets. If moments of the same magnitude are aligned anti-parallel (Fig. 1.1.3, bottom left), the material is called an antiferromagnet with the Neel temperature, T_N, as an ordering temperature (Cr, Mn,[5] MnO[6], FeO[7]). The susceptibility values of antiferromagnetic materials are similar to those of paramagnetic materials and it arises due to tilting and flipping of magnetic moments along the direction of the applied field. When moments are anti-parallel but their magnitudes differ (Fig. 1.1.3, bottom right), the corresponding magnetic state is called ferrimagnetic (magnetite Fe_3O_4[8]). Qualitative and quantitative behaviours of ferrimagnetic materials are similar to those of ferromagnetic phases.

There exist many other magnetic states, like canted, sinusoidal/cosinusoidal, helicoidal etc. However, they are less common than the above mentioned states and are not of a significant interest to the subject of the magnetocaloric effect.

1.1.5 Microscopic origin of magnetism

Electrons are the carriers of magnetism. They contribute through their orbiting (orbital momentum) and spinning (spin momentum) motions (Fig. 1.1.4).

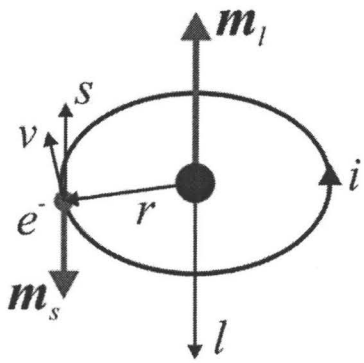

Figure 1.1.4. Angular orbital (l) and spin (s) momenta of the electron and associated magnetic moments $\boldsymbol{m}_l$ and $\boldsymbol{m}_s$. Orbiting radius denoted as r, speed as v, current as i

From a classical point of view, the orbital motion of an electron generates a magnetic moment

$$\boldsymbol{m}_l = IA \tag{1.1.10}$$

where I is the current and A is the area of the orbit. It is easy to see, that it is equal to

$$\boldsymbol{m}_l = -\frac{1}{2}evr \tag{1.1.11}$$

where e is the charge of an electron, v is its speed and r is the orbiting radius, i.e. distance from the nucleus to the electron. In classical physics, the angular momentum of motion is analogous to the linear momentum $L = mv$ of motion and is equal to $L = mvr$, where m is the mass. Therefore, the magnetic moment originating from the orbital angular momentum is

$$\boldsymbol{m}_l = -\frac{e}{2m}\boldsymbol{l} \tag{1.1.12}$$

Contrary to the classical physics, in real, i.e. microscopic world of electrons, the orbital angular momentum can take only certain orientations about the magnetic field. The quantized projection of the angular momentum onto the field axis can be written as $m_l\hbar$, resulting in the angular momentum magnetic moment, $\boldsymbol{m}_l$, to be equal to

$$\boldsymbol{m}_l = -\frac{e\hbar}{2m}m_l \tag{1.1.13}$$

where m_l is the orbital magnetic quantum number and ħ is the Dirac constant. The $e\hbar/2m$ constant is called the Bohr magneton, μ_B, and is the elementary unit of magnetic moment. The effective or total orbital contribution to the magnetic moment is

$$\boldsymbol{m}_l = -\mu_B\sqrt{l(l+1)} \tag{1.1.14}$$

where l is the orbital quantum number. Taking into account the contribution of the electron spin, the total effective magnetic moment is

$$\boldsymbol{m} = -\,g_j\mu_B\sqrt{j(j+1)} \tag{1.1.15}$$

where j is the total quantum number, which accounts for the spin-orbital contribution and g_j is the Lande splitting factor.

1.1.6 Theory of paramagnetism

When a paramagnetic material is exposed to an external magnetic field, its moments tend to align along the field direction to reduce their magnetic energy $E = -\mu_0\boldsymbol{m}\cdot\boldsymbol{H}$ (eq. 1.1.6). The moment of atoms along the magnetic field is equal to $\boldsymbol{m} = -\,g_J\mu_B J$, and the resulting energy of the electrons becomes

$$E = -\mu_0 g_J \mu_B J \cdot \boldsymbol{H}. \tag{1.1.16}$$

If orbital contribution is ignored, J = S. Spins in an external magnetic field precess around its direction (Larmor precession) and orient themselves in two ways with respect to the field – up and down. We denote these states of an electron by the corresponding spin quantum numbers, m_s: +1/2 and –1/2, respectfully (Fig. 1.1.5).

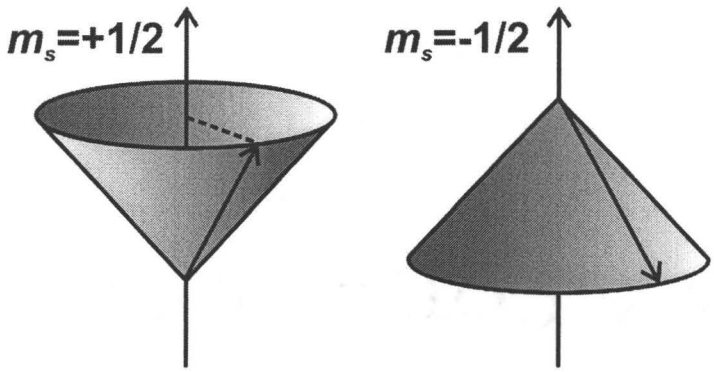

Figure 1.1.5. Precession of magnetic spins along the field (left) and in the opposite direction (right)

However, thermal energy prevents all moments from orienting along the field direction and the resulting equation for magnetization takes the form of

$$M = N g_J J \mu_B B_J \left(\frac{g_J J \mu_B \mu_0 H}{k_B T} \right) \tag{1.1.17}$$

where B_J is a Brillouin function:

$$B_J(x) = \left(\frac{2J+1}{2J} \right) \coth\left(\frac{(2J+1)x}{2J} \right) - \left(\frac{1}{2J} \right) \coth\left(\frac{x}{2J} \right). \tag{1.1.18}$$

When $\frac{\mu_0 m H}{k_B T} << 1$, the effective magnetization is equal to

$$M = \frac{N\mu_0 m^2 H}{3k_B T} = \frac{N\mu_0 g_J^2 \mu_B^2 J(J+1)H}{3k_B T}. \quad (1.1.19)$$

The corresponding magnetic susceptibility is

$$\chi = \frac{M}{H} = \frac{N\mu_0 g_J^2 \mu_B^2 J(J+1)}{3k_B T} = \frac{C}{T} \quad (1.1.20)$$

which is a Curie law with

$$C = \frac{N\mu_0 g_J^2 \mu_B^2 J(J+1)}{3k_B} \quad (1.1.21)$$

The classical counterpart of eq. 1.1.21 is obtained when $J = \infty$ resulting in

$$M = Nm\left[\coth\left(\frac{mH}{k_B T}\right) - \frac{k_B T}{mH}\right] = NmL(\alpha) \quad (1.1.22)$$

where $L(\alpha) = \coth(\alpha) - 1/\alpha$ is the Langevin function with $\alpha = \frac{mH}{k_B T}$.

1.1.7 Theory of ferromagnetism

Magnetocaloric effect has the largest values around ferromagnetic transitions. Ordered magnetic states, including ferromagnetic, emerge through the exchange coupling of magnetic moments. The total Hamiltonian of this coupling (ignoring orbital contribution) can be written as

$$\langle H \rangle = -2\boldsymbol{J}_{ij}\boldsymbol{s}_i \cdot \boldsymbol{s}_j \quad (1.1.23)$$

where $\boldsymbol{s}_i$ and $\boldsymbol{s}_j$ represent spins of atoms i and j and $\boldsymbol{J}_{ij}$ is the exchange coupling constant. A positive sign of $\boldsymbol{J}_{ij}$ indicates a ferromagnetic type of interaction, negative –

antiferromagnetic. Now, the magnetic energy of the electrons of a ferromagnetic material in an external magnetic field is equal to

$$E = -\mu_0 g_J \mu_B J \cdot (\boldsymbol{H} + \alpha M') \tag{1.1.24}$$

where $\alpha M'$ is a field acting on the electron created by its neighbouring electrons. Magnetization is now equal to

$$M = N g_J J \mu_B B_J \left(\frac{g_J J \mu_B \mu_0 (H + \alpha M')}{k_B T} \right) \tag{1.1.25}$$

where B_J is a Brillouin function.

Paramagnetic susceptibility of ferromagnetic materials is described by the Curie-Weiss law

$$\chi = \frac{C}{T - \theta} \tag{1.1.26}$$

where θ is the Weiss temperature.

In magnetic systems based on rare-earth elements, which will be considered here, magnetic moments originate from the localized 4*f*-electrons and exchange interactions are mediated by the conduction electrons. This often induces polarization of the conduction electrons and an increase in the calculated effective magnetic moment per magnetic atom.

1.2 Magnetocaloric effect

1.2.1 Conventional magnetocaloric effect

The magnetocaloric effect (MCE) was discovered by Warburg in 1880.[9] He applied a magnetic field on pure iron and noticed a rise in its temperature (Fig. 1.2.1). To understand the mechanism behind this phenomenon we have to model changes in a

magnetically active system induced by a magnetic field.

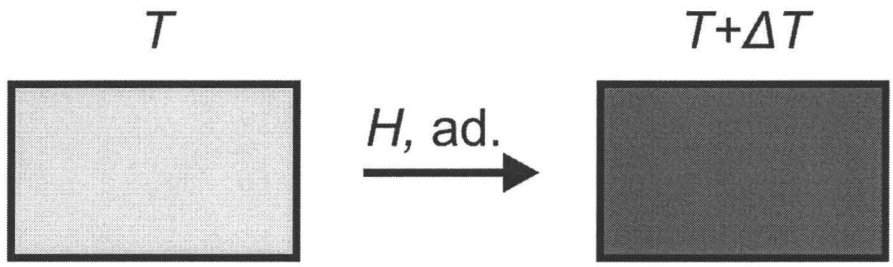

Fig. 1.2.1. Rise in temperature of iron upon application of magnetic field

Let's consider a system of four unpaired spins in a high-spin state. The total spin quantum number, S, for this system is equal to S = (1/2)n = 2, where n is the total number of spins. The number of possible states this system can adopt, Ω, is

$$\Omega = 2S + 1 \tag{1.2.1}$$

and equals to five (Fig. 1.2.2).

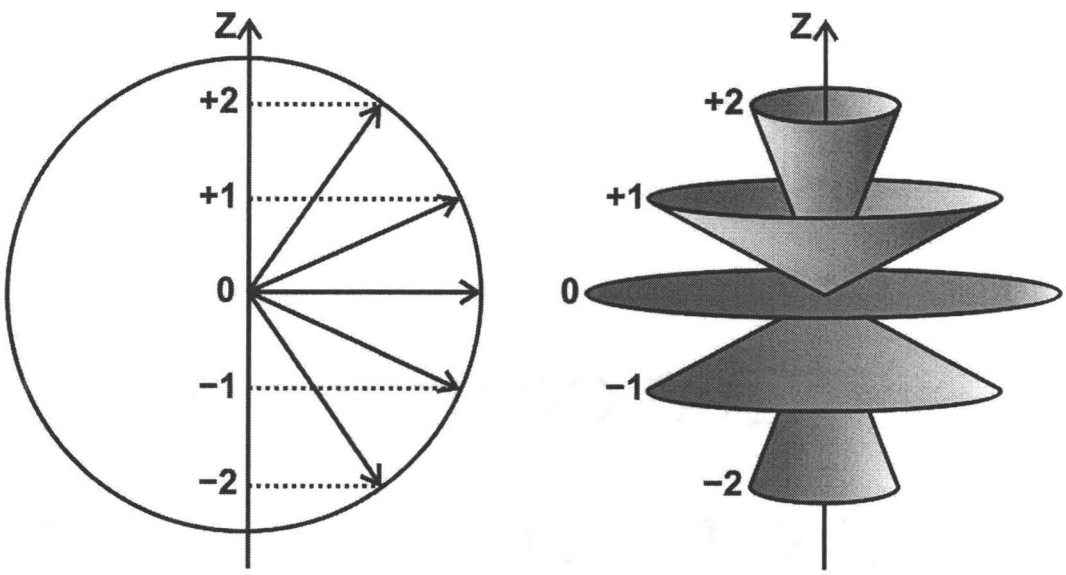

Fig. 1.2.2. Five possible states of the system with S = 2

The entropy of a system with a known number of possible states can be calculated using the Boltzmann equation

$$S = k_B \ln \Omega \tag{1.2.2}$$

where k_B is the Boltzmann constant. Therefore, the entropy of the system of magnetic spins can be written as

$$S = k_B \ln(2S+1) \tag{1.2.3}$$

and is called magnetic entropy. This equation takes the form of $S = R\ln(2S+1)$ if normalized to a mole of moments (R – universal gas constant).

To illustrate the influence of a magnetic field on the magnetic entropy, let's consider a system of randomly oriented (paramagnetic-like state) magnetic moments without a magnetic field (Fig. 1.2.3, left). As derived above, the entropy of such a system can be calculated using the $S_{mag} = R\ln(2S+1)$ relationship (only spin contributions to the magnetic moments are assumed here). If upon application of a magnetic field we obtain a perfect order (ferromagnetic-like state), i.e. the system adopts a state with all moments oriented along the field (Fig. 1.2.3, right), the entropy of such system is equal to $S_{mag} = k_b \ln \Omega = k_b \ln 1 = 0$. Therefore, the change in the magnetic entropy, ΔS_{mag}, upon this type of ordering is[10]

$$\Delta S_{mag} = -R\ln(2S+1) \tag{1.2.4}$$

If the field is applied adiabatically, the system heats up. This increase in temperature follows from the fact that entropy of solids consists of three parts: lattice (S_{lat}), electronic (S_{el}) and magnetic (S_{mag}). During an adiabatic process the total entropy change, ΔS, equals zero. Since S_{mag} decreases upon the application of a magnetic field,

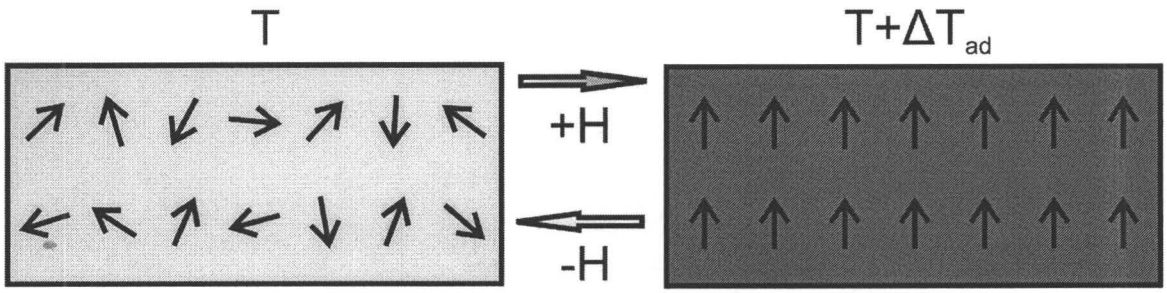

Fig. 1.2.3. Complete ordering of spins upon application of magnetic field

i.e. $\Delta S_{mag} < 0$, the sum of ΔS_{lat} and ΔS_{el} must be positive, i.e. $\Delta S_{lat} + \Delta S_{el} > 0$. The adiabatic temperature change, ΔT_{ab}, is related to the sum of ΔS_{lat} and ΔS_{el} through the $(\Delta S_{lat} + \Delta S_{el})T_{ad} = c_p \Delta T_{ad}$ equation, where c_p is the heat capacity. Since c_p is always positive, ΔT_{ad} must be positive as well, i.e. we observe an increase in the temperature of the system.

The mechanism described above represents the conventional MCE and is present in any material that has a positive magnetic response, i.e. positive susceptibility. Since ordering of magnetic moments lies at the origin of the MCE (as described above), it has the largest values for ferromagnetic materials around their ordering temperatures, T_c. For gadolinium metal, which orders around room temperature, ΔS_{mag} reaches -10 J/kg K at its magnetic transition.[2]

1.2.2 Giant magnetocaloric effect

The conventional MCE can be enhanced if a ferromagnetic transition is accompanied by a first-order structural transition. In this case the magnetic transition becomes first-order as well, and a first-order coupled magnetostructural transition

occurs.[11] Such transition yields much larger values of the entropy and/or temperature changes when compared to the conventional MCE and the resulting magnetocaloric response is called giant MCE. It is convenient to use entropy vs. temperature plots to describe the giant MCE (Fig. 1.2.4).

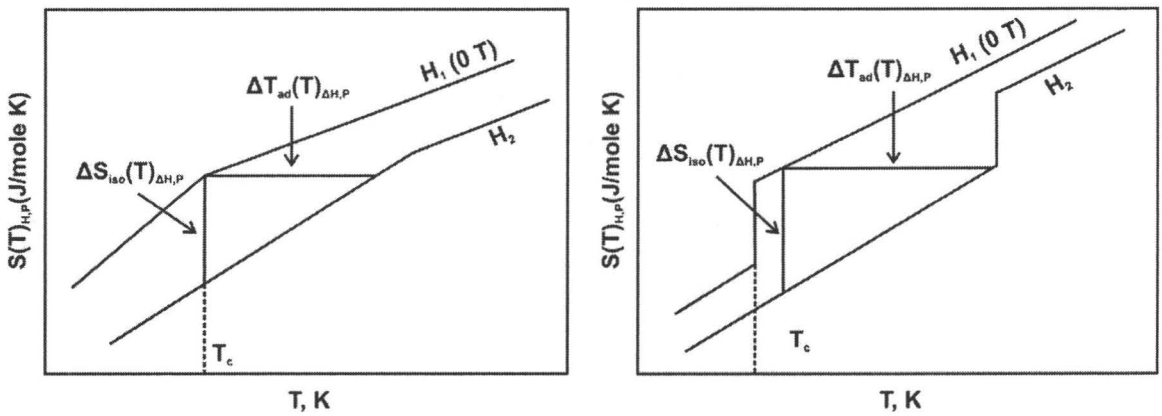

Figure 1.2.4. Entropy vs. temperature plots for conventional (left) and giant (right) MCEs. H_1 represents zero field; H_2 – applied field (arb. value); $\Delta S_{iso}(T)_{\Delta H,P}$ – isothermal entropy change for a field change of ΔH under constant pressure; $\Delta T_{ad}(T)_{\Delta H,P}$ – adiabatic temperature change for a field change of ΔH under constant pressure

During a first-order magnetostructural transition (Fig. 1.2.4, on the right), entropy changes discontinuously at the transition point. This results in enhanced values of ΔS and ΔT when compared to the values of a conventional MCE (Fig. 1.2.4, on the left). The equation for the total entropy change, ΔS, now consists of two parts – magnetic and structural:

$$\Delta S_{iso}(T)_{\Delta H,P} = S(T)_{H_2,P} - S(T)_{H_1,P} = \int_0^T \frac{[c(T)_{H_2} - c(T)_{H_1}]_P}{T} dT - \frac{\Delta E_{H_1}}{T_{t,H_1}} = \Delta S_{mag} - \frac{\Delta E_{H_1}}{T_{t,H_1}}$$

(eq. 1.2.5) where ΔS_{mag} is the magnetic entropy change; $c(T)$ – heat capacities; ΔE – enthalpy of structural transition; T_t – transition temperature. Correspondingly, a general formula for the total entropy change is

$$\Delta S = \Delta S_{mag} + \Delta S_{str} \tag{1.2.6}$$

The equation for the adiabatic temperature change, ΔT_{ad}, is the same both for the conventional and giant MCE:

$$\Delta T_{ad}(T)_{\Delta H,P} = -\frac{T_1}{c(T_1)_{H_2,P}} \Delta S_{iso}(T)_{\Delta H,P} \tag{1.2.7}$$

The adiabatic temperature change is larger for giant MCE since the corresponding entropy change, ΔS, is larger.

The giant MCE was discovered in 1997 in the monoclinic $Gd_5Si_2Ge_2$ phase,[12] which is a member of a large family of RE_5T_4 phases (RE – rare-earth element, T – p-element). The RE_5T_4 phases are built from $[RE_5T_4]$ slabs, which are interconnected through the T-T dimers. At this point, two structure types of the RE_5T_4 family have to be introduced: orthorhombic Gd_5Si_4-type, where all dimers are intact, i.e. all T-T bonds exist, and orthorhombic Sm_5Ge_4-type with all dimers broken (Fig. 1.2.5, on the left and on the right, respectively).[13]

The monoclinic modification of the $Gd_5Si_2Ge_2$ phase has half of the interslab T-T dimers broken, i.e. it can be viewed as an intermediate structure between Gd_5Si_4- and Sm_5Ge_4-types (Fig. 1.2.5, in the middle). At room temperature, monoclinic $Gd_5Si_2Ge_2$ is a paramagnet and transforms into a ferromagnetic Gd_5Si_4-type structure below 271 K. The application of a magnetic field on the monoclinic $Gd_5Si_2Ge_2$ phase in the vicinity of 271

K induces a first-order magnetostructural transition, i.e. reformation of all interslab *T*-*T* (Si/Ge-Si/Ge in this case) dimers and ferromagnetic ordering.[14] This results in giant values of MCE: ΔS = -36 J/kg K, ΔT = 17 K.[15]

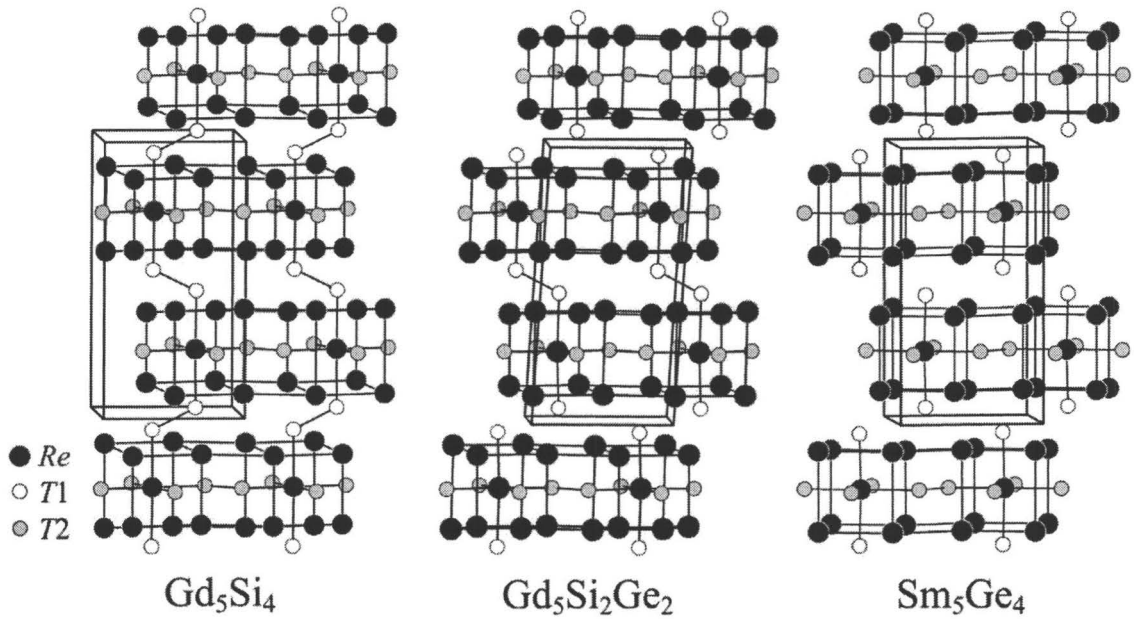

Figure 1.2.5. Gd_5Si_4- (left), $Gd_5Si_2Ge_2$- (middle) and Sm_5Ge_4-type structures

1.2.3 Magnetic refrigeration

The magnetocaloric effect can be used for magnetic refrigeration (Fig. 1.2.6, on the left). Its mechanism is analogous to a conventional vapor-pressure method (Fig. 1.2.6, on the right), which is commonly used today.

Let's consider a system of randomly oriented magnetic moments at an arbitrary ambient temperature *T* (Fig. 1.2.6, left-top). Upon an adiabatic application of magnetic field, *H*, the magnetic moments align along the field and the system heats up with a change of temperature ΔT_{ad} (Fig. 1.2.6, left-right). The mechanism behind this

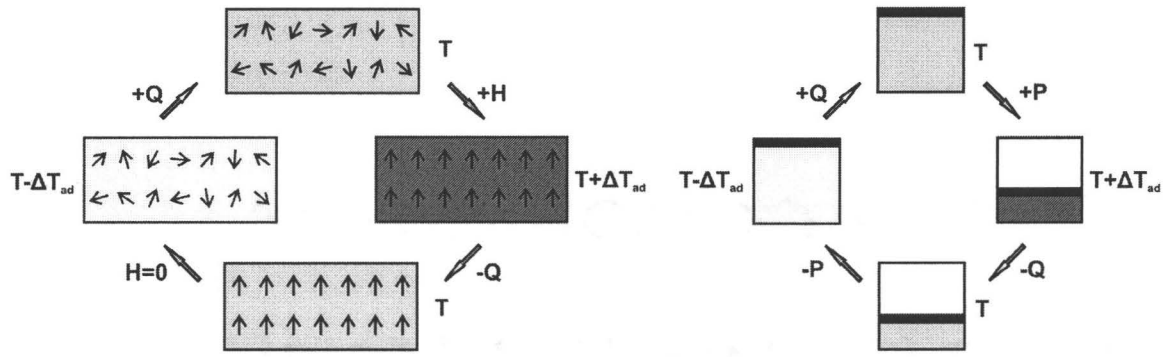

Figure 1.2.6. Magnetic (left) and vapor-pressure (right) cycles of refrigeration

temperature rise was described in Section 1.2.1. After the system is brought to the original temperature, T, with the applied field, H, on (Fig. 1.2.6, left-bottom), the subsequent adiabatic release of the field results in a temperature decrease $-\Delta T_{ad}$ (Fig. 1.2.6, left-left). Cooling occurs due to the increase in the magnetic entropy at the expense of the lattice and electronic entropies. Upon the heat exchange with a targeted object, i.e. a cooling process, the system returns to the original state with randomly oriented moments and temperature T (Fig. 1.2.6, left-top). Continuous cooling can be achieved by repeating this cycle.

The first experimental magnetic refrigeration unit based on gadolinium metal was built by the Astronautics Corporation of America, Milwaukee, USA jointly with the Ames Lab of DOE USA.[16] The efficiency of this kind of system is about 60%, while the efficiency of conventional vapour-pressure units is 30-40%. Beside this advantage, magnetic refrigeration is virtually noiseless, vibrationless and is environmentally friendly, since no ozone-depleting substances are employed (i.e. no chlorofluorocarbons).

No commercial magnetic refrigeration units that operate around room

temperatures are available to date. Many important aspects have to be addressed prior to implementation of this technique into a household.

1.2.4 Design of magnetic refrigeration materials for application around room temperatures

One of the most chemically and physically challenging tasks is to achieve large values of MCE under a small applied magnetic field. In practice, fields larger than 3 Tesla are accessible only with superconducting magnets. Apparently, superconducting magnets themselves require a large amount of energy to operate since a constant supply of liquid nitrogen/helium is required to maintain their superconducting state.

Since the MCE peaks around ferromagnetic transitions (section 1.2.1), a ferromagnetic ordering is a necessary requirement for a magnetocaloric phase. Therefore, a successful material must contain magnetically active 3*d*- and 4*f*-elements. The 4*f*-elements are expected to yield larger values of the magnetic entropy change, ΔS_{mag}, since ΔS_{mag} depends on the total quantum number J as

$$\Delta S_{mag} = -Rln(2J+1). \tag{1.2.8}$$

Besides this, 4*f*-elements have high thermal conductivity, which facilitates a heat exchange during a refrigeration cycle. Also, high densities of the rare-earth elements result in a larger cooling power in a smaller volume and lower lattice heat capacity per unit mass.

The above described concerns the optimization of a magnetic contribution to the total entropy change. A first-order structural transition has to be introduced together with

a magnetic transition to achieve a giant MCE (section 1.2.2). It is not an easy and straightforward task. Abrupt structural changes can be incorporated as a cleavage/formation of directional bonds, e.g. covalent ones, as it was done in the $Gd_5Si_2Ge_2$ phase. The *p*-block elements are particularly promising for this task.

Another important property of magnetocaloric materials is hysteresis. While hysteresis is an intrinsic phenomenon for phases that undergo first-order transformations, it significantly decreases the performance of a magnetic refrigerant. As the purity and homogeneity of a material increases, its hysteresis decreases.[17] In addition, homogeneity decrease the temperature span of the transition, i.e. making it sharper. This yields a greater response to the external magnetic field, resulting in higher values of MCE around the ordering temperature.

Besides the fundamental chemical and physical aspects of the MCE optimization described above, a number of engineering issues will have to be addressed. These are the chemical and mechanical stability of the refrigeration materials, environmental friendliness and a low cost.

References

[1] A. Paoletti, *Theory Condens. Matter, Lect. Int. Course, 4th* **1968,** 561-74.

[2] S. Dan'kov, A. Tishin, V. Pecharsky, K. Gschneidner Jr., *Phys. Rev. B: Condens. Matter Mater. Phys.* **1998**, *57*, 3478.

[3] K. Strnat, G. I. Hoffer, J. C. Olson, W. Ostertag, J. J. Becker, *J. Appl. Phys.* **1967**, *38*, 1001-1002.

[4] M. Sagawa, S. Fujimura, H. Yamamoto, Y. Matsuura, S. Hirosawa, *J. Appl.* Phys. **1985**, *57*, 4094-4096.

[5] C. G Shull, M. K. Wilkinson, *Rev. Mod. Phys.* **1953**, *25*, 100-107.

[6] M. E. Lines, E. D. Jones, *Phys. Rev.* **1965**, *139*, 1313-1327.

[7] F. B. Koch, M. E. Fine, *J. Appl. Phys.* **1967**, *38*, 1470-1471.

[8] S. Yamaguchi, *Z. Anorg. Allg. Chem.* **1962**, *314*, 222-225.

[9] E. Warburg, *Ann. Phys.* **1881**, *13*, 141.

[10] A. M. Tishin, Y. L. Spichkin, *The Magnetocaloric Effect and Its Applications, Institute of Physics Publishing, Bristol and Philadelphia*, **2003**.

[11] V. K. Pecharsky, K. A. Gschneidner Jr., A. O. Pecharsky, A. M. Tishin, *Phys. Rev. B: Condens. Matter Mater. Phys.* **2001**, *64*, 144406/144401-144406/144413.

[12] V. K. Pecharsky, K. A. Gschneidner Jr., *Phys. Rev. Lett.* **1997**, *78*, 4494-4497.

[13] V. Svitlyk, G. J. Miller, Y. Mozharivskyj, *J. Am. Chem. Soc.* **2009**, *131*, 2367-2374.

[14] W. Choe, V. K. Pecharsky, A. O. Pecharsky, K. A. Gschneidner Jr., V. G. Young Jr., G. J.Miller, *Phys. Rev. Lett.* **2000**, *84*, 4617-4620.

[15] A. O. Pecharsky, K. A. Gschneidner, V. K. Pecharsky, *J. Appl. Phys.* **2003**, *93*, 4722-4728.

[16] C. Zimm et. al., *Adv. Cryog. Eng.* **1998**, *43*, 1759-1766.

[17] V. K. Pecharsky, K. A. Gschneidner, Y. Mudryk, D. Paudyal, *J. Magn. Magn. Mater.* **2009**, *321*, 3541-3547.

Chapter 2. Experimental X-ray diffraction techniques and crystal structure determination

2.1 Role of diffraction in solid-state research

The structure of a material is crucial to the understanding of all of its properties: chemical, physical, mechanical, electronic etc. Knowing the relationship between the structural features and properties allows for the targeted design of new materials with the desired functionality.

Determination of a structure requires different tools for different materials. For instance, structures of organic molecules can often be revealed by various spectroscopic methods. Solid-state crystalline materials, besides a short-range order intrinsic to organic molecules (interatomic bonds), possess a long-range order. This order can be represented as an infinite 3-dimentional network of atoms. While spectroscopy can determine the local arrangements of the atoms, it is not able to provide a global picture, i.e. how the building blocks (atoms, ions, molecules etc.) of a material are packed into the 3D structure.

Diffraction is a technique that allows for the determination both of short- and long-range structural arrangements. However, a structure obtained by means of diffraction is an average of all elementary building units of the compound. Although it does not affect fully ordered systems, this technique cannot provide a detailed picture for disordered phases. Nevertheless, it is a straightforward, easy to use technique which allows for quick and, in most cases, conclusive structural determinations.

2.2 Selection of the diffraction source

Diffraction is the coherent and elastic scattering of physical objects with wave-like properties upon an interaction with a periodic material. It can take place only when the wavelength of the radiation is commensurate with the periodicity of the studied system. Solid-state chemistry deals with atomic-scale structures with typical distances of about 2-4 Å. Electromagnetic waves which correspond to this wavelength are known as hard X-rays. Since microscopic particles exhibit wave-particle duality, they can be employed for diffraction experiments as well. Commonly used particles with wavelengths matching atomic-scale dimensions are neutrons.

Due to the diverse nature of X-rays and neutrons, the physics of their interactions with matter is different. X-rays are scattered by the electron clouds of atoms while neutrons are scattered by their nuclei. Additionally, neutrons interact with the magnetic moments of atoms, which makes possible the determination of the magnetic structure of a material.

Many factors have to be considered for the selection of the diffraction source. One of the most important is accessibility. While powerful X-ray beams can be generated in a conventional laboratory using compact X-ray tubes (See **Generation of X-rays in the laboratory environment** section), controlled neutron beams can be generated by nuclear fission reactions, i.e. inside a nuclear reactor, or using spallation sources. Another useful feature of laboratory X-rays is a much larger flux compared to neutron sources, which translates into smaller amounts of a sample needed for the experiment.

These factors make X-ray radiation the number one choice for structural studies. Neutron diffraction is usually employed to determine the magnetic structure of a material or for specific structural needs, such as light atom localization, distinguishing elements with similar electron densities or isotopes mapping.

2.3 Generation of X-rays in the laboratory environment

The most common laboratory sources of X-rays are sealed X-ray tubes (Fig. 2.1).

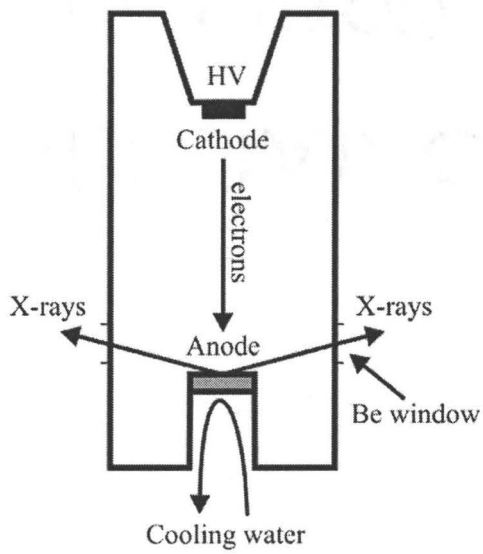

Figure 2.1. Scheme of the conventional sealed X-ray tube

Here, a high voltage (HV) of about 40 kV is applied to create an electric potential between the cathode and anode (Fig. 2.1). This generates a current of electrons from the heated cathode towards the anode in the evacuated tube. Upon contact with the anode, continuum (white) and characteristic radiations are generated (Fig. 2.2).

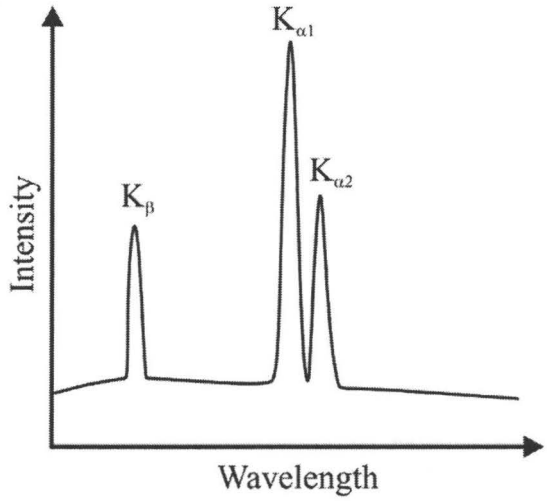

Figure 2.2. Continuum spectra of X-rays with three characteristic lines

Continuum spectra (background) results from the energy loss of the accelerated electrons upon contact with the anode. Characteristic signals with much stronger intensities arise from the excitations of the inner shell electrons of the anode material. Therefore, by varying the anode material, wavelengths of the characteristic X-rays can be changed. The most common anode elements are Cr, Fe, Co, Cu, Mo, Ag and others.

Generated X-rays travel from the anode to the instrumental optics through beryllium windows (Fig. 2.1). Characteristic wavelength is singled-out by monochromatization of white beam through the diffraction on a single crystal oriented in a specific way. Although this dramatically decreases the total photon flux, it provides higher resolution data. Resultant monoenergy X-rays are collimated and focused on the sample.

The performance of X-ray tubes can be enhanced by introduction of rotating anodes. The latter can handle much higher electron currents without overheating, which

results in more powerful X-ray beams.

2.4 Scattering of X-rays by atoms and the diffraction laws

X-rays as electromagnetic waves have electric and magnetic constituents. Upon contact with atoms, they interact with their electron clouds, causing them to oscillate with the same frequency as the electric field of the X-rays. In the case of elastic scattering, oscillating electrons generate electromagnetic radiation of the same frequency as the incident beam and scatter it in all directions. The intensity of the scattered beam depends on the phase differences of the travelling waves: they have the largest amplitude when waves travel in phase (constructive interference) and no intensity when waves travel out of phase (destructive interference).

Due to the large volume of the electron clouds (Fig. 2.3), phase differences of scattered waves depend on the scattering angle.

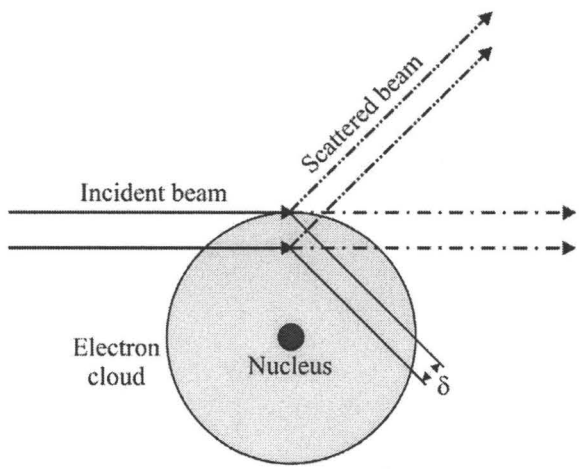

Figure 2.3. Path difference of scattered X-ray beam

While there is no difference in the path of forward scattered X-rays, any other scattering

direction has a path difference, δ, between the scattered waves which increases with the scattering angle. This results in the weakening of the scattered beam with increasing angle. The angular dependence of the radiation intensity scattered by the specific atom is described by its scattering factor *f*. In contrast to X-rays, neutrons are scattered on the nuclei, which are small and can be viewed as point objects. Consequently, there is a low decrease in the scattering intensity for neutrons with the increasing angle.

When X-rays interact with regular arrangements of atoms, i.e. crystal lattice, they scatter only in specific directions. This phenomenon is called diffraction and can be described by mathematical equations. The first diffraction conditions were given by Laue as a set of three equations, which have to be satisfied simultaneously:

$$\begin{aligned} a(\cos\alpha_1-\cos\beta_1) &= h\lambda \\ b(\cos\alpha_2-\cos\beta_2) &= k\lambda \\ a(\cos\alpha_3-\cos\beta_3) &= l\lambda \end{aligned} \tag{2.1}$$

where *a*, *b* and *c* are the cell parameters; α and β are the angle of incident and diffracted, respectively, beams with respect to the row of atoms in three independent directions; λ – wavelength; *h*, *k* and *l* are the Miller indices. The latter are integers that indicate the number of times a specific plane of atoms intersects the crystallographic unit cell of the crystalline solid along the *a*, *b* and *c* directions, respectively. Laue conditions are used to describe diffraction from the monocrystalline solids, i.e. single crystals.

Bulk structural analysis is usually performed on powder samples, which consist of many randomly oriented tiny crystallites. In this case it is convenient to use Bragg's law, which views scattering as a reflection from the atomic planes and has the form of

$$2d\sin\theta = n\lambda \tag{2.2}$$

where d is the distance between atomic planes; θ – angle of the incident and diffracted beam with respect to the atomic planes (Bragg angle); n – diffraction order. Bragg's law illustrates the condition for the constructive interference: diffraction occurs when the phase difference between the scattered waves is equal to an integer number of wavelengths $n\lambda$.

2.5 Reciprocal lattice, Ewald's sphere, structure factor and the Fourier transformation

Mathematical description of diffraction can be conveniently presented with the help of the reciprocal lattice concept, which was introduced to crystallography by Ewald. The reciprocal lattice is the analogue of the direct lattice of real space and is defined by three vectors

$$a^* = \frac{\boldsymbol{b}\mathbf{x}\boldsymbol{c}}{V}, b^* = \frac{\boldsymbol{a}\mathbf{x}\boldsymbol{c}}{V}, c^* = \frac{\boldsymbol{a}\mathbf{x}\boldsymbol{b}}{V} \tag{2.3}$$

where **x** stands for the vector product operator; V is the volume of the direct lattice. A reciprocal lattice vector d^* is inversely proportional to the corresponding direct space interplanar distance d

$$d^* = \frac{1}{d}. \tag{2.4}$$

Consider a two-dimensional reciprocal lattice and an incident wave of wavelength λ with the propagation vector $\boldsymbol{k}$ with an absolute value equal to 1/λ (Fig. 2.4). If the incident wave is scattered elastically, the resulting wave has the same absolute value of its

propagating vector $|\boldsymbol{k}'| = |\boldsymbol{k}| = 1/\lambda$. When $\boldsymbol{k}$ and $\boldsymbol{k}'$ have the same origin and the end of $\boldsymbol{k}$ coincides with the origin of the reciprocal lattice, diffraction in the $\boldsymbol{k}'$ direction occurs when the end of the $\boldsymbol{k}'$ vector overlaps with a reciprocal lattice point. Since $\boldsymbol{k}' = \boldsymbol{k} + \boldsymbol{d}^*$, it is easy to see that

$$|\boldsymbol{k}'|sin\theta = |\boldsymbol{k}|sin\theta = \frac{|\boldsymbol{d}^*|}{2} \tag{2.5}$$

which is Bragg's law. The sphere of radius $1/\lambda$ is called the Ewald sphere.

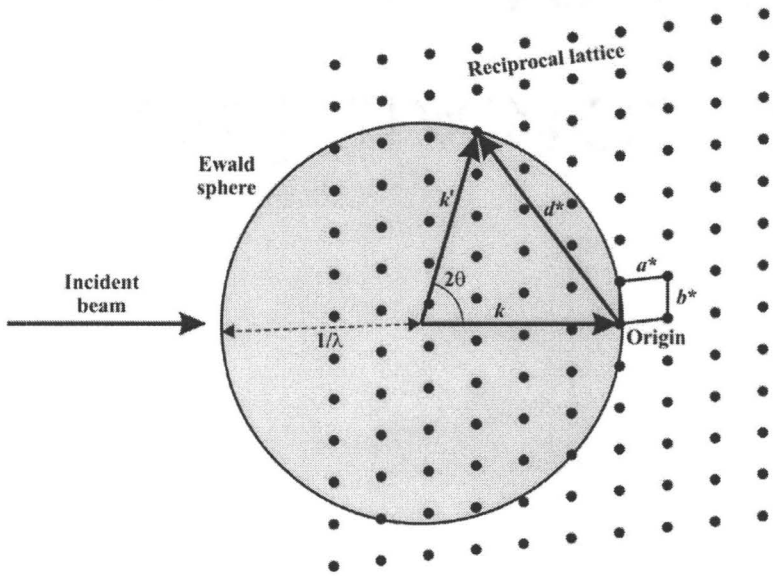

Figure 2.4. Ewald sphere with a radius of $1/\lambda$ and the reciprocal lattice

The intensity of the diffracted beam is related to the structure of the material and is proportional to the square of the structure amplitude $|F_{hkl}|^2$, where F_{hkl} is a structure factor equal to

$$F_{hkl} = \sum_{i=1}^{n} f_i(s) g_i \, t_i(s) \exp[2\pi \mathbf{i}(hx_i + ky_i + lz_i)] \tag{2.6}$$

where n is the total number of atoms in the unit cell; s is the $\sin\theta/\lambda$ function; $f_i(s)$ is the

atomic scattering function; g_i is the occupation factor; $t_i(s)$ is the temperature factor; $\mathbf{i} = \sqrt{-1}$; h, k and l are the Miller indices; x_i, y_i and z_i are coordinates of the i^{th} atom. Another important factor that influences the observed intensities is the absorption, which depends on the geometry, properties of the samples and the specific diffraction instrumentation.

Real and imaginary parts of the structure factor can be separated by the Euler expansion

$$e^{ix} = cosx + isinx \tag{2.7}$$

which results in F_{hkl} being equal to

$$\begin{aligned} F_{hkl} = &\sum_{i=1}^{n} f_i(s) g_i t_i(s) \cos[2\pi(hx_i + ky_i + lz_i)] \\ &+ \mathbf{i} \sum_{i=1}^{n} f_i(s) g_i t_i(s) \sin[2\pi(hx_i + ky_i + lz_i)] \end{aligned} \tag{2.8}$$

The complex number F_{hkl} can be represented as a vector with the real, R_{hkl}, and imaginary, I_{hkl}, components (Fig. 2.5).

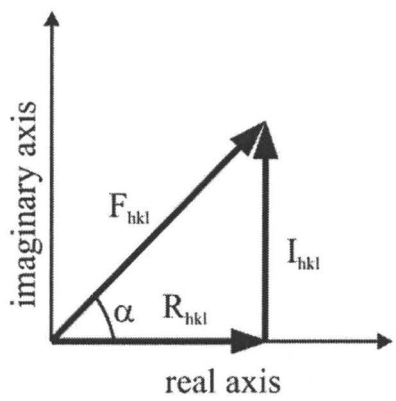

Figure 2.5. Vector representation of the structure factor

The angle α between the structure factor vector and the real axis is called the phase angle. Information about the phase angle is lost during data collection experiments, since the intensity of reflections is proportional to the square of the structure factor. In crystallography, the associated complication is called a phase angle problem. Methods of tackling this problem will be discussed later.

Determination of the structure of a material, i.e. transition from the reciprocal to real space, is done through the mathematical routine called Fourier transformation:

$$\rho_{xyz} = \frac{1}{V} \sum_{h=-\infty}^{h=+\infty} \sum_{k=-\infty}^{k=+\infty} \sum_{l=-\infty}^{l=+\infty} F_{hkl} \exp[-2\pi \mathbf{i}(hx + ky + lz)] \tag{2.9}$$

where ρ_{xyz} is the electron density; V is the volume of the unit cell in the direct space.

2.6 Single crystal X-ray diffraction

2.6.1. Experimental principles behind the single crystal X-ray diffraction

In the single crystal X-ray diffraction experiment, an incident beam interacts with a monocrystalline sample with a typical size of 0.1 to 1 mm. Diffraction occurs when a reciprocal lattice point of the single crystal intersects the Ewald sphere, as described above. For a good quality structural solution and refinement, data must be collected over a wide range of angles, which increases the number of diffraction events, i.e. reflections. Collected reflections then are subject to an automatic or semiautomatic indexing, which includes assigning specific Miller indices to each of the observed reflections, determining a crystallographic space group and unit cell dimensions. Possible space groups are deduced from the systematic absences. The indexed reflections are then integrated, i.e.

intensities of the reflections that were split into several frames are summed with the subsequent generation of an *hkl* file. This file includes the list of the Miller indices of the reflections with the corresponding integrated intensities.

2.6.2. Structural solutions: tackling the phase angle problem

By substituting complex coefficients in eq. 2.9 with the squares of structure amplitudes, the imaginary part vanishes, meaning no phase angles are needed. This method was introduced by Patterson and the resulting equation can be written as

$$P_{xyz} = \frac{2}{V} \sum_{h=0}^{h=+\infty} \sum_{k=0}^{k=+\infty} \sum_{l=0}^{l=+\infty} |F_{hkl}|^2 \cos[2\pi(hx + ky + lz)] \qquad (2.10)$$

where the multiplier 2 appears because only half of the reciprocal space is integrated due to its centrosymmetricity. The P_{xyz} is called a Patterson function.

Due to the loss of the phase angles, no absolute atomic coordinates can be calculated by this method. Instead, the Patterson function provides the distribution of the interatomic vectors in the unit cell. By employing symmetry analysis, this information is used to build possible structural models. However, in the case of complicated structures, the maps of interatomic vectors become packed and vectors can overlap. Therefore, this technique is usually used to find locations of heavy atoms in the unit cell with a subsequent allocation of light atoms through the difference map. Accordingly, the Patterson method is often referred to as a method of heavy atoms.

Phase angles can be obtained from the observed reflections by a statistical technique called the direct method. Here, three reflections r, r' and r-r' which are not

symmetrically related are chosen as follows

$$\begin{aligned} &\text{r: } h, k, l \\ &\text{r': } h', k', l' \\ &\text{r-r': } h-h', k-k', l-l' \end{aligned} \tag{2.11}$$

Corresponding phase angles α_r, $\alpha_{r'}$ and $\alpha_{r-r'}$ are related through the tangent formula

$$\tan \alpha_r \cong \frac{\sum_r |E_{r'}||E_{r-r'}| \sin(\alpha_{r'} + \alpha_{r-r'})}{\sum_r |E_{r'}||E_{r-r'}| \cos(\alpha_{r'} + \alpha_{r-r'})} \tag{2.12}$$

where E_r are the normalized structure factors

$$E_{hkl} = \frac{|F_{hkl}|}{\langle F_{exp}^2 \rangle^{1/2}}. \tag{2.13}$$

Some of the phase angles have to be set arbitrarily. In centrosymmetric structures, phase angles have only two values, 0° and 180°, which greatly simplifies the solution. The direct method produces a set of phase angles which are subject to a subsequent structural refinement.

2.6.3. Refinement of the structural solution

Validity of the structural solution is easily verified during the refinement procedure. In both the single crystal and powder diffraction techniques, structural refinement is based on the minimization of the difference between the observed and calculated intensities through the least-squares method. Single crystal refinement usually includes the following parameters: atomic coordinates, isotropic/anisotropic temperature factors, atomic occupancy/mixing, extinction coefficient (correction for back-reflection and re-reflection) and weighting scheme (corrects contribution from reflections with

different intensities).

A refined model is subject to structural and mathematical validations. The first includes analysis of the interatomic distances, atomic environments, atomic thermal vibrations and the overall chemical and physical sense of the new structure. Mathematical validation is performed by the comparison of the experimental and theoretical (calculated) data through the agreement factors. These are based either on the structure amplitudes

$$R_1 = \frac{\sum_{i=1,n} \left| |F_{obs,i}| - |F_{calc,i}| \right|}{\sum_{i=1,n} |F_{obs,i}|} \tag{2.14}$$

or the squares of the structure factors

$$wR_2 = \left[\frac{\sum_{i=1,n} w_i \left| F^2_{obs,i} - F^2_{calc,i} \right|^2}{\sum_{i=1,n} w_i \left(F^2_{obs,i}\right)^2} \right]^{1/2} \tag{2.15}$$

where n is the number of reflections; $w_i = 1/Y^2_{obs,i}$ where Y is the intensity of observed reflection. The statistical parameter The Goodness of Fit is calculated as

$$S = \left[\frac{\sum_{i=1,n} w_i \left| F^2_{obs,i} - F^2_{calc,i} \right|^2}{n - p} \right]^{1/2} \tag{2.16}$$

where n is the total number of reflections, p – the number of refined parameters.

2.6.4. Single crystal X-ray diffraction instrumentation

The primary machine used for single crystal X-ray diffraction experiments was the STOE IPDS II diffractometer. Here, collimated Mo K_α radiation hits a single crystal mounted on a glass capillary on the goniometer head (Fig. 2.6). The diffracted beam is intercepted by an image-plate area detector with a subsequent scanning and retrieving of

the experimental intensities. The collection range is determined by the detector position and equals 4-59° in 2θ for the default distance of 100 mm from the crystal to the detector. Angle coverage can be increased by moving the detector towards the crystal, but this results in a lower spatial resolution.

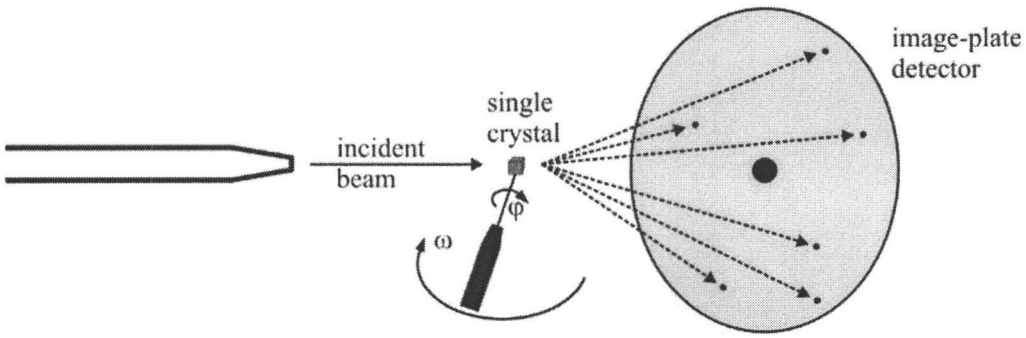

Figure 2.6. Schematics of the single crystal X-ray diffraction setup on the STOE IPDS II diffractometer

Data are collected in the whole reciprocal sphere by scanning along the ω and φ angles, as shown in the Figure 2.6. A typical frame collected on the STOE IPDS II diffractometer is presented in Figure 2.7 (Si single crystal data).

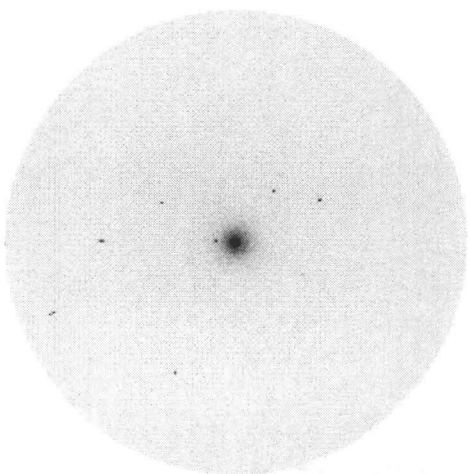

Figure 2.7. Typical frame collected on the STOE IPDS II diffractometer

The collected data are indexed and then integrated using the STOE X-Area software. Subsequent numerical absorption correction is based on the crystal shape derived from the optical face indexing and optimized against the equivalent reflections with the STOE X-Shape software.[1]

A produced *hkl* file is used to solve and refine the structure with the SHELXS and SHELXL programs, respectively.[2]

2.7 Powder X-ray diffraction

2.7.1. Experimental principles behind the powder X-ray diffraction

In a powder diffraction experiment, a studied sample consists of many small single crystals, i.e. it is polycrystalline. Nevertheless, the basic mechanism of diffraction is the same as in the single crystal method: diffraction occurs when the reciprocal lattice intersects the Ewald sphere.

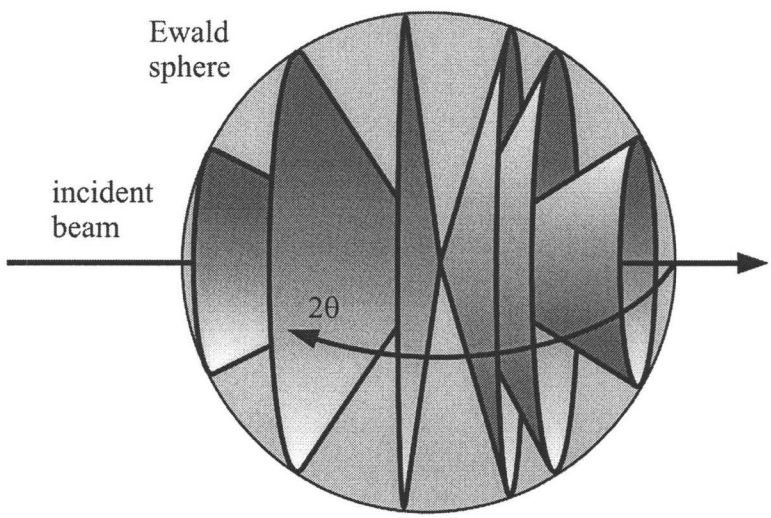

Figure 2.8. Intersection of the Ewald sphere with cones of diffracted radiation from a polycrystalline sample

The difference is that now there are many small single crystals randomly oriented that satisfy the diffraction conditions simultaneously. Their diffraction vectors form a cone around the incident beam direction (Fig. 2.8).

Powder diffraction data are recorded as intensity vs. 2θ angle massifs. Either transmission or reflection geometries are used, with the latter being more common.

2.7.2. Utilizing powder X-ray diffraction data

The great advantage of powder X-ray diffraction is that it allows for the express qualitative analysis of bulk specimens. Experimental diffraction profiles are automatically compared with the database patterns with a subsequent selection of the matching compounds. This procedure is called a phase analysis and is probably the most frequent use of the powder method.

Powder diffraction data are also widely used for the structural refinement of compounds with known structure types. Fundamentals of powder structural refinement are the same as those of single crystal refinement described above. However, in the powder diffraction method, a number of experimental parameters have to be refined along with the structural ones. Usually these are background level, width, shape and asymmetry of peaks, displacement of the sample from the ideal position, preferred orientation, absorption and others.

Agreement factors for the powder diffraction refinement are defined as follows:

$$R_p = 100\frac{\Sigma_{i=1,n}|y_{obs,i} - y_{calc,i}|}{\Sigma_{i=1,n} y_{obs,i}} \qquad (2.17)$$

$$R_{wp} = 100\left[\frac{\sum_{i=1,n} w_i \left|y_{obs,i} - y_{calc,i}\right|^2}{\sum_{i=1,n} w_i \, {y_{obs,i}}^2}\right]^{1/2} \tag{2.18}$$

$$R_{exp} = 100\left[\frac{n-p}{\sum_{i=1,n} w_i \, {y_{obs,i}}^2}\right]^{1/2} \tag{2.19}$$

$$R_B = 100\frac{\sum_{i=1,m}\left|I_{obs,i} - I_{calc,i}\right|}{\sum_{i=1,m} I_{obs,i}} \tag{2.20}$$

$$\chi^2 = 100\left[\frac{R_{wp}}{R_{exp}}\right]^{1/2} \tag{2.21}$$

where y is the profile intensity; I is an integrated intensity; n is the number of data points; p is the number of least-square parameters; m is the number of possible Bragg reflections; $w_i = 1/{Y^2}_{obs,i}$ where Y is the intensity of the observed reflection.

Finally, the powder diffraction technique can be used to solve unknown structures. However, it is not as trivial and straightforward as in the single crystal method. Powder diffraction data are just projections of the reciprocal lattice, which means directions of the reciprocal lattice vectors are lost. This can also result in an overlapping of the experimental peaks which lowers the resolution of the data.

The first step in the structural solution from the powder data is the determination of the unit cell dimensions. It is done through the automatic indexing of the observed reflections with a subsequent deduction of the possible space groups. When high resolution and quality powder data are available, intensities of the experimental peaks can be integrated individually, i.e. the diffraction pattern is decomposed into separate reflections. The resulting dataset is analogous to the *hkl* massifs obtained from the single crystal method. Subsequently, a structural solution can be obtained by the Patterson technique or the direct method.

Another more popular method is called the simulated annealing. Here, multiple structural models are generated using the Monte Carlo or grid search methods and corresponding theoretical powder diffraction profiles are simulated. Local minima are found through the comparison of the theoretical and experimental patterns using the agreement factors. The name "simulated annealing process" reflects the analogy to physical annealing. In this method, a sample virtually heats up very close to the melting point where it has a large degree of freedom for structural transformations. The following cooling allows for the "crystallization" of the phase of interest.

2.7.3. Powder X-ray diffraction instrumentation

Experimental powder diffraction data were collected on the PANalytical diffractometer. Here, an incident line-focused beam hits the sample with a subsequent reflection and capturing of the signal on the detector (Fig. 2.9).

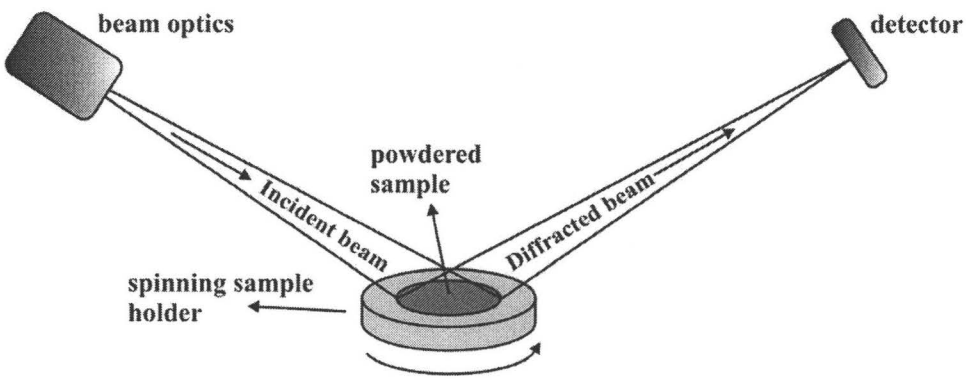

Figure 2.9. Scheme of the powder diffraction experiment setup on the PANalytical diffractometer

The standard operational radiation is $CuK_{\alpha 1}$ monochromated with a Ge single

crystal. For systems rich in Gd and Fe, CoK_α radiation is used in order to eliminate fluorescence associated with the Cu K_α radiation.

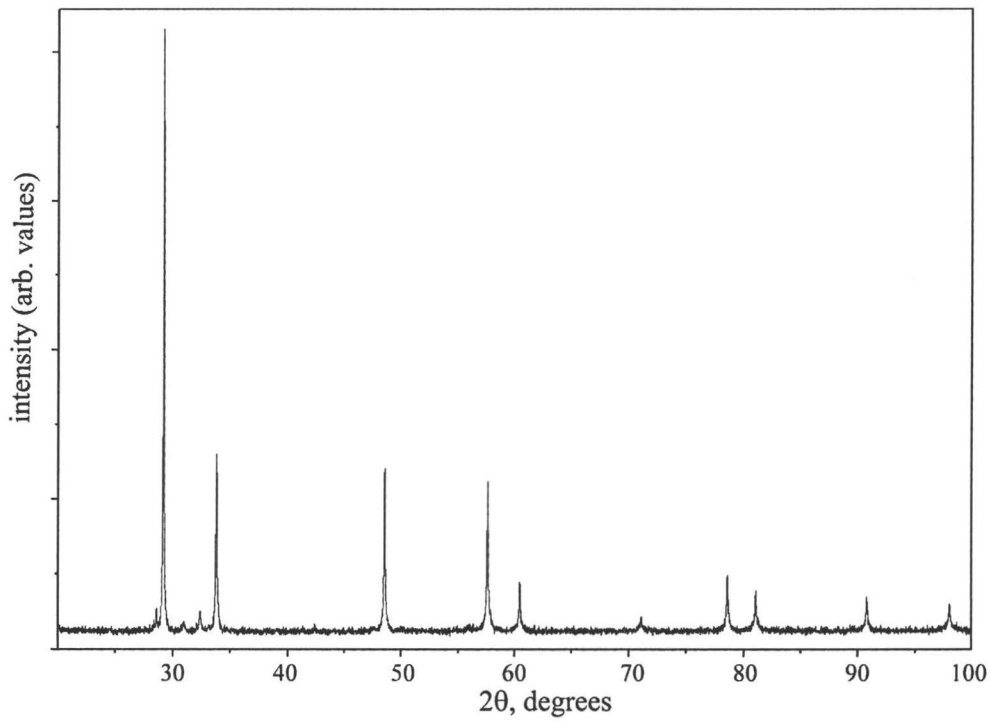

Figure 2.10. Typical X-ray powder diffraction pattern collected on the PANalytical diffractometer

The X-ray detector consists of 128 independent channels to facilitate the collection time. During the data collection, the sample holder spins along its vertical axis to increase the number of diffracting crystallites (Fig. 2.9). Structures were refined using the Fullprof software.[3] A typical powder pattern collected on the PANalytical diffractometer is shown in Figure 2.10 (mixture of gadolinium metal and gadolinium hydride).

References

[1] *Stoe & Cie GmbH*, Darmstadt: Germany, **2004**.

[2] G. M. Sheldrick, *SHELXL97 and SHELXS97*; University of Gottingen: Germany, **1997**.

[3] J. Rodriguez-Carvajal, *IUCr Newsletter* **2001**, *26*, 12-19.

Chapter 3. $Gd_5Si_{4-x}P_x$: targeted structural changes through increase in valence electron count

This chapter contains the manuscript "$Gd_5Si_{4-x}P_x$: targeted structural changes through increase in valence electron count", published in the Journal of the American Chemical Society (*J. Am. Chem. Soc.* **2009**, *131*, 2367–2374). The candidate completed all of the experimental synthesis, data collection, processing and interpretation and prepared the manuscript. Electronic structure calculations were performed in collaboration with Dr. G. J. Miller.

$Gd_5Si_{4-x}P_x$: targeted structural changes through increase in valence electron count

Volodymyr Svitlyk,[a] Gordon J. Miller,[b] and Yurij Mozharivskyj[a]

[a]*Department of Chemistry, McMaster University, Hamilton, Ontario, L8S 4M1, Canada*

[b]*Department of Chemistry, Iowa State University, Ames, Iowa 50011*

3.1 Abstract

Phase transformations in the $Gd_5Si_{4-x}P_x$ system ($0 \leq x \leq 2$), studied through X-ray diffraction techniques, reveal an intimate coupling between the crystal structure and valence electron count. An increase in the valence electron count through P substitution results in breaking the interslab *T*-*T* dimers ($d_{T\text{-}T}$ = 3.74 Å; *T* is a mixture of Si and P) and shear movement of the $\propto^2[Gd_5T_4]$ slabs in $Gd_5Si_{2.75}P_{1.25}$. The $Gd_5Si_{2.75}P_{1.25}$ phase extends the existence of the orthorhombic Sm_5Ge_4-type structures to the valence electron count larger than 31 e^-/formula unit. Tight-binding linear-muffin-tin-orbital calculations trace the origin of the *T*-*T* dimer cleavage in $Gd_5Si_{2.75}P_{1.25}$ to a larger population of antibonding states within the dimers.

3.2 Introduction

Discovery of the giant magnetocaloric effect in $Gd_5Si_2Ge_2$,[1] followed by a successful test of a rotary magnetic refrigerator,[2,3] showed that the magnetocaloric effect may be beneficially utilized for room-temperature refrigeration and air conditioning. The unique feature which makes $Gd_5Si_2Ge_2$ and other materials, like $MnFeP_{1-x}As_x$, suitable for

practical applications is an intrinsic coupling between a first-order structural transition and ferromagnetic ordering.[4,5] As a result, the entropy change is significantly increased (nearly doubled in $Gd_5Si_2Ge_2$ for ΔH = 0-5 T) and the magneto-structural transformation yields a large temperature response to magnetic field.[6] The origin of structural transformations in $Gd_5Si_2Ge_2$ and related phases can be traced back to the interslab *T*-*T* dimer cleavage and formation (*T* is a mixture of main group elements, viz., Si, Ge, Sn, and Ga) and, associated with that, movement of the $_\infty^2[Gd_5T_4]$ slabs,[7] which are the main building blocks of these structures. Thus, the ability to control the *T*-*T* bonds is a possibility to tune structural and physical properties of existing magnetocaloric materials and a route to design new phases.

The RE_5T_4 phases (*RE* is a rare-earth metal), except for some Si-rich La-Nd phases, adopt three related structures types: (1) the orthorhombic Gd_5Si_4-type with all interslab *T*-*T* dimers intact ($d_{T\text{-}T}$ = ca. 2.5 Å); (2) the monoclinic $Gd_5Si_2Ge_2$-type, in which the *T*-*T* dimers between alternate layers are broken ($d_{T\text{-}T}$ = ca. 3.4 Å); and (3) the orthorhombic Sm_5Ge_4-type with all interslab dimers broken.[4,8-16] The interslab dimers arise from one crystallographic site, called the *T*1 site. There are two additional sites for main group atoms, *T*2 and *T*3, which also form dimers, but these dimers reside inside the $_\infty^2[Gd_5T_4]$ slabs and are not perturbed during any structural transition.[7] As discussed later in the text and previously for some RE_5T_4 phases,[17-19] the chemical formulas of the three structure types can be written as $(RE^{3+})_5(T_2^{6-})_2(3e^-)$, $(RE^{3+})_5(T_2^{6-})_{1.5}(T^{4-})(2e^-)$ and $(RE^{3+})_5(T_2^{6-})(T^{4-})_2(e^-)$. The conduction electrons noted in these formulas reside in the region of the conduction band that consists of bonding *RE*-*RE* and *RE*-*T* states, but

antibonding *T*-*T* states. The suggested electron counting scheme for the RE_5T_4 phases implies that their structures and, consequently, their properties can be governed by the valence electron count (VEC). This hypothesis was substantiated when the Gd_5Ge_4 phase with VEC = 31 e^- and broken interslab dimers could reform the *T*1-*T*1 dimers through partial substitution of Ge by the size-equivalent triel Ga in $Gd_5Ga_xGe_{4-x}$ (x = 1-2, VEC = 29-30 e^-).[17] Seo et al. subsequently demonstrated that lowering the VEC through substitution of trivalent La and Ce with divalent Ca also leads to *T*1-*T*1 dimer formation in $La_{5-x}Ca_xGe_4$ and $Ce_{5-x}Ca_xGe_4$.[19] So far, rigorous exploration of the relationship between VEC and structure for the RE_5X_4 phases has been limited to VEC $\leq$ 31 e^- and focused on forming interslab dimers into the Sm_5Ge_4-type structures.

Alternatively, it should be possible to break interslab dimers in Gd_5Si_4-type structures with VEC = 31 e^- by increasing the VEC. To explore structural responses of RE_5T_4 to higher VECs unambiguously, size-equivalent but electron-richer atoms must be introduced into a structure with interslab dimers intact. The $Gd_5Si_{4-x}P_x$ system was chosen for such studies because the parent Gd_5Si_4 phase contains interslab dimers, and similar atomic radii of Si and P (covalent radii, r_{cov}, of Si and P, respectively, are 1.17 and 1.10 Å)[20] will minimize possible matrix effects. In this paper, we report for the first time the synthesis and characterization of $Gd_5Si_{4-x}P_x$ phases, in which an increase in the VEC through P substitution was employed to break the Si-Si dimers of the parent Gd_5Si_4 phase. With this $Gd_5Si_{4-x}P_x$ series, we extend the existence of the RE_5T_4 phases adopting the Sm_5Ge_4-type structure into an electron-richer region, above the VEC of 31 e^-/formula unit, and have verified the prediction of breaking interslab dimers by replacing some Si

atoms with P in Gd_5Si_4.

3.3 Experimental section

3.3.1 Synthesis

According to our in-house analysis, the gadolinium powders purchased from several suppliers were severely contaminated with hydrogen. Since such light atom impurities may have a detrimental effect on physical and structural properties,[21,22] the synthesis of $Gd_5Si_{4-x}P_x$ phases had to proceed from bulk gadolinium. Starting materials included pieces of gadolinium (99.99 wt.%, distilled grade, Metall Rare Earth Limited, China), silicon (99.999 wt.%, Alfa Aesar), and phosphorus (99.999 wt.%, Puratronic, Alfa Aesar). To avoid introducing contaminants by filing gadolinium, pieces of Gd and Si in a 1:1 molar ratio were arc-melted to obtain the GdSi binary phase (FeB-type structure). The resulting GdSi product was ground in an Ar-filled glovebox and intimately mixed with ground phosphorus in the GdSi:P molar ratio of 1:1. This mixture was pressed, sealed in an evacuated silica tube, heated to 400 at 50 °C/hour, kept at this temperature for 12 h, then heated to 800 at 50 °C/hour, kept at this temperature for 48 h, and subsequently quenched in cold water. X-ray powder diffraction analysis indicated that P substituted for Si in GdSi to form the GdP binary phase (NaCl-type structure), thereby discharging elemental Si. This sample was then ground in the glovebox and pressed into seven tablets. Each tablet was combined with a proper amount of Gd and Si pieces to target $Gd_5Si_{4-x}P_x$ with compositions x = 0.25, 0.50, 0.75, 1.00, 1.25, 1.50, and 2.00, and the samples were arc-melted. During melting total losses were negligible, <0.2 wt.%. Any

P losses, which would be recognized by a white deposit inside the chamber, could not be detected. Absence of any significant P losses can be explained by the fact that phosphorus was bound as an anion into the highly refractory GdP binary phase. The Gd_5Si_4 phase was prepared by directly arc-melting Gd and Si pieces; the resulting buttons were remelted at least 3 times to improve homogeneity.

3.3.2 X-ray analysis

Phase analyses and lattice constant refinements of the products were completed on a PANalytical X'Pert Pro diffractometer with a linear X'Celerator detector. Co*K*α radiation was used to avoid the Gd fluorescence associated with Cu*K*α radiation and to obtain a better resolution required for the refinement of the structurally similar and simultaneously present Gd_5Si_4- and Sm_5Ge_4-type phases. The unit cell parameters derived from a full-profile Rietveld refinement (*Rietica* program[23]) are summarized in Table 3.1. Amounts of the Gd_5Si_4- and Sm_5Ge_4-type phases were estimated using the same technique. The $Gd_5Si_{4-x}P_x$ samples with x = 0.25-1.00 were found to be mixtures of both Gd_5Si_4- and Sm_5Ge_4-type phases, with the amount of Sm_5Ge_4-type phase being proportional to the P concentration, x. Samples with x = 1.25-2.00 did not contain a Gd_5Si_4-type phase. However, at x = 1.50 and 2.00, large amounts of a GdP impurity were observed. Based on the phase analysis, it can be concluded that the Sm_5Ge_4-type phase of $Gd_5Si_{4-x}P_x$ appears in the region of $1.00 < x \leq 1.25$. The unit cell parameters, specifically a and c as well as the c/a ratio (Figure 3.1), point to some possible homogeneity for the Sm_5Ge_4-type phase. But this homogeneity is expected to be relatively small and unlikely

to go much beyond $x = 1.25$, as the increase in the P content above $x = 1.25$ yields almost identical lattice constants and leads to a larger GdP presence.

Table 3.1. Crystallographic data for the $Gd_5Si_{4-x}P_x$ powders and single crystals

x	sample	str. type of phases	a, Å	b, Å	c, Å	c/a	V, Å^3
0	crystal	Gd_5Si_4	7.4743(5)	14.753(1)	7.7424(5)	1.0359(1)	853.7(1)
	powder	Gd_5Si_4	7.4827(4)	14.746(1)	7.7473(5)	1.0354(1)	854.9(1)
0.25	powder[a]	Gd_5Si_4	7.4910(5)	14.712(1)	7.7430(6)	1.0336(2)	853.3(1)
0.5	crystal	Gd_5Si_4[b] + Sm_5Ge_4	7.522(1)	14.698(3)	7.724(1)	1.0268(2)	853.9(3)
	powder	Gd_5Si_4[b]	7.4909(6)	14.692(1)	7.7504(6)	1.0346(1)	853.0(1)
		Sm_5Ge_4	7.5739(9)	14.671(2)	7.6686(9)	1.0125(2)	852.1(2)
0.75	crystal	Gd_5Si_4+ Sm_5Ge_4[b]	7.548(1)	14.661(3)	7.698(1)	1.0199(2)	851.9(3)
	powder	Gd_5Si_4	7.4916(9)	14.668(2)	7.7414(9)	1.0333(2)	850.7(2)
		Sm_5Ge_4[b]	7.5758(9)	14.664(2)	7.6653(8)	1.0118(2)	851.5(2)
1	crystal	Gd_5Si_4+ Sm_5Ge_4[b]	7.545(1)	14.669(2)	7.695(1)	1.0199(2)	851.7(3)
	powder	Gd_5Si_4	7.4890(8)	14.663(2)	7.751(1)	1.0350(4)	851.1(2)
		Sm_5Ge_4[b]	7.5834(8)	14.649(2)	7.6624(7)	1.0104(1)	851.2(1)
1.25	crystal	Sm_5Ge_4	7.607(2)	14.645(3)	7.684(2)	1.0101(4)	856.0(4)
	powder	Sm_5Ge_4	7.5913(7)	14.628(1)	7.6656(7)	1.0098(1)	851.2(1)
1.5	powder	Sm_5Ge_4	7.5935(5)	14.626(1)	7.6661(5)	1.0096(1)	851.4(1)
2	powder	Sm_5Ge_4	7.5946(5)	14.620(1)	7.6634(5)	1.0091(1)	850.9(1)

[a] Cell parameters of the Sm_5Ge_4-type phase could not be reliably refined. [b] Dominant phase.

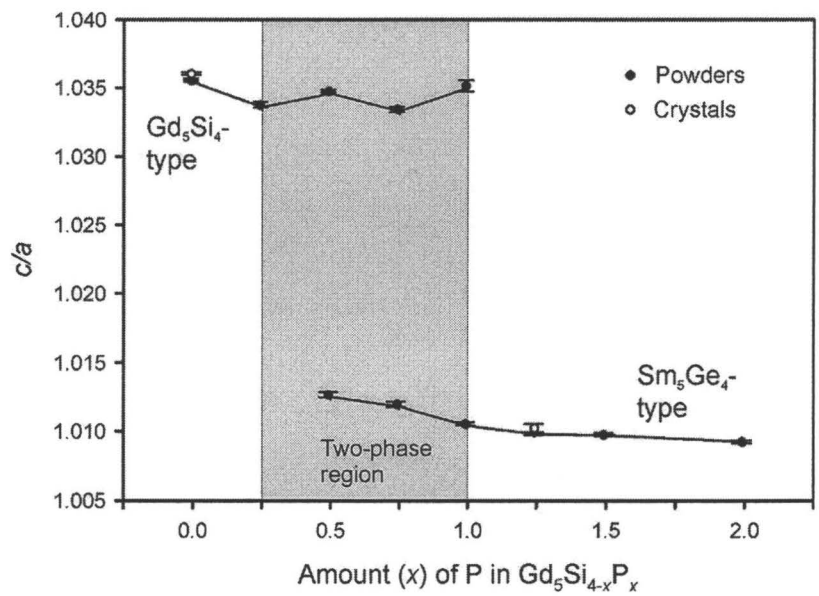

Figure 3.1. *c/a* ratio as a function of P amount. The gray area indicates a two-phase region as established from X-ray powder diffraction patterns at room temperature

Single crystals were extracted from the samples with x = 0, 0.50, 0.75, 1.00 and 1.25. Room-temperature data were collected on a STOE IPDS II diffractometer with Mo Kα radiation. Numerical absorption corrections were based on the crystal shapes that were originally derived from optical face indexing, but later optimized against equivalent reflections using STOE *X-Shape* software.[24] Structural refinements were performed using the *SHELXL* program.[25] Significant crystallographic results are summarized in Tables 3.2 and 3.3. Since the atomic scattering factors of Si and P are nearly identical, the same Si/P statistical mixtures consistent with sample compositions were assumed on the three T sites. Nearest-neighbor bond distances could not be used to distinguish Si and P atoms adequately, because their similar atomic radii makes such analysis untenable.

Table 3.2. Crystal data and structure refinements for Gd_5Si_4 and $Gd_5Si_{2.75}P_{1.25}$ at 293 K, Mo$K_{\alpha 1}$ radiation, STOE IPDS II diffractometer

composition	Gd_5Si_4	$Gd_5Si_{2.75}P_{1.25}$
Space group	*Pnma*	*Pnma*
Lattice parameters (Å)	a = 7.4743(5)	a = 7.607(2)
	b = 14.7529(7)	b = 14.645(3)
	c = 7.7424(4)	c = 7.684(2)
Volume (Å^3)	853.74(8)	856.0(4)
Z	4	4
Density (calculated), g/cm^3	6.991	7.000
Crystal size, mm^3	0.09 × 0.11 × 0.17	0.05 × 0.07 × 0.08
2θ range for data collection	5.94 to 58.30°	5.76 to 56.56°
Index ranges	$-10 \le h \le 10$, $-20 \le k \le 16$, $-10 \le l \le 10$	$-10 \le h \le 9$, $-19 \le k \le 19$, $-6 \le l \le 10$
Reflections collected	8147	6432
Independent reflections	1192 [R_{int} = 0.0712]	1065 [R_{int} = 0.0494]
Completeness to max 2θ	99.8%	96.7%
Data/restraints/parameters	1192/0/47	1095/0/47
Goodness-of-fit on F^2	1.089	1.112
Final R indices [$I > 2\sigma(I)$]	R_1 = 0.0344, wR_2 = 0.0749	R_1 = 0.0754, wR_2 = 0.1633
R indices (all data)	R_1 = 0.0419, wR_2 = 0.0774	R_1 = 0.0823, wR_2 = 0.1665
Extinction coefficient	0.00356(19)	0.00063(11)
Largest diff. peak/ hole, e$^-$/Å^3	2.800/-2.802	5.769/-3.944

Table 3.3. Atomic and isotropic temperature (U_{eq}) parameters for Gd_5Si_4 and $Gd_5Si_{2.75}P_{1.25}$ from single crystal diffraction data

atom	site	occupancy	*x/a*	*y/b*	*z/c*	U_{eq} (Å^2)
Gd_5Si_4						
Gd1	8*d*	1	0.02881(5)	0.59724(3)	0.18263(5)	0.0110(2)
Gd2	8*d*	1	0.31646(5)	0.12238(3)	0.17964(5)	0.0095(2)
Gd3	4*c*	1	0.14440(7)	0.25	0.51113(7)	0.0094(2)
Si1	8*d*	1	0.1439(3)	0.0400(2)	0.4723(3)	0.0116(4)
Si2	4*c*	1	0.0214(4)	0.25	0.0996(4)	0.0112(6)
Si3	4*c*	1	0.2590(4)	0.25	0.8753(5)	0.0106(6)
$Gd_5Si_{2.75}P_{1.25}$						
Gd1	8*d*	1	-0.0380(2)	0.60363(8)	0.1765(2)	0.0110(3)
Gd2	8*d*	1	0.3916(2)	0.11477(8)	0.1650(2)	0.0105(3)
Gd3	4*c*	1	0.2205(2)	0.25	0.5013(2)	0.0091(3)
Si/P1	8*d*	0.69/0.31[a]	0.2275(9)	0.0469(4)	0.4772(9)	0.011(1)
Si/P2	4*c*	0.69/0.31[a]	0.0998(14)	0.25	0.1114(12)	0.012(2)
Si/P3	4*c*	0.69/0.31[a]	0.3309(13)	0.25	0.8748(13)	0.010(2)

[a] Si/P occupancy was not refined

Structural refinements for the crystals with x = 0.50, 0.75, and 1.00 produced positive residual electron density accompanying every atomic position. Additional crystals were tested for each sample, but identical results were obtained. The electron density maps generated from the experimental intensities showed a smeared, pear-shape electron density distribution around every atomic site. Comparison of these maps with those from Gd_5Si_4 and $Gd_5Si_{2.75}P_{1.25}$ (Figure 3.2) indicated that such electron density peaks result from the superposition of the two different structures, Gd_5Si_4 and $Gd_5Si_{2.75}P_{1.25}$. Presence of a possible superstructure, which could account for the diffuse electron density, was not supported due to the lack of additional Bragg reflections. Therefore, it was concluded that the crystals are twins of the Gd_5Si_4- and Sm_5Ge_4-type structures with similar unit cells but different atomic arrangements. Since the unit cell parameters of the Gd_5Si_4- and Sm_5Ge_4-type structures from the same $Gd_5Si_{4-x}P_x$ sample

are quite similar (as judged from X-ray powder diffraction), peak splitting is small and could not be reliably detected due to the low spatial resolution of the area detector.

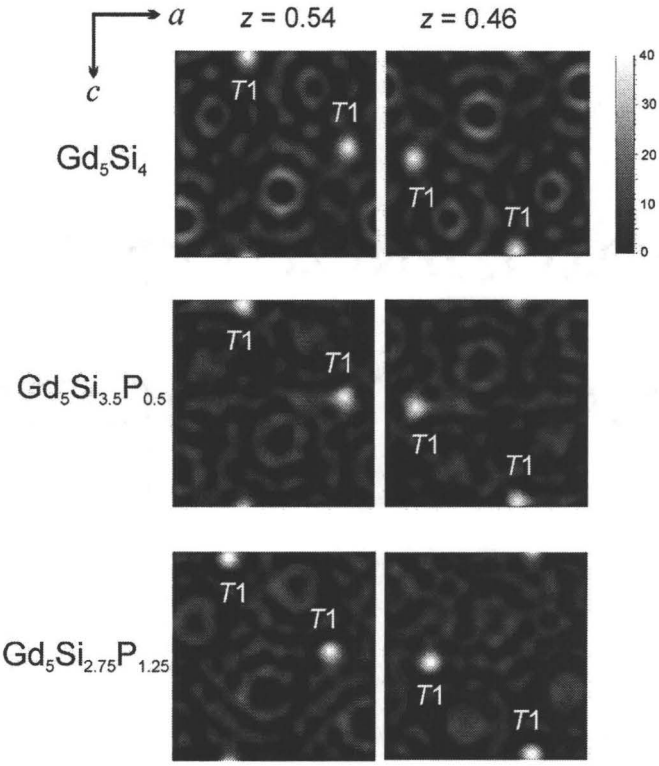

Figure 3.2. Electron density maps for Gd_5Si_4, $Gd_5Si_{3.5}P_{0.5}$ and $Gd_5Si_{2.75}P_{1.25}$. The planes from two different unit cells at two different z values are shown in order to emphasize changes in the $T1$-$T1$ dimer distances

Instead, the positions and intensities of the peaks originating from the two structures were averaged which resulted in the average unit cell dimensions and composite atomic arrangements during refinements. Indeed, the unit cell parameters of the crystals with x = 0.50, 0.75, and 1.00 fall between the values obtained for the Gd_5Si_4- and Sm_5Ge_4-type structures for the same sample. Annealing the samples with x = 0.50, 0.75, and 1.00 at 800 °C for two weeks did not eliminate the crystal twinning. Although unusual, such

twinning has been previously observed in the two-phase regions of the $Gd_5Ga_xGe_{4-x}$ and $Gd_5Si_{4-x}Ge_x$ systems.[17,26] In $Gd_5Si_{1.5}Ge_{2.5}$, the composite nature of the crystals was traced to their microscopic inhomogeneity.[26] A similar compositional inhomogeneity can be assumed to exist on the microscopic level in the two-phase $Gd_5Si_{4-x}P_x$ samples. Further details of the crystal structure investigations can be obtained from the Fachinformationszentrum Karlsruhe, 76344 Eggenstein-Leopoldshafen, Germany, (fax: (49) 7247-808-666; e-mail: crysdata@fiz.karlsruhe.de) on quoting the depository CSD numbers 420010 for Gd_5Si_4 and 420011 for $Gd_5Si_{2.75}P_{1.25}$ and also from the Supporting Information.

3.3.3 Electronic structure calculations

Tight-binding, linear-muffin-tin-orbital calculations using the atomic sphere approximation (TBLMTO-ASA)[27] were carried out for Gd_5Si_4 and a hypothetical "Gd_5Si_3P" with the Stuttgart program.[28] The lattice and atomic parameters from the $Gd_5Si_{2.75}P_{1.25}$ single crystal were used for the structure of "Gd_5Si_3P." Exchange and correlation were treated by the local density approximation (LDA).[29] All relativistic effects except spin-orbit coupling were taken into account by using a scalar relativistic approximation.[30] In the ASA method, space is filled with overlapping Wigner-Seitz (WS) atomic spheres, the radii of which were obtained by requiring the overlapping potential to be the best possible approximation to the full potential. This overlap should not be too large because the error in kinetic energy introduced by the combined correction is proportional to the fourth power of the relative sphere overlap. To satisfy the overlap

criteria of the atomic spheres in the TB-LMTO-ASA method, empty spheres were included in the unit cell employing an automatic sphere generation.[31] The WS radii employed for these calculations are as follows: Gd = 1.75-1.81 Å, Si = 1.47-1.57 Å, *P* = 1.45-1.54 Å, and empty spheres = 0.69-1.06 Å. The basis sets included 6s, 6p, and 5d wave functions for Gd; 3s and 3p wave functions for Si and P; and 1s functions for the empty spheres. The Gd 6p orbitals were treated by the Löwdin downfolding technique,[27,29,30] and the 4f electrons of Gd were treated as core electrons. The *k*-space integrations were performed by the tetrahedron method.[32] The self-consistent charge density was obtained using 256 irreducible *k*-points in the Brillouin zone for the orthorhombic cells.

Three different structural models were considered for "Gd_5Si_3P." In the first model, the P atoms were placed on one-half of the *T*1 sites in a way that the nearest P neighbors are only Si1 atoms (*Pnma* symmetry was reduced to $P2_1ma$); in two other models, the P atoms were placed, respectively, on the *T*2 and *T*3 sites.

3.4 Results and discussion

3.4.1 Structural changes

The phase transition in the $Gd_5Si_{4-x}P_x$ series, which occurs between Gd_5Si_4 and $Gd_5Si_{2.75}P_{1.25}$, can be characterized as a Gd_5Si_4-to-Sm_5Ge_4 transformation. Gd_5Si_4 adopts its own structure type, while $Gd_5Si_{2.75}P_{1.25}$ crystallizes with the Sm_5Ge_4-type structure. The detailed description of the two structure types can be found elsewhere,[4,33,34] so only a brief summary of the most important structural features will be presented here. The

Gd_5Si_4-type and Sm_5Ge_4-type structures of the $Gd_5Si_{4-x}P_x$ series are built from nearly identical 3^2434 nets of Gd atoms (Figure 3.3).

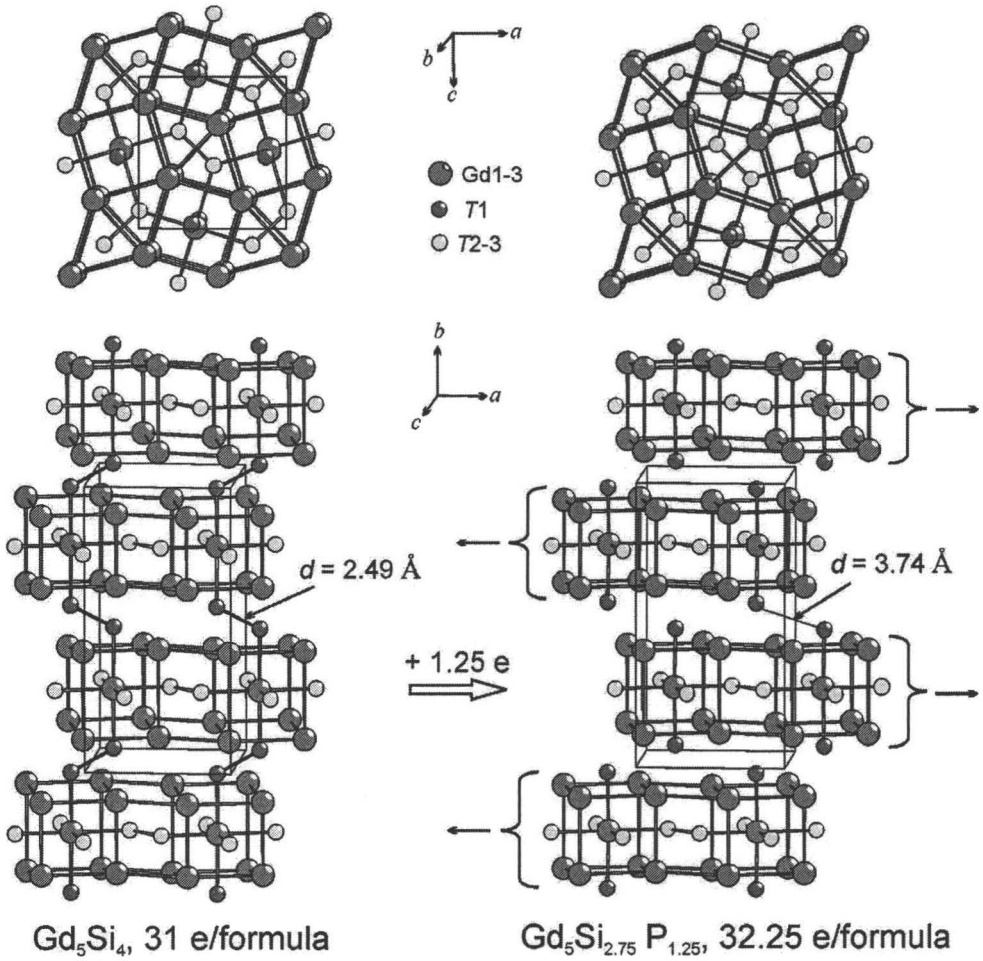

Figure 3.3. Crystal structure of Gd_5Si_4 and $Gd_5Si_{2.75}P_{1.25}$ as projected along *b* (top) and *c* directions (bottom). Movement of the slabs in $Gd_5Si_{2.75}P_{1.25}$, which leads to the *T*1-*T*1 dimer cleavage, is represented by arrows

Two such nets are stacked over one another along the *b* axis to form two-dimensional slabs with Gd3 atoms in pseudocubic and *T*2, *T*3 main group atoms in trigonal prismatic voids. Since the trigonal prisms in these slabs share a face, the separation between the *T*2

and $T3$ atoms is small enough to allow dimer formation. The Gd pseudocubes are capped top and bottom by the $T1$ atoms, and the empirical composition of the slabs is identical to the overall composition of the phase, Gd_5T_4. Whereas in Gd_5Si_4 the $\propto^2[Gd_5T_4]$ slabs are interconnected via Si1-Si1 bonds ($d_{Si1\text{-}Si1}$ = 2.49 Å), all $T1$- $T1$ interslab bonds are broken ($d_{T1\text{-}T1}$ = 3.74 Å) in $Gd_5Si_{2.75}P_{1.25}$. This bond cleavage is accompanied by a shear movement of the slabs primarily along the *a*-direction and an increase in the corresponding lattice parameter of the Sm_5Ge_4-type phases. This type of phase transition can be monitored in $Gd_5Si_{4-x}P_x$ through the *c/a* ratio, as proposed by Choe et al.[26] for $Gd_5Si_{4-x}Ge_x$ and also successfully applied to other related phases.[17,19] For the $Gd_5Si_{4-x}P_x$ powders, the *c/a* ratio changes discontinuously, which indicates a first-order structural transformation (Figure 3.1). For the single crystal data, the increase in *c/a* is smoother, with intermediate *c/a* values in the two-phase region, which is due to their unusual structural behavior in this region, as discussed above.

The shear movement of the $\propto^2[Gd_5T_4]$ slabs in $Gd_5Si_{4-x}P_x$ is expected to alter interslab interactions more significantly than the intraslab ones. Indeed, using *T-T* dimer distances as a perturbation parameter, it can be seen that the atomic arrangements are only slightly disturbed within the slabs ($d_{T2\text{-}T3}$ = 2.53 Å in $Gd_5Si_{2.75}P_{1.25}$ vs $d_{Si2\text{-}Si3}$ = 2.48 Å in Gd_5Si_4), while significantly disrupted between the slabs ($d_{T1\text{-}T1}$ = 3.74 Å vs $d_{Si1\text{-}Si1}$ = 2.49 Å) along the Gd_5Si_4-to-$Gd_5Si_{2.75}P_{1.25}$ transition. A more detailed analysis of the interatomic distances supports this argument and reveals that the intraslab Gd-*T* and Gd-Gd bonds remain almost unaltered, whereas the interslab Gd-$T1$ bonds become appreciably shorter and Gd-Gd contacts somewhat larger (Table 3.4), as also seen in

$Gd_5Si_{4-x}Ge_x$.[35] Such variations in the interatomic distances highlight the two unique features of the Gd_5T_4 structures, and the RE_5T_4 ones in general, namely the rigidity of the $_\infty^2[Gd_5T_4]$ slabs and flexibility of the interslab bonds. Thus, the interslab dimers in $Gd_5Si_{2.75}P_{1.25}$ respond to the larger VEC by breaking $T1$-$T1$ bonds, thereby accommodating the additional conduction electrons in the valence shell of these Si or P monomers. In this way, $Gd_5Si_{2.75}P_{1.25}$ with the VEC of 32.25 e^- is able to preserve the $_\infty^2[Gd_5T_4]$ layers, i.e., the essential building units of the RE_5T_4 structures, while optimizing the interslab interactions. To understand the relationship between the increased VEC and the dimer cleavage in $Gd_5Si_{2.75}P_{1.25}$, we will first consider the electronic structure of Gd_5Si_4.

3.4.2 Electronic structure of Gd_5Si_4

Qualitatively, the electronic structure of many intermetallic compounds containing main group elements can be successfully analyzed within the framework of the Zintl-Klemm electron counting formalism.[36] According to this concept, the Si dimers of Gd_5Si_4 are isoelectronic with halogen dimers and carry a formal negative charge of 6 (Si_2^{6-} dimers). If ionic interactions between the Si_2^{6-} dimers and Gd^{3+} cations are implied, only 28 valence electrons are required to optimize interactions. In reality, the Gd-Si interactions are far from being ionic. Furthermore, short Gd-Gd distances indicate strong bonding between the neighboring Gd atoms. Still treating the Gd atoms as Gd^{3+}, the chemical formula can be written as $(Gd^{3+})_5(Si_2^{6-})_2(3e^-)$. The three valence electrons in excess of 28 e^- will occupy a mixture of Si-Si σ_p^* antibonding states as well as Gd-Gd

and Gd-Si bonding states.

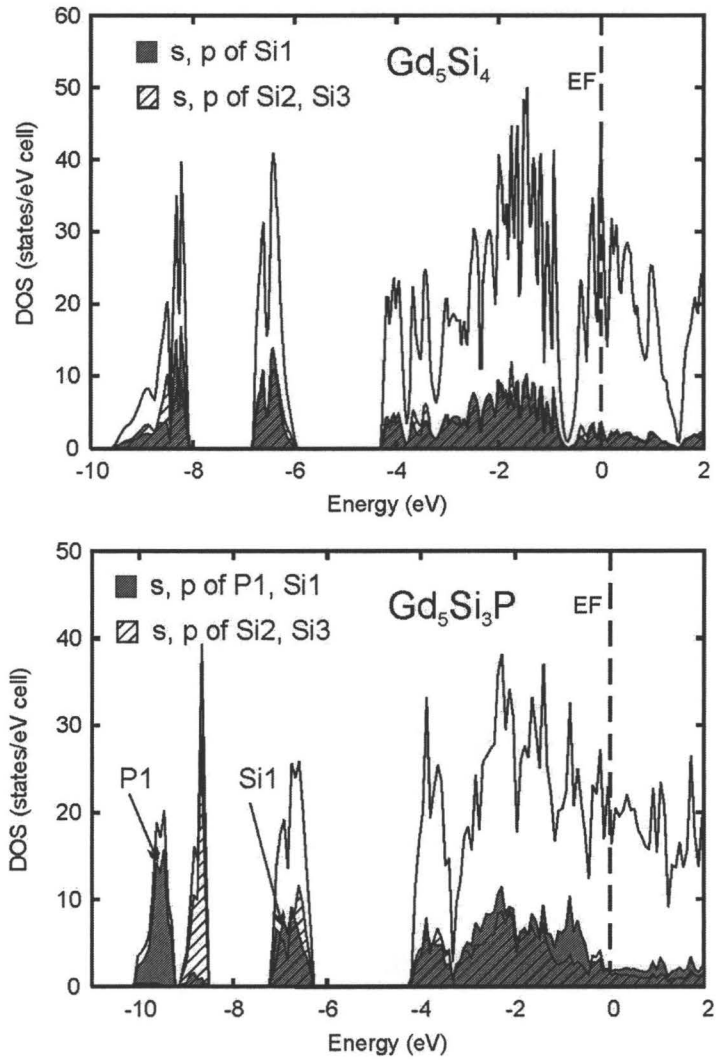

Figure 3.4. Total and projected densities of states (DOS) for Gd_5Si_4 and "Gd_5Si_3P"

This simple bonding scheme is supported by TB-LMTO-ASA electronic structure calculations (Figures 3.4 and 3.5). In the density of states (DOS) and crystal orbital Hamilton population (COHP) plots, the two peaks around -8.5 and -6.5 eV represent, respectively, the bonding σ_s and antibonding σ_s* states from the Si_2 dimers, with some contribution from Gd orbitals. Due to the similar Si1-Si1 and Si2-Si3 bond lengths, the

states originating from the two distinct dimers (Si1-Si1 and Si2-Si3) significantly overlap each other in the DOS curve. The valence band, which extends from -4.5 to -0.7 eV, is separated by a pseudogap from the conduction band. The states below -0.7 eV are derived primarily from the σ_p, π, and π^* states of the Si_2 dimers mixed with Gd 6*s* and 5d orbitals. The states up to the pseudogap account for 28 valence electrons/formula, which agrees with the results obtained by the Zintl-Klemm approach. Presence of Gd states in this low-energy region is due to the interactions between the 3p lone pairs of the Si_2 dimers and Gd orbitals as well as to the Gd-Gd bonds.

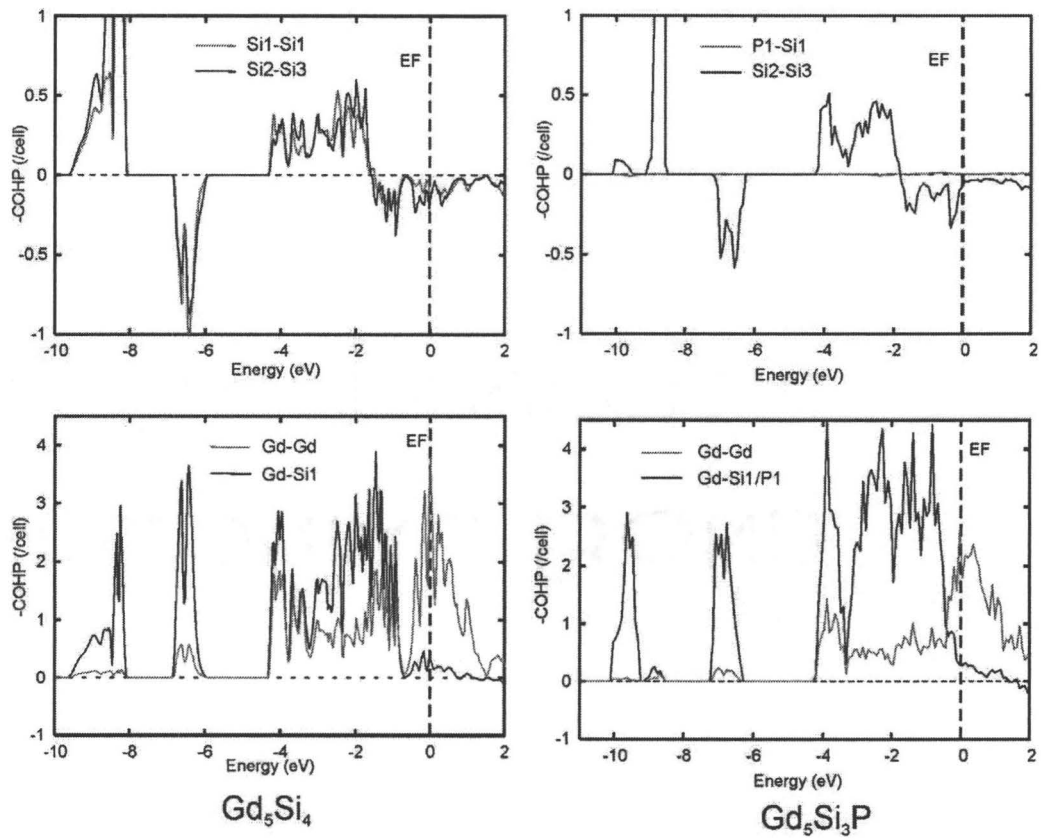

Figure 3.5. Crystal orbital Hamilton population (COHP) curves for some interactions in Gd_5Si_4 and "Gd_5Si_3P". Interactions in the upper part are bonding and in the lower part are antibonding

The conduction band, which lies above -0.7 eV, has the largest contribution from Gd 5d and 6p orbitals and a small contribution from the σ_p* antibonding states within the Si_2 dimers. Analysis of the bonding characteristics by COHP curves indicates antibonding interslab and intraslab Si-Si interactions (Figure 3.5), with all other interactions being bonding around the Fermi level. The occupancy of the Si-Si σ_p* antibonding states indicates a potential electronic instability, which can be partially lifted by breaking interslab Si1-Si1 bonds as observed in Er_5Si_4 below 222 K.[37] However, in Gd_5Si_4, this instability is not observed to be lifted at low temperatures. Thus, other approaches, in particular variations in VEC, can be used to eliminate it.

3.4.3 Electronic structure of "Gd_5Si_3P"

Increasing the VEC through P substitution will have a destabilizing effect on both the intraslab and interslab *T*-*T* dimers in the Gd_5Si_4-type phases. Thus, a structural response is expected from electronic considerations and, indeed, is observed in $Gd_5Si_{2.75}P_{1.25}$ in the form of *T*1-*T*1 dimer cleavage. For simplicity, we assume that the transition also occurs in "Gd_5Si_3P." By treating the monomers resulting from the *T*1-*T*1 dimer cleavage to be isoelectronic with noble gas atoms, "Gd_5Si_3P" can be formulated as $(Gd^{3+})_5(Si_2^{6-})(Si^{4-})(P^{3-})(2e^-)$ when P is on the *T*1 site or $(Gd^{3+})_5([SiP]^{5-})(Si^{4-})_2(2e^-)$ when P is on the *T*2 or *T*3 site. As seen, the interslab dimer cleavage absorbs the extra electrons and preserves the intraslab dimers and integrity of the slabs themselves.

Using chemical considerations, it should also be possible to predict site preference for the P atoms. Three models are considered here: in Model **1**, the 4 P atoms occupy one-

half of the *T*1 sites in a way that the nearest P neighbors are only Si1 atoms; in Models **2** and **3**, the P atoms are on the *T*2 and *T*3 sites, respectively. The environments around the *T*2 and *T*3 sites are quite similar, but significantly different from that around the *T*1 site. Thus, it should be possible to differentiate between the preference of P for the *T*1 site and the *T*2/*T*3 site. Distribution of different atoms over two or more independent sites is known as a coloring problem.[38] While the entropy contribution to the Gibbs free energy always favors statistical distribution of a mixture of elements, electronic and geometric factors usually dictate atomic separation.[39]

In "Gd_5Si_3P" size effects seem to be less important than electronic effects. According to covalent radii (r_{cov}(Si) = 1.17 Å; r_{cov}(P) = 1.10 Å),[20] P atoms should prefer sites with smaller coordination volumes while also leading to smaller unit cell volumes than in Gd_5Si_4. Indeed, unit cell volumes decrease with P substitution. With regard to electronic effects, the two itinerant electrons indicated in the formulations of "Gd_5Si_3P" above will partially occupy σ_p* antibonding states within the intraslab *T*2-*T*3 dimers. Because P is more electronegative than Si (χ_P = 2.25 vs χ_{Si} = 1.92),[40] its σ_p* antibonding states within the intraslab dimers would be lower in energy and more populated than those of Si. Thus, having P atoms on the *T*1 site results in a lower electronic energy than placing P atoms on the *T*2 or *T*3 sites. This simple reasoning is supported by the band structure calculations. The TB-LMTO-ASA analysis predicts that the total electronic energy of Model **1** will be 2.56 eV/unit cell lower than that of Model **2** and 3.64 eV/unit cell lower than that of Model **3**. Although there is no experimental proof at this stage to substantiate our conclusions for the site preferences in $Gd_5Si_{4-x}P_x$, the previous studies on

the $Gd_5Si_2Ge_2$[41] and $Gd_5Si_{4-x}Sn_x$[18] phases point to a very good agreement between the theoretical findings and experimental data.

Calculated DOS and COHP curves for the Model **1** of "Gd_5Si_3P" are presented in Figures 3.4 and 3.5. Presence of the P and Si monomers at the *T*1 sites with very weak *T*1-*T*1 bonding affects both the DOS and COHP curves. The two most prominent features of the DOS of "Gd_5Si_3P," as compared to that of Gd_5Si_4, are (i) appearance of an additional DOS peak around -10 eV and (ii) disappearance of the pseudogap. These changes in the DOS are direct consequences of the dimer breaking, with the first feature also reflecting the higher electronegativity of P as compared to Si. The peak around -10 eV originates almost entirely from the nonbonding P1 3*s* orbitals, with its counterpart Si1 nonbonding 3*s* orbitals overlapping the antibonding σ_s* states of the Si2-Si3 dimers. The peak position at -10 eV mirrors the energy of the P1 3*s* orbitals, as the weak interaction between P1 and Si1 is not expected to shift the P1 3*s* states to significantly lower energies. A small energetic dispersion is also expected for the P1 and Si1 3*p* states, which, in turn, leads to a larger DOS at lower energies and, thus, elimination of the pseudogap.

The *T*1-*T*1 dimer cleavage leads to strengthening of the Gd- *T*1 bonds in "Gd_5Si_3P." The COHP calculations show appearance of the additional Gd-*T*1 bonding states around -0.7 eV (Figure 3.5). Such reinforcement of the Gd-*T*1 interactions is expected from chemical considerations, as the *T*1 electrons freed from the *T*1-*T*1 bonds are donated to the Gd-*T*1 interactions. Integrated COHP (-ICOHP) values calculated for Gd-*T*1 interactions are significantly larger for "Gd_5Si_3P" than for Gd_5Si_4 (13.63 vs 8.99

eV/cell). An increase in Gd-*T*1 bonding correlates well with the changes in Gd-*T*1 interatomic distances (Table 3.4). During the Gd_5Si_4-to-$Gd_5Si_{2.75}P_{1.25}$ transition, the average Gd-*T*1 bond distance decreases from 3.108 Å in Gd_5Si_4 to 3.082 Å in $Gd_5Si_{2.75}P_{1.25}$. In addition, Gd-Gd interactions become weaker during the transition as represented by the average interslab Gd-Gd distances and calculated –ICOHP values (3.67 vs 4.86 eV/cell for "Gd_5Si_3P" and Gd_5Si_4, respectively). Thus, there is an energetic tradeoff in interactions during the structural transformation: as the interslab *T*1-*T*1 and Gd-Gd interactions became weaker, the Gd-*T*1 bonds became stronger.

Table 3.4. Average interatomic distances in Gd_5Si_4 and $Gd_5Si_{2.75}P_{1.25}$[a]

bonds	Gd_5Si_4 *d*, Å	$Gd_5Si_{2.75}P_{1.25}$ *d*, Å
Distances within the slabs		
*T*2-*T*3 (×1)	2.484	2.529
Gd-*T*2 (×8)	3.056	3.064
Gd-*T*3 (×8)	3.077	3.063
Gd-Gd (×10)	3.885	3.889
Distances between the slabs		
*T*1-*T*1 (×1)	2.491	3.741
Gd-*T*1 (×16)	3.108	3.082
Gd-Gd (×5)	3.871	4.037

[a] Number of bonds per formula unit is given in parentheses

The *T*1-*T*1 bonds appear to break up abruptly with an increasing VEC in $Gd_5Si_{4-x}P_x$. Only two atomic arrangements, one with dimers intact ($d_{T1\text{-}T1}$ = 2.49 Å in Gd_5Si_4) and the other with completely broken dimers ($d_{T1\text{-}T1}$ = 3.74 Å in $Gd_5Si_{2.75}P_{1.25}$), are observed in this system. Indirectly, the composite nature of the single crystals from the two-phase region supports this argument. Also, the powder diffraction data (Figure 3.1) indicate existence only of the Gd_5Si_4- and Sm_5Ge_4-type phases, and no phases with intermediate

unit cell parameters and, thus, no intermediate dimer distances were seen, even in the two-phase region. Small variations in the lattice constants for the Sm_5Ge_4-type phases may indicate some variations in the interslab distances, but these variations are expected to be small and the bonds are expected to be fully broken. At present, it is not fully understood why there is a sudden change in the interslab *T*1-*T*1 interactions instead of gradual bond stretching. It can be assumed that a structure with intermediate *T*1-*T*1 distances is unstable with respect to the Gd_5Si_4- and Sm_5Ge_4- type structures. A similar, abrupt dimer cleavage was observed in the $Gd_5Ga_xGe_{4-x}$ system, where introducing an extra 0.3 electron into Gd_5GaGe_3 ($d_{T1\text{-}T1}$ = 2.93 Å) leads to complete dimer cleavage in $Gd_5Ga_{0.7}Ge_{3.3}$ ($d_{T1\text{-}T1}$ = 3.46 Å) and to a firstorder phase transition.[17] Analysis of the lattice constants of the $Gd_5Si_xGe_{4-x}$ compounds also points to an abrupt dimer cleavage as a function of Si content,[42] which supports the argument that in some systems stabilization of intermediate structures may not be possible.

3.4.4 Structure vs electron count in RE_5T_4 phases

The current work on the $Gd_5Si_{4-x}P_x$ system clearly demonstrates that the bonding within the interslab *T*-*T* dimers can be disrupted through an increase in the VEC. As discussed above, the atomic sizes are not as influential as electronic factors, i.e., energy band filling and electronegativity, toward controlling these dimer interactions. In fact, if the electronic effects would be neglected, a somewhat smaller size of P would lead to shorter *T*-*T* distances. Additionally, $Gd_5Si_{2.75}P_{1.25}$ extends the existence of RE_5T_4 phases (*RE* is a rare-earth metal, *T* is a *p*-element) with a Sm_5Ge_4-type structure to the VEC of

32.5 e⁻/formula unit, above 31 e⁻ as previously observed.

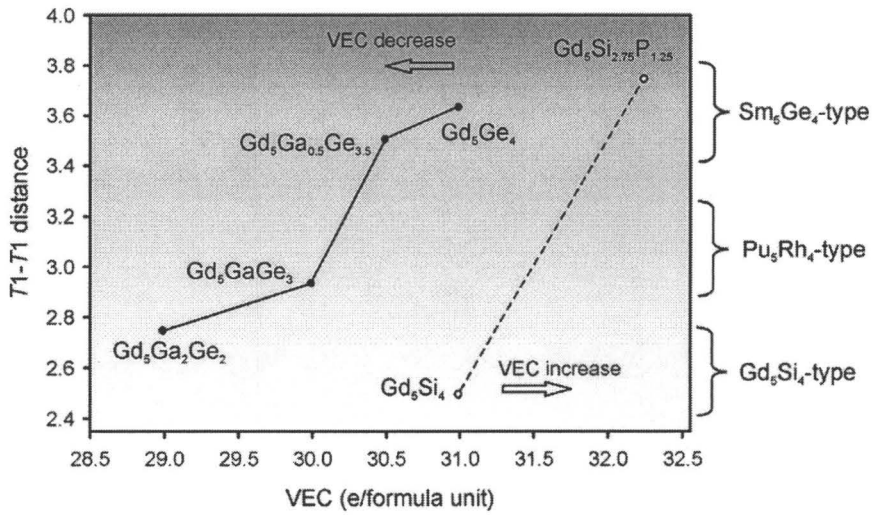

Figure 3.6. Interslab dimer distances in the $Gd_5Ga_xGe_{4-x}$ and $Gd_5Si_{4-x}P_x$ phases as a function of valence electron concentration. Only single crystal data from single-phase samples are used. Data for $Gd_5Ga_xGe_{4-x}$ are taken from ref 17. The existence ranges for the three structure types are shown

The electron-richer $RE_5T_2Sb_2$ phases (RE = Y, Tb, Dy, Ho, Er, T = Si, Ge) have been also reported, but they adopt a different orthorhombic structure (space group *Cmca*), which is an ordered version of the Eu_5As_4 structure.[43] While being similar to the Sm_5Ge_4 structure such that there are no interslab dimers, this new orthorhombic structure has not exhibited any phase transition to reform dimers, and the absence of *T*/Sb mixing in their atomic arrangements suggests a simple structural adaptation for the larger Sb atoms. In $RE_5T_2Sb_2$, the Sb atoms are located between the slabs, while T atoms form dimers within the slabs. As discussed for "Gd_5Si_3P," the more electronegative atoms prefer to occupy sites with no homonuclear bonds in order to minimize the total electronic energy. If the

two sites in $RE_5T_2Sb_2$ could be occupied by both Si and Sb, then Si would be expected to fill in the interslab sites and Sb to form intraslab dimers. Therefore, the $RE_5T_2Sb_2$ structures adapt to the larger Sb atoms rather than respond to the increased VEC. This type of structural adaptation was also observed in $Gd_5Si_{4-x}Sn_x$, where substitution of Si with electron-equivalent, but larger, Sn led to dimer cleavage.[18] There are two contradictory reports regarding the existence of $Gd_5Si_2Sb_2$, with one claiming that the phase cannot be obtained[43] and the other one stating that $Gd_5Si_2Sb_2$ adopts a Sm_5Ge_4-type structure as observed from X-ray powder diffraction (however, the diffraction profile was not provided).[44] We will refrain from discussing $Gd_5Si_2Sb_2$ until further studies are done.

The current study on the $Gd_5Si_{4-x}P_x$ system complements the previous studies on the $Gd_5Ga_xGe_{4-x}$ system. In $Gd_5Ga_xGe_{4-x}$, the lower VEC led to reforming the interslab $T1$-$T1$ dimers by substituting Ga for Ge in the 31 e^- Gd_5Ge_4 phase, which adopts the Sm_5Ge_4-type structure. On the other hand, in $Gd_5Si_{4-x}P_x$, the higher VEC manifested breaking the interslab $T1$-$T1$ dimers in the 31 e^- Gd_5Si_4 phase by replacing Si with P atoms. Figure 3.6 shows the dependence of the interslab $T1$-$T1$ dimer distances as a function of VEC for various Gd_5T_4 single crystals. While being similar in its nature, the two approaches differ with respect to the targeted phases and potential outcome. In particular, in a structure with the interslab dimers intact, an increase in the VEC is expected to break the dimers. Obviously, doing so in a phase with already broken dimers will have no structural consequences, and, thus, the opposite direction, namely reduction in the VEC, has to be pursued. We believe that the two approaches can be extended to other RE_5T_4 phases and may be utilized in predicting and, subsequently, obtaining new

phases.

3.5 Conclusions

Structural transformations in the $Gd_5Si_{4-x}P_x$ system prove that a higher VEC can be used to break interslab *T*-*T* dimers in Gd_5Si_4-type phases and, thus, to induce a Gd_5Si_4-to-Sm_5Ge_4 phase change. Also, the existence of the Sm_5Ge_4-type phases is extended to VEC values larger than 31 e^-/formula unit. The driving force for the phase transition in $Gd_5Si_{4-x}P_x$ and RE_5T_4 phases, in general, is optimization of interslab *T*-*T* bonding, which leads to *T*-*T* dimer cleavage at higher VEC values and their recombination at lower VEC values.

3.6 Acknowledgment

This work was supported by a Discovery Grant from the Natural Sciences and Engineering Research Council of Canada.

Supporting information available: Supplementary crystallographic data (cif). This material is available free of charge via the Internet at http://pubs.acs.org.

References

[1] V. K. Pecharsky, K. A. Gschneidner Jr., *Phys. Rev. Lett.* **1997**, *78*, 4494–4497.

[2] C. B. Zimm, A. Sternberg, A. G. Jastrab, A. M. Boeder, L. M. Lawton Jr., J. J. Chell, *Rotating bed magnetic refrigeration apparatus.* US patent 6526759, **2003**.

[3] C. Zimm, A. Boeder, J. Chell, A. Sternberg, A. Fujita, S. Fujieda, K. Fukamichi, *Inter. J. Refrig.* **2006**, *29*, 1302–1306.

[4] V. K. Pecharsky, K. A. Gschneidner Jr., *J. Alloys Compd.* **1997**, *260*, 98–106.

[5] O. Tegus, E. Brick, K. H. J. Buschow, F. R. de Boer, *Nature* **2002**, *415*, 150–152.

[6] V. K. Pecharsky, K. A. Gschneidner Jr., *Springer Ser. Mater. Sci.* **2005**, *79*, 199–222.

[7] W. Choe, V. K. Pecharsky, A. O. Pecharsky, K. A. Gschneidner Jr., V. G. Young Jr., G. J. Miller, *Phys. Rev. Lett.* **2000**, *84*, 4617– 4620.

[8] K. A. Gschneidner Jr., V. K. Pecharsky, A. O. Pecharsky, V. V. Ivtchenko, E. M. Levin, *J. Alloys Compd.* **2000**, *303-304*, 214–222.

[9] H. Huang, A. O. Pecharsky, V. K. Pecharsky, K. A. Gschneidner Jr., *Adv. Cryog. Eng.* **2002**, *48*, 11–18.

[10] V. K. Pecharsky, A. O. Pecharsky, K. A. Gschneidner Jr., *J. Alloys Compd.* **2002**, *344*, 362–368.

[11] Y. I. Spichkin, V. K. Pecharsky, K. A. Gschneidner Jr., *J. Appl. Phys.* **2001**, *89*, 1738–1745.

[12] V. K. Pecharsky, A. O. Pecharsky, Y. Mozharivskyj, K. A. Gschneidner Jr., G. J. Miller, *Phys. Rev. Lett.* **2003**, *91*, 207205/207201–204.

[13] K. Ahn, A. O. Tsokol, Y. Mozharivskyj, K. A. Gschneidner Jr., V. K. Pecharsky, *Phys. Rev. B* **2005**, *72*, 054404/054401–11.

[14] H. F. Yang, G. H. Rao, G. Y. Liu, Z. W. Ouyang, W. F. Liu, X. M. Feng, W. G. Chu, J. K. Liang, *Phys. B (Amsterdam)* **2003**, *325*, 293–299.

[15] H. F. Yang, G. H. Rao, G. Y. Liu, Z. W. Ouyang, W. F. Liu, X. M. Feng, W. G. Chu, J. K. Liang, *J. Alloys Compd.* **2003**, *348*, 150–156.

[16] H. F. Yang, G. H. Rao, G. Y. Liu, Z. W. Ouyang, W. F. Liu, X. M. Feng, W. G. Chu, J. K. Liang, *J. Alloys Compd.* **2002**, *346*, 190–196.

[17] Y. Mozharivskyj, W. Choe, A. O. Pecharsky, G. J. Miller, *J. Am. Chem. Soc.* **2003**, *125*, 15183–15190.

[18] Y. Mozharivskyj, A. O. Tsokol, G. J. Miller, *Z. Kristallogr.* **2006**, *221*, 493–501.

[19] L.-M. Wu, S.-H. Kim, D.-K. Seo, *J. Am. Chem. Soc.* **2005**, *127*, 15682–15683.

[20] L. C. Pauling, *The Nature of the Chemical Bond and the Structure of Molecules and Crystals: An Introduction to Modern Structural Chemistry*, 3rd ed.; Cornell University Press: Ithaca, NY, **1960**.

[21] K. A. Gschneidner Jr., V. K. Pecharsky, *J. Appl. Phys.* **1999**, *85*, 5365–5368.

[22] Y. Mozharivskyj, A. O. Pecharsky, V. K. Pecharsky, G. J. Miller, *J. Am. Chem. Soc.* **2005**, *127*, 317–324.

[23] B. A. Hunter, C. J. Howard, *Australian Nuclear Science and Technology Organization*: Menai: Austalia, **2000**.

[24] *STOE & Cie GmbH*, Darmstadt: Germany, **2004**.

[25] G. M. Sheldrick, *SHELXL97 and SHELXS97*, University of Gottingen: Germany, **1997**.

[26] W. Choe, G. J. Miller, J. Meyers, S. Chumbley, A. O. Pecharsky, *Chem. Mater.* **2003**, *15*, 1413–1419.

[27] O. K. Anderson, *Phys. Rev. B* **1986**, *34*, 2439.

[28] O. Jepsen, A. Burkhardt, O. K. Anderson *The TB-LMTO-ASA Program, Version 4.7, Max-Planck-Institut für Festkörperforschung*; Stuttgart: Germany **1999**.

[29] O. K. Anderson, O. Jepsen, *Phys. Rev. Lett.* **1984**, *53*, 2571.

[30] O. K. Anderson, O. Jepsen, D. Glötzel, In *Highlights of condensed matter theory*; Bassani, F., Fumi, F., Tosi, M., Eds.; Lambrecht, W. R. L.: New York, 1985.

[31] O. Jepsen, O. K. Anderson, *Z. Phys. B* **1995**, *97*, 35.

[32] P. E. Blöchl, O. Jepsen, O. K. Anderson, *Phys. Rev. B* **1994**, *49*, 16223.

[33] J. Le Roy, J. M. Moreau, D. Paccard, E. Parthe, *Acta Crystallogr. B* **1978**, *B34*, 3315–3318.

[34] F. Holtzberg, R. J. Gambino, T. R. McGuire, *J. Phys. Chem. Solids* **1967**, *28*, 2283–2289.

[35] S. Misra, G. J. Miller, *J. Solid State Chem.* **2006**, *179*, 2290–2297.

[36] G. J. Miller, In *Chemistry, Structure, and Bonding of Zintl Phases and Ions*; S. M. Kauzlarich, Ed., VCH Publishers, Inc.: New York, **1996**; pp 1-59.

[37] Y. Mozharivskyj, A. O. Pecharsky, V. K. Pecharsky, G. J. Miller, J. Gschneidner, A. Karl, *Phys. Rev. B* **2004**, *69*, 144102.

[38] G. J. Miller, *Eur. J. Inorg. Chem.* **1998**, *5*, 523–536.

[39] Y. Mozharivskyj, H. F. Franzen, *J. Alloys Compd.* **2001**, *319*, 100–107.

[40] J. B. Mann, T. L. Meek, L. C. Allen, *J. Am. Chem. Soc.* **2000**, *122*, 2780–2783.

[41] G. D. Samolyuk, V. P. Antropov, *J. Appl. Phys.* **2002**, *91*, 8540–8542.

[42] A. O. Pecharsky, K. A. Gschneidner Jr., V. K. Pecharsky, C. E. Schindler, *J. Alloys Compd.* **2002**, *338*, 126–135.

[43] A. Y. Kozlov, V. V. Pavlyuk, V. M. Davydov, *Intermetallics* **2004**, *12*, 151–155.

[44] R. Nirmala, A. V. Morozkin, S. K. Malik, *Europhys. Lett.* **2005**, *72*, 652–657.

Chapter 4. Magnetic transitions in the $Gd_5Si_{4-x}P_x$ (x = 0.5, 0.75, 1.25) phases. Magnetocaloric effect of the $Gd_5Si_{2.75}P_{1.25}$ phase

This chapter contains the manuscript "Magnetic transitions in the $Gd_5Si_{4-x}P_x$ (x = 0.5, 0.75, 1.25) phases. Magnetocaloric effect of the $Gd_5Si_{2.75}P_{1.25}$ phase", published in the Solid State Sciences (*Solid State Sci.* **2009**, *11*, 1941–1944). The candidate completed all of the experimental synthesis, data collection, processing and interpretation and prepared the manuscript.

Magnetic transitions in the $Gd_5Si_{4-x}P_x$ (x = 0.5, 0.75, 1.25) phases.

Magnetocaloric effect of the $Gd_5Si_{2.75}P_{1.25}$ phase

Volodymyr Svitlyk and Yurij Mozharivskyj

Department of Chemistry, McMaster University, Hamilton, ON, L8S 4M1, Canada

4.1 Abstract

The $Gd_5Si_{2.75}P_{1.25}$ phase with all interslab Si/P–Si/P dimers broken (Sm_5Ge_4-type structure) undergoes a ferromagnetic transition at 184 K. For this phase, the magnetocaloric effect in terms of the magnetic entropy change, ΔS, reaches the maximum value of -7.8 J/kg K at 177 K. Absence of a temperature-dependant structural transition, as confirmed by the low-temperature single crystal diffraction studies, together with the moderate value of ΔS points to the presence of a conventional magnetocaloric effect. $Gd_5Si_{3.5}P_{0.5}$ and $Gd_5Si_{3.25}P_{0.75}$, which are composites of the Gd_5Si_4- (all Si/P–Si/P dimers intact) and Sm_5Ge_4-type phases, possess two magnetic transitions associated with the two-phases. Introduction of P into Gd_5Si_4 lowers the Curie temperature from 336 K to 332 K in $Gd_5Si_{3.25}P_{0.75}$.

4.2 Introduction

The RE_5T_4 family (RE – rare earth element, T – p-element) became a subject of intense investigation after the discovery of a giant magnetocaloric effect (GMCE) in $Gd_5Si_2Ge_2$.[1] The optimally prepared $Gd_5Si_2Ge_2$ phase exhibits an isothermal entropy change, ΔS, of -36 J/kg K around the 272 K temperature[2] at which the coupled magneto-

structural transition occurs. This reversible first-order transition is accompanied by the cleavage/formation of the interslab Si/Ge–Si/Ge (*T*–*T*) dimers[3] and significantly enhances the magnetic entropy change.[4]

It has been shown that formation or cleavage of the interslab *T*–*T* dimers in the RE_5T_4 phases can be controlled through the valance electron count (VEC). For instance, substitution of Ga for Ge in Gd_5Ge_4 (VEC = 31 e^-) with all interslab *T*–*T* dimers broken reforms the *T*–*T* bonds in $Gd_5Ga_xGe_{4-x}$ (x = 1–2, VEC = 29–30 e^-/f.u.).[5] The *T*–*T* dimers could be also formed in $La_{5-x}Ca_xGe_4$ and $Ce_{5-x}Ca_xGe_4$ after the substitution of divalent Ca for trivalent La and Ce.[6] Recently, the VEC approach has been successfully used to break the interslab dimers. Substitution of Si in the Gd_5Si_4 phase (VEC = 31 e^-, all Si–Si dimers intact) with size-equivalent P lead to the cleavage of the interslab dimers in $Gd_5Si_{2.75}P_{1.25}$ (VEC = 32.5 e^-).[7] As confirmed by the electronic structure calculations, the origin of this structural transition stems from the population of antibonding states within the *T*–*T* bonds. At the critical P amount of 1.25/f.u., the *T*–*T* dimers, which now can be represented as Si/P–Si/P ones, break to accommodate the extra electron density.[7]

$Gd_5Si_{2.75}P_{1.25}$ is attractive as a potential refrigerant material. If present, a temperature-dependent first-order magneto-structural transition originating from the formation of the Si/P–Si/P dimers could yield a GMCE in the phase. In this work we report on the magnetic properties of the $Gd_5Si_{4-x}P_x$ ($0 \leq x \leq 1.25$) series and on the magnetocaloric effect of the $Gd_5Si_{2.75}P_{1.25}$ phase.

4.3 Experimental

4.3.1 Synthesis, X-ray structure analysis, single crystal growth and temperature treatment

Starting materials were gadolinium (99.99 wt%, distilled grade, Metall Rare Earth Limited, China), silicon (99.999 wt%, Alfa Aesar) and phosphorus (99.999 wt%, Puratronic, Alfa Aesar). A GdSi precursor was synthesized by arc-melting of elemental Gd and Si. The GdSi alloy was ground in an Ar-filled drybox and mixed with ground phosphorus in the 1:1 molar ratio. The resulting GdSi–P mixture was pressed, sealed in an evacuated silica tube, heated to 400 at 50 °C/h followed by a 12 h dwell, then heated to 800 °C at 50 °C/h followed by a 48 h dwell and quenched in cold water. P was found to substitute for Si in the GdSi phase to yield a mixture of GdP and elemental Si, as concluded from the X-ray powder diffraction. The GdP–Si mixture was pressed into pellets and combined with corresponding amounts of elemental Gd and Si to yield the $Gd_5Si_{3.5}P_{0.5}$, $Gd_5Si_{3.25}P_{0.75}$, Gd_5Si_3P, $Gd_5Si_{2.85}P_{1.15}$ and $Gd_5Si_{2.75}P_{1.25}$ compositions and arc-melted at least three times. No significant losses of P could be observed during the arc-melting, which can be attributed to an ionic nature of the Gd-P bonds in the GdP binary. $Gd_5Si_{2.75}P_{1.25}$ was prepared in order to examine its magnetocaloric properties, as discussed in the Introduction. $Gd_5Si_{3.5}P_{0.5}$, $Gd_5Si_{3.25}P_{0.75}$ and Gd_5Si_3P samples were synthesized in order to track the changes in magnetic properties as a function of composition. $Gd_5Si_{2.85}P_{1.15}$ was prepared in order to establish finer boundaries for the formation of the Sm_5Ge_4-type phase. All samples were annealed in evacuated silica tubes at 800 °C for 2 weeks.

X-ray powder diffraction data were obtained on a PANalytical X'Pert Pro diffractometer with a linear X'Celerator detector using the CoK_α radiation. Quantitative phase analysis was performed with the FULLPROF software[8] (Table 4.1). The Gd_5Si_3P sample had significant amounts of the GdP (NaCl-type structure) and Gd_5Si_3 (Mn_5Si_3-type) impurities (ca. 25 mass % in total). The $Gd_5Si_{2.75}P_{1.25}$ sample was found to consist only of the Sm_5Ge_4-type phase along with the GdP and Gd_5Si_3 impurities (9.5 mass% in total). Although all phases were synthesized by arc-melting under similar conditions, it was impossible to maintain the same temperature and, especially, a cooling rate during the arc-melting for the different trials. The cooling conditions may play a crucial role in the formation of the GdP impurity, which melts congruently above 2500 °C.[9]

Table 4.1. X-ray phase analysis of the $Gd_5Si_{3.5}P_{0.5}$, $Gd_5Si_{3.25}P_{0.75}$, Gd_5Si_3P and $Gd_5Si_{2.75}P_{1.25}$ samples

Composition	Sample	Gd_5Si_4/Sm_5Ge_4-type phases, mass %[a]	Secondary phases, total mass %	*c/a* for Gd_5Si_4/Sm_5Ge_4-type phases
$Gd_5Si_{3.5}P_{0.5}$	Crystal	~ 95/5	Not detected	1.0346(1)/1.0125(2)
$Gd_5Si_{3.25}P_{0.75}$	Powder	~ 50/50	GdP, Gd_5Si_3, ~ 10%	1.0333(2)/1.0118(2)
Gd_5Si_3P	Powder	~ 80/20	GdP, Gd_5Si_3, ~ 25%	1.0350(4)/1.0104(1)
$Gd_5Si_{2.75}P_{1.25}$	Powder	Not detected/100	GdP, Gd_5Si_3, ~ 9.5%	n.a./1.0098(1)

[a] The total mass of the Gd_5Si_4- and Sm_5Ge_4-type phases was normalized to 100%

To reduce amounts of the GdP and Gd_5Si_3 impurities, the Gd_5Si_3P sample was annealed at 400, 600, 800, 1000, 1200 and 1400 °C. Samples sealed in evacuated silica tubes were annealed at 400 and 600 °C for 4 weeks, at 800 and 1000 °C for 2 weeks in conventional box furnaces. For annealing at 1000 °C the sample was wrapped in Ta foil

to prevent undesired reactions with silica. Heat treatment at 1200 and 1400 °C was performed for 4 h under a dynamic vacuum of $0.5x10^{-5}$ Torr in the induction furnace. Phase analysis showed no changes in the sample composition for treatments at 400, 600 and 800 °C. Samples annealed at 1000, 1200 and especially at 1400 °C showed increased concentrations of the GdP and Gd_5Si_3 impurities. Disproportionation of the Gd_5Si_3P phase at high temperatures indicates that the phase is likely to be stable only below 1000 °C.

A tri-arc Czochralski single crystal growth technique[10] was employed for the $Gd_5Si_{3.5}P_{0.5}$, $Gd_5Si_{3.25}P_{0.75}$, Gd_5Si_3P and $Gd_5Si_{2.75}P_{1.25}$ samples in order to obtain pure and monocrystalline Gd_5Si_4- or Sm_5Ge_4-type phases. An eight millimeter-long single crystal was grown successfully for the $Gd_5Si_{3.5}P_{0.5}$ sample (Fig. 4.1) but this technique did not produce desired results for the phases with the higher P content, i.e. $Gd_5Si_{3.25}P_{0.75}$, Gd_5Si_3P and $Gd_5Si_{2.75}P_{1.25}$. The latter samples contained the GdP phase as a major phase. A small part of the $Gd_5Si_{3.5}P_{0.5}$ crystal was chipped off and analyzed on the STOE IPDSII diffractometer.

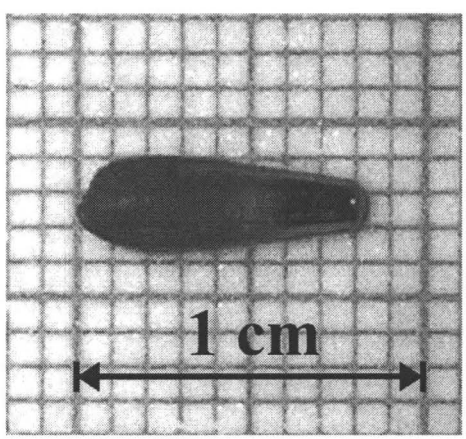

Figure 4.1. A single crystal obtained by the tri-arc Czochralski technique from the $Gd_5Si_{3.5}P_{0.5}$ sample

As shown for the $Gd_5Ga_xGe_{4-x}$ and $Gd_5Si_{4-x}P_x$ series,[5,7] the Gd_5Si_4- and Sm_5Ge_4-type phases can be distinguished by the *c*/*a* cell parameter ratio. For the Gd_5Si_4-type phases with interslab *T*–*T* bonds intact, *c*/*a* is close to 1.03, while for the Sm_5Ge_4-type ones with *T*–*T* dimers broken, this ratio is around 1.01. The *c*/*a* ratios and phase analysis of the $Gd_5Si_{3.5}P_{0.5}$, $Gd_5Si_{3.25}P_{0.75}$, Gd_5Si_3P and $Gd_5Si_{2.75}P_{1.25}$ samples are summarized in Table 4.1.

4.3.2 Magnetic measurements

Magnetization in a field-cooled (FC) mode for the monocrystalline $Gd_5Si_{3.5}P_{0.5}$, polycrystalline $Gd_5Si_{3.25}P_{0.75}$ and $Gd_5Si_{2.75}P_{1.25}$ samples was measured on a Quantum Design SQUID magnetometer at 100 Oe field between 375 and 2 K (Fig. 4.2, Table 4.2). Magnetization of the Gd_5Si_3P sample was not measured due to the significant amounts of the secondary phases. The magnetocaloric effect for $Gd_5Si_{2.75}P_{1.25}$ was evaluated from the magnetization vs. field (M vs. H) curves measured around the ordering temperature with 5 K increments. The magnetic field changed from 0 to 50 kOe in 2 kOe steps (Fig. 4.3).

4.4 Results and discussion

4.4.1 Phase compositions and magnetic properties of $Gd_5Si_{3.5}P_{0.5}$, $Gd_5Si_{3.25}P_{0.75}$ and $Gd_5Si_{2.75}P_{1.25}$

According to the X-ray analysis, the $Gd_5Si_{3.5}P_{0.5}$, $Gd_5Si_{3.25}P_{0.75}$, Gd_5Si_3P and $Gd_5Si_{2.85}P_{1.15}$ samples were found to consist of two phases, one with all *T*–*T* dimers intact (Gd_5Si_4-type structure, *c*/*a* ~ 1.03) and the other with all dimers broken (Sm_5Ge_4-type

structure, $c/a \sim 1.01$). While the phase analysis indicates that the homogeneity region for the Gd_5Si_4-type phase does not extend to $x = 0.5$, the unit cell parameters and magnetic data suggest that the P amount in the Gd_5Si_4-type phase increases slightly with the loading composition. Thus, it can be assumed that the phase equilibrium is not reached during the arc-melting and annealing. Since no Gd_5Si_4-type phase could be detected in the $Gd_5Si_{2.75}P_{1.25}$ diffraction pattern, the limiting composition for the Sm_5Ge_4-type phase must be close to the $Gd_5Si_{2.75}P_{1.25}$ one. The homogeneity ranges established during the current studies are similar to the ones observed previously.[7]

Table 4.2. Curie temperatures, T_c, for the Gd_5Si_4- and Sm_5Ge_4-type phases in the $Gd_5Si_{3.5}P_{0.5}$, $Gd_5Si_{3.25}P_{0.75}$ and $Gd_5Si_{2.75}P_{1.25}$ samples from the magnetization data

Sample	T_C, Gd_5Si_4-type phase	T_C, Sm_5Ge_4-type phase
$Gd_5Si_{3.5}P_{0.5}$	336 K	~190 K
$Gd_5Si_{3.25}P_{0.75}$	332 K	188 K
$Gd_5Si_{2.75}P_{1.25}$	330 K	184 K

A Gd_5Si_4-type phase was found to be dominant in the $Gd_5Si_{3.5}P_{0.5}$ samples prepared both by arc-melting and tri-arc single crystal growth. While the crystal grown by the tri-arc Czochralski method had well-defined faces and visually appeared to be a single face, in reality it contained the Gd_5Si_4- and Sm_5Ge_4-type phases as established from the single crystal X-ray diffraction. During the structural refinement, the composite nature of the crystal manifested itself as a pear-like distribution of electron densities around the atomic sites associated with the Gd_5Si_4-type structure. Such unusual crystal behavior has been observed previously in the $Gd_5Si_{4-x}P_x$ series[7] and is believed to result from the

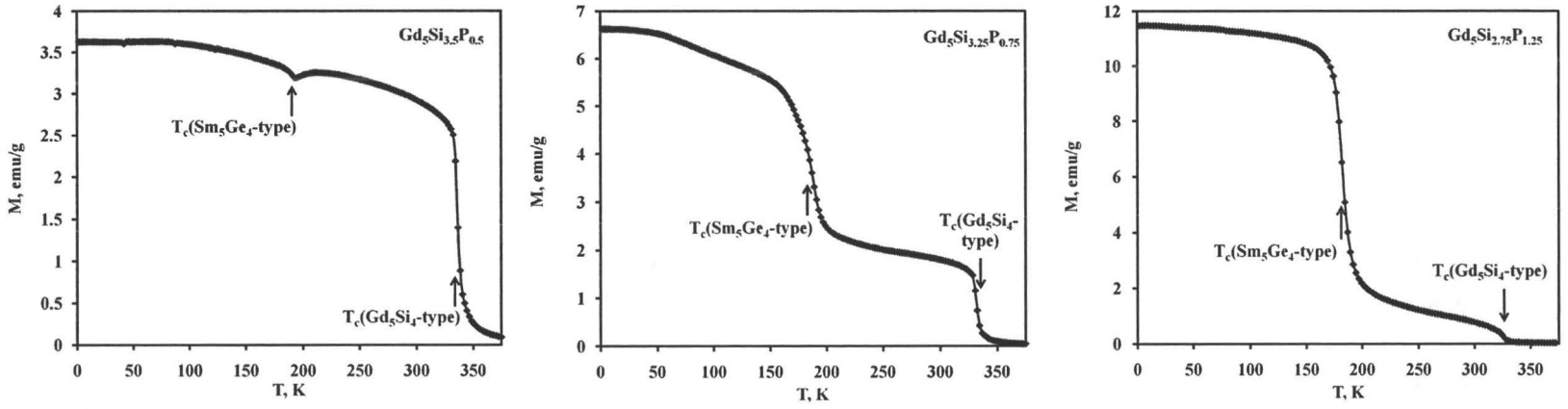

Figure 4.2. Magnetic transitions in the $Gd_5Si_{3.5}P_{0.5}$, $Gd_5Si_{3.25}P_{0.75}$ and $Gd_5Si_{2.75}P_{1.25}$ samples

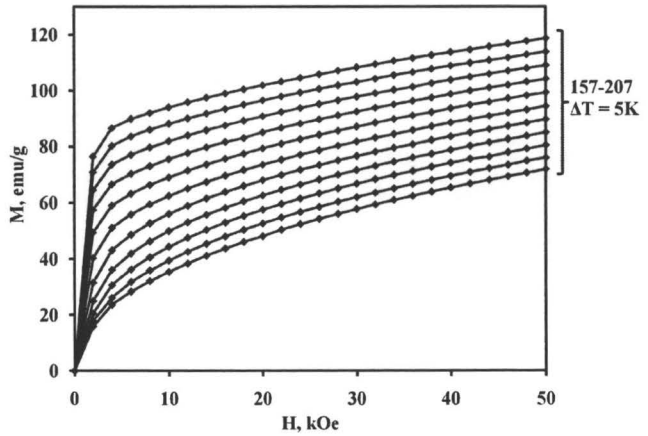

Figure 4.3. Magnetization vs. field (M vs. H) measurements around the Curie temperature for $Gd_5Si_{2.75}P_{1.25}$

microscopic compositional inhomogeneities. The grown crystal had a lower amount of the Sm_5Ge_4-type phase as compared to the arc-melted sample, therefore only its data are presented here.

Because of the smaller covalent radius of P vs. Si (r_{cov} equals to 1.10 and 1.17 Å, respectively[11]), the unit cell volume of the Gd_5Si_4-type phase in the $Gd_5Si_{3.5}P_{0.5}$ sample is expected to decrease upon the P substitution, providing the structure remains the same. Indeed, a decrease in the cell volume from 854.9(1) for Gd_5Si_4 to 853.0(1) $Å^3$ indicates existence of a Si/P homogeneity region. The main magnetic transition at 336 K (Fig. 4.2, at the left) corresponds to the Gd_5Si_4-type phase, and matches the literature value of 336 K for the Gd_5Si_4 phase.[12] Such magnetic behavior implies that the current P concentration has no or little effect on the magnetic interactions in the Gd_5Si_4-type phase. Presence of the Sm_5Ge_4-type phase in the $Gd_5Si_{3.5}P_{0.5}$ sample is verified by a feature around 190 K on the magnetization curve.

The $Gd_5Si_{3.25}P_{0.75}$ sample contained almost equal amounts of Gd_5Si_4- and Sm_5Ge_4-type phases with a GdP and Gd_5Si_3 as a secondary phases (ca. 10% mass). The cell volume of the Gd_5Si_4- type phase decreased to 850.7(2) $Å^3$ indicating a increased P content in the phase. The Curie temperature for the Gd_5Si_4-type structure shifted from 336 to 332 K (Fig. 4.2, in the centre). The Sm_5Ge_4-type phase, whose amount increased as compared to the $Gd_5Si_{3.5}P_{0.5}$ sample, has a well-pronounced ferromagnetic transition at 188 K.

The $Gd_5Si_{2.75}P_{1.15}$ sample found to have Sm_5Ge_4-type phase as a major component with a small amount of the Gd_5Si_4-type phase. This implies that the $Gd_5Si_{2.75}P_{1.15}$

composition still falls in the two-phase region. Amount of the Gd_5Si_4-type phase could not be estimated reliably by the mean of the powder X-ray diffraction due to its small amount.

The $Gd_5Si_{2.75}P_{1.25}$ sample, which showed no signs of the Gd_5Si_4- type phase on the powder diffraction pattern, did posses a weak magnetic transition around 330 K (Fig. 4.2, at the right). This indicates the presence of a small amount of the Gd_5Si_4-type phase in the $Gd_5Si_{2.75}P_{1.25}$ sample at the levels not detectable by the X-ray analysis. The Gd_5Si_4-type impurity is likely to result from the formation of GdP, which shifts the effective composition to a P poorer region. The ferromagnetic transition at 184 K corresponds to the $Gd_5Si_{2.75}P_{1.25}$ phase (Sm_5Ge_4-type structure). A decrease in the Curie temperature as compared to $Gd_5Si_{3.25}P_{0.75}$ can be attributed to a different Si/P ratio in the sample.

The quantitative phase analysis of the $Gd_5Si_{4-x}P_x$ samples could not be performed precisely by the means of the powder X-ray diffraction, due to the presence of the preferred orientation, different level of crystallinity for different phases and partial peak overlap. Therefore, paramagnetic Weiss temperatures and effective magnetic moments of the Gd atoms could not be determined with the satisfactory accuracy. Nevertheless, the estimated Weiss temperatures for the $Gd_5Si_{3.5}P_{0.5}$, $Gd_5Si_{3.25}P_{0.75}$ and $Gd_5Si_{2.75}P_{1.25}$ samples fall around 300 K, indicating a ferromagnetic nature of the interactions.

4.4.2 Magnetocaloric effect in $Gd_5Si_{2.75}P_{1.25}$

Magnetocaloric effect in terms of the isothermal entropy change, ΔS, can be evaluated from the magnetization data (Fig. 4.3) using the Maxwell equation:[13]

$$\left(\frac{\partial S(T,H)}{\partial H}\right)_T = \left(\frac{\partial M(T,H)}{\partial T}\right)_H . \tag{4.1}$$

The entropy change is obtained from the integration of the partial derivative of magnetization, M, with respect to temperature, T, over a change in the magnetic field, H:

$$\Delta S(T)_{\Delta H} = \int_{H_1}^{H_2} \left(\frac{\partial M(T,H)}{\partial T}\right)_{H,P} dH . \tag{4.2}$$

In practice a numerical integration is performed using the following formula:

$$\Delta S(T)_{\Delta H} = \sum_i \frac{M_i - M_{i+1}}{T_{i+1} - T_i} \delta H , \tag{4.3}$$

where δH is a magnetic field step and M_i and M_{i+1} are the values of magnetization at temperatures T_i and T_{i+1}, respectively. The magnetic entropy change, ΔS, for ΔH = 0–50 kOe peaks around the Curie temperature with a value of –7.8 J/kg K (Fig. 4.4) after the normalization for the phase concentration in the sample.

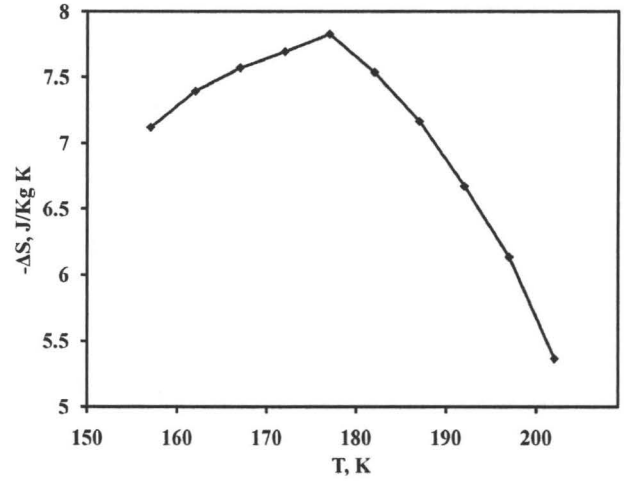

Figure 4.4. Magnetic entropy change for $Gd_5Si_{2.75}P_{1.25}$ as a function of temperature for ΔH = 0–50 kOe

This shape of the -ΔS vs. T graph is expected since magnetic moments are oriented

spontaneously at the Curie temperature, thus, the magnetization has a higher response to the external magnetic field at this region. A similar behavior was observed for other systems undergoing ferromagnetic transitions.[1,14,15] The value of -7.8 J/kg K for the magnetic entropy change indicates the presence of a conventional magnetocaloric effect (MCE) and implies the absence of a first-order coupled magneto-structural transition. Single crystal diffraction studies performed at 100 K on a Gd_5Si_3P single crystal, which contained about 80 mass% of the Sm_5Ge_4-type phase, showed no structural transition into the Gd_5Si_4-type structure, i.e. no reformation of the Si/P–Si/P dimers.

4.5 Conclusions

The $Gd_5Si_{3.5}P_{0.5}$ and $Gd_5Si_{3.25}P_{0.75}$ samples show two magnetic transitions, which correspond to the Gd_5Si_4- and Sm_5Ge_4-type phases. The $Gd_5Si_{2.75}P_{1.15}$ sample was also found to consist of both the Gd_5Si_4- and Sm_5Ge_4-type phases. According to the X-ray analysis, the $Gd_5Si_{2.75}P_{1.25}$ sample contained only the Sm_5Ge_4-type phase, thus $Gd_5Si_{2.75}P_{1.25}$ the composition can be considered as the right boundary within the Gd_5Si_4–Sm_5Ge_4 two-phase region. The Sm_5Ge_4-type $Gd_5Si_{2.75}P_{1.25}$ phase is a ferromagnet with a Curie temperature, T_c, of 184 K. The MCE in terms of the magnetic entropy change, ΔS, reaches the maximum of -7.8 J/kg K around the Curie temperature. Single-crystals X-ray diffraction studies show no signs of a temperature-dependant structural transition, which implies the presence of a conventional MCE only. The absence of a structural transition is reflected in the lower value of the magnetic entropy change, ΔS, as compared to the giant magnetocaloric $Gd_5Si_2Ge_2$ material.

References

[1] V. K. Pecharsky, K. A. Gschneidner Jr., *Phys. Rev. Lett.* **1997**, *78*, 4494–4497.

[2] A. O. Pecharsky, K. A. Gschneidner, V. K. Pecharsky, *J. Appl. Phys.* **2003**, 93, 4722–4728.

[3] W. Choe, V. K. Pecharsky, A. O. Pecharsky, K. A. Gschneidner Jr., V.G. Young Jr., G. J. Miller, *Phys. Rev. Lett.* **2000**, *84*, 4617–4620.

[4] V. K. Pecharsky, K. A. Gschneidner Jr., *Springer Ser. Mater. Sci.* **2005**, *79*, 199–222.

[5] Y. Mozharivskyj, W. Choe, A. O. Pecharsky, G. J. Miller, *J. Am. Chem. Soc.* **2003**, *125*, 15183–15190.

[6] L. -M. Wu, S. -H. Kim, D. -K. Seo, *J. Am. Chem. Soc.* **2005**, *127*, 15682–15683.

[7] V. Svitlyk, G. J. Miller, Y. Mozharivskyj, *J. Am. Chem. Soc.* **2009**, *131*, 2367–2374.

[8] J. Rodriguez-Carvajal, *IUCr Newsletter.* **2001**, *26*, 12–19.

[9] J. F. Miller et. al., *Tech. Rep.* AL-TDR-64-239 (AD 607082). **1964** 90.

[10] J. E. Barnes, K. P. Trumble, *J. Cryst. Growth* **1996**, *160*, 66–70.

[11] L. C. Pauling, *The Nature of the Chemical Bond and the Structure of Molecules and Crystals: An Introduction to Modern Structural Chemistry, third ed.* Cornell University Press, Ithaca, NY, **1960**.

[12] F. Holtzberg, R. J. Gambino, T. R. McGuire, *J. Phys. Chem. Solids* **1967**, *28*, 2283–2289.

[13] A. M. Tishin, Y. L. Spichkin, T*he Magnetocaloric Effect and Its Applications*, Institute of Physics Publishing, Bristol and Philadelphia, **2003**, p. 480.

[14] V. Svitlyk, F. Fei, Y. Mozharivskyj, *J. Solid State Chem.* **2008**, *181*, 1080–1086.

[15] S. Y. Dan'kov, A. M. Tishin, V. K. Pecharsky, K. A. Gschneidner Jr., *Phys. Rev. B: Condens. Matter Mater. Phys.* **1998**, *57*, 3478–3490.

Chapter 5. $Gd_5Si_{4-x}Bi_x$ structures: novel slab sequences achieved by turning off the directionality of nearest-slab interactions

This chapter contains the manuscript "$Gd_5Si_{4-x}Bi_x$ structures: novel slab sequences achieved by turning off the directionality of nearest-slab interactions", published in the Inorganic Chemistry (*Inorg. Chem.* **2009**, *48*, 10364–10370). The candidate completed all of the experimental synthesis, data collection, processing and interpretation and prepared the manuscript. Analysis of the stacking faults in the $Gd_5Si_{4-x}Bi_x$ system was performed in collaboration with Dr. B. J. Campbell.

$Gd_5Si_{4-x}Bi_x$ structures: novel slab sequences achieved by turning off the directionality of nearest-slab interactions

Volodymyr Svitlyk,[a] Branton J. Campbell,[b] and Yurij Mozharivskyj[a]

[a]*Department of Chemistry, McMaster University, Hamilton, ON, L8S 4M1, Canada*

[b]*Department of Physics and Astronomy, Brigham Young University, Provo, Utah 84602*

5.1 Abstract

Substitution of Bi for Si leads to the complete cleavage of the interslab dimers *T*-*T* in the $Gd_5Si_{4-x}Bi_x$ system with x = 1.58 - 2.42 (*T* is a mixture of Si and Bi). Equivalence of the interslab *T*···*T* contacts, achieved through combination of the electronic and geometrical parameters, removes directionality of nearest-slab interactions and allows for a novel slab stacking. Two new slab sequences, *ABCDABCD* (x = 2.07, $I4_1/acd$ space group) and *ABADABAD* (x = 2.42, $P4_2bc$), have been discovered in $Gd_5Si_{4-x}Bi_x$ in addition to the known one, ABAB, that is dominant among the RE_5X_4 phases (*RE* is a rare-earth element, *X* is a *p*-element). The slab stacking for x = 2.07 and x = 2.42 is dictated by the second-nearest slab interactions which promote an origin shift either for the entire slab sequence as in *ABCDABCD* or for every other second-nearest slab pair as in *ABADABAD*. The loss of the directionality of the nearest-slab bonding allows for extensive stacking faults and leads to diffuse scattering.

5.2 Introduction

RE_5T_4 phases (where *RE* is a rare earth and *T* is a p-element) such as the giant

magnetocaloric material $Gd_5Si_2Ge_2$ exhibit an intimate relationship between crystal structure, valence electron concentration, and physical properties.[1-9] Excluding the tetragonal Zr_5Si_4-type and hexagonal Ti_5Ga_4-type structures, most of the known RE_5T_4 structures can be described as stackings of rigid two-dimensional pseudotetragonal $_\infty^2[RE_5T_4]$ slabs (Figure 5.1). The principal differences among the distinct structures built from $_\infty^2[RE_5T_4]$ slabs lies in the strength of their interslab *T*-*T* dimers. In Gd_5Si_4-type structures (space group *Pnma*), the slabs are interconnected by strong *T*-*T* dimers ($d'_{T\text{-}T}$ < 2.7 Å). In contrast, the dimers are substantially stretched ($d'_{T\text{-}T}$ = ca. 2.9 Å) in Pu_5Rh_4 (*Pnma*) and entirely broken ($d'_{T\text{-}T}$ > 3.2 Å) in Sm_5Ge_4 (*Pnma*), Eu_5As_4 (*Cmca*), and $U_2Mo_3Si_4$ ($P2_1/c$). $Gd_5Si_2Ge_2$ ($P2_1/a$) is an interesting case in which the *T*-*T* dimers alternate between broken and unbroken from one interslab interface to the next.

The rigidity of these two-dimensional $_\infty^2[RE_5T_4]$ slabs and the relative flexibility of the interslab *T*-*T* dimers make the overall crystal structure quite sensitive to subtle variations in the electronic and geometric parameters available via *RE* and *T*-atom substitution. Extensive research has already demonstrated that the interslab *T*-*T* dimers, and thus the RE_5T_4 structures, can be manipulated by modifying either the valence electron count or the *T*-atom size.[5,9-11] In fact, the RE_5T_4 slab-stacking sequence proves to be an excellent probe of the strength of these dimers. In most cases, however, the original and modified structures are both described by the same two-slab *ABAB* stacking sequence (Figure 5.1), where the relative positions of the slabs are dictated by the lengths and orientations of the *T*-*T* dimers. Even when the dimers are cleaved ($d'_{T\text{-}T}$ > 3.2 Å), the original *ABAB* stacking sequence generally remains (e.g., the Gd_5Si_4-to-Sm_5Ge_4

transitions in the $Gd_5Si_{4-x}P_x$,[5] $Gd_5Ga_xGe_{4-x}$,[10] $Gd_5Si_{4-x}Ge_x$,[12] and $Dy_5Si_{4-x}Ge_x$[13] systems) suggesting that the residual interslab interactions are highly directional.

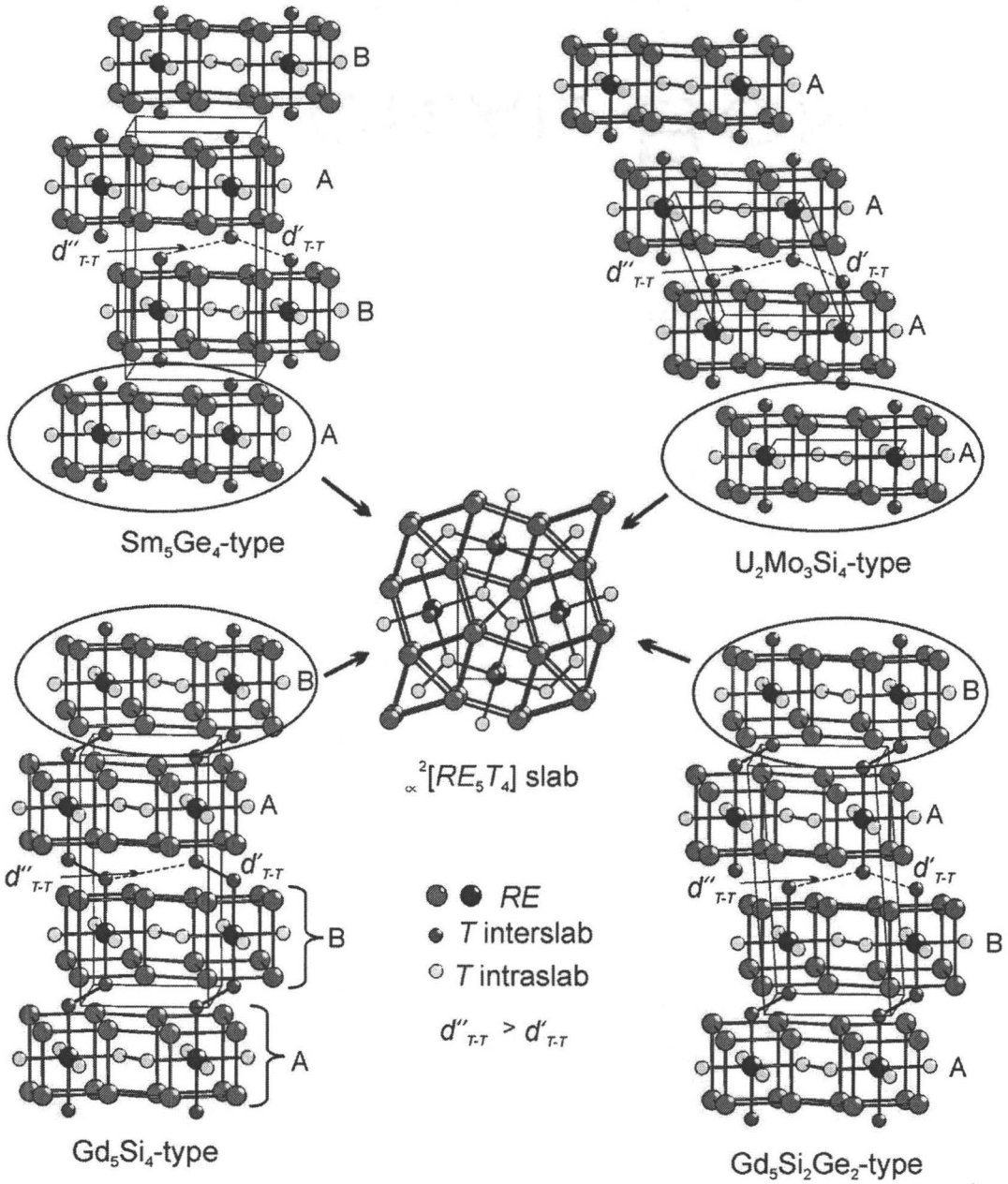

Figure 5.1. RE_5T_4 structure built from the $\infty^2[RE_5T_4]$ slabs. The Eu_5As_4 structure is similar to that of the Sm_5Ge_4 but has equal $d'_{T\text{-}T}$ and $d''_{T\text{-}T}$ distances. The Pu_5Rh_4-type structure is similar to the Gd_5Si_4-type one but with the stretched $d'_{T\text{-}T}$ dimers

In contrast to previous work, we now report that by simultaneously adjusting both valence-electron and geometric parameters within the $Gd_5Si_{4-x}Bi_x$ system, we can successfully suppress the directionality of the nearest-neighbor interslab interactions and thereby obtain entirely new slab stacking sequences that are controlled primarily by longer range (e.g., second-nearest-slab) interactions.

5.3 Experimental section

Starting materials for $Gd_5Si_{4-x}Bi_x$ samples were pieces of gadolinium (99.99 wt.%, distilled grade, Metall Rare Earth Limited, China), silicon (99.999 wt.%, Alfa Aesar), and bismuth (99.998 wt.%, Alfa Aesar). Samples with x = 0, 0.5, 1, 1.5, 2.0, 2.5, 3.0, and 3.5 and a total mass of 1 g were prepared by arc-melting. During the arc-melting process, Bi pieces were placed under the Si and Gd pieces in order to minimize Bi losses associated with the high vapor pressure of molten Bi. In addition, 2 mg of extra Bi were added to compensate for anticipated losses. The samples were remelted two times to improve homogeneity. The cast samples were then sealed in evacuated silica tubes, annealed at 800 °C for 2 weeks, and quenched in cold water.

Phase analyses of the polycrystalline products were performed on a PANalytical X'Pert Pro diffractometer with a linear X'Celerator detector. CoKα radiation was used to avoid the Gd fluorescence associated with CuKα radiation and to obtain the resolution required for the identification of structurally similar phases. Data from the samples with x = 0, 0.5, 1.5, 2, and 2.5 suggested phases closely related to the Gd_5Si_4-type structure. The samples with x = 3.0 and 3.5 yielded Gd_4Bi_3 and GdSi phases.The sample with x = 1

yielded a phase with a different structure and composition that is not discussed here.

Single crystals were extracted from both the cast and annealed samples with x = 0.5, 1.5, 2.0, and 2.5. Room-temperature data were collected on a STOE IPDS II diffractometer with Mo Kα radiation. Numerical absorption corrections were based on the crystal shapes that were originally derived from optical face indexing but later optimized against equivalent reflections using the STOE X-Shape software.[14] Structural refinements were performed using the SHELXL program.[15] Further details of the crystal structure investigations can be obtained from the Fachinformationszentrum Karlsruhe, 76344 Eggenstein-Leopoldshafen, Germany (fax: (49) 7247-808-666; e-mail: crysdata@fiz.karlsruhe.de), on quoting the depository CSD numbers 420923 for x = 0.5, 420922 for x = 1.5, 420921 for x = 2.0, and 420920 for x = 2.5, and also from the Supporting Information.

5.4 Results and discussion

5.4.1 Structural analysis

All crystals except for x = 0.5 showed significant diffuse scattering (Figures 5.2 and 5.3) due to stacking-fault defects in the $\propto^2[Gd_5T_4]$ slab-stacking sequence (recall that T is the mixture of Si and Bi). This diffuse scattering was most intense at x = 2.5. In each case, the observed diffuse scattering obeyed an $h + k = 2n + 1$ selection rule (equivalent to $k + l = 2n + 1$ in the setting used for x = 1.5), in addition to a rather unusual $h \neq 3n$ and $k \neq 3n$ selection rule (equivalent to $k \neq 3n$ and $l \neq 3n$ in the setting selected for x = 1.5). The origin of these selection rules is discussed in more detail below.

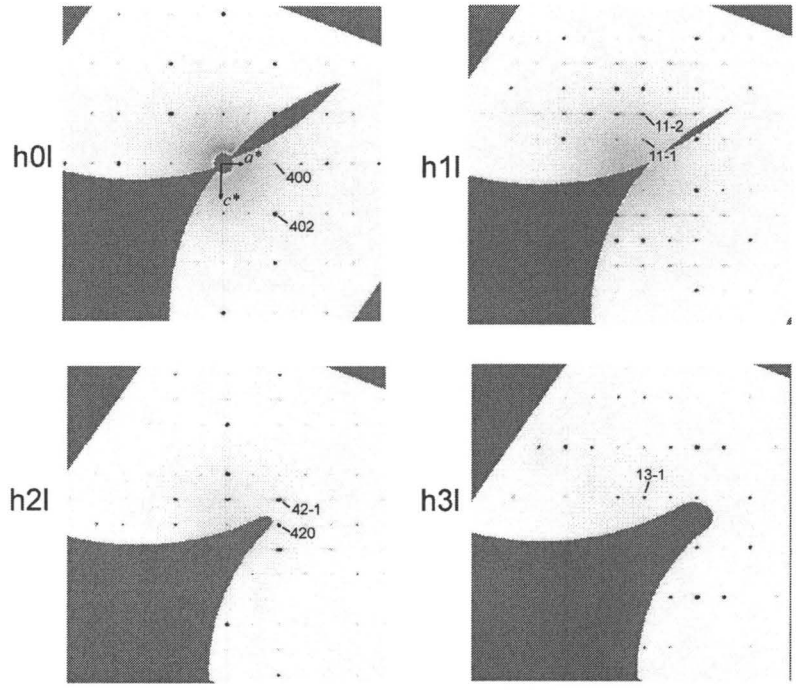

Figure 5.2. Reciprocal layers for the $Gd_5Si_{2.5}Bi_{1.5}$ crystal

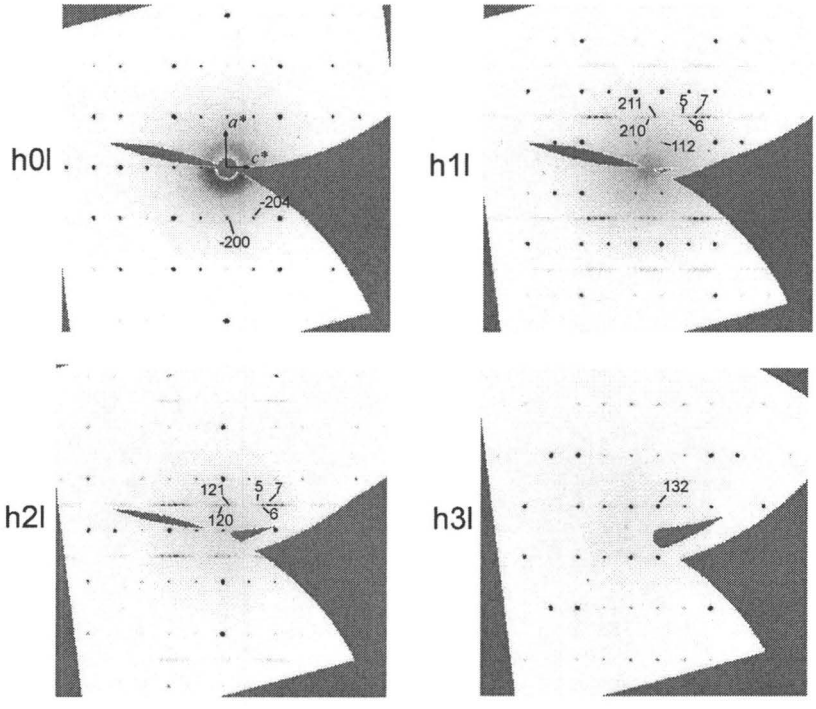

Figure 5.3. Reciprocal layers for the $Gd_5Si_{1.5}Bi_{2.5}$ crystal

Space-group determinations and structure solutions were straightforward for the crystals with x = 0.5, 1.5, and 2.0. Crystallographic data and atomic parameters are summarized in Tables 5.1 and 5.2 and illustrated in Figure 5.5. Because the diffraction data from the annealed and unannealed crystals were very similar, only the results from the annealed crystals are presented here. Indexing of the Bragg's reflections for the crystal with x = 0.5 yielded an orthorhombic *Pnma* symmetry and an *ABAB* slab-stacking sequence similar to that of Gd_5Si_4. The refined composition $Gd_5Si_{3.904(8)}Bi_{0.096(8)}$ of the Gd_5Si_4-type phase from the sample with x = 0.5 suggests that the homogeneity region for the Gd_5Si_4-type phase is unlikely to extend beyond x = 0.096(8). For the crystal with x = 1.5, one of the indexing choices was a *C*-centered unit cell with the b and c parameters being equal within 2 standard deviations (Table 5.1). The orthorhombic symmetry was verified through the powder diffraction which clearly indicated peak splitting and yielded a larger difference between the b and c parameters (a = 15.262(1), b = 7.9144(8), c = 7.9333(8) Å). The resulting structure had the *Cmca* symmetry, an *ABAB* slab-stacking sequence, and was isostructural to Eu_5As_4. But unlike Gd_5Si_4, the cleaved dimers allowed the "*B*" slab to shift all the way to the symmetric (x = 1/2, y = 0) position relative to the "*A*" slab. The crystal with x = 2.0 was unambiguously indexed in a larger *I*-centered tetragonal cell (a = 7.9858(9), c = 30.700(6) Å) and had systematic absences consistent with space-group symmetry $I4_1/acd$. The c-axis cell-doubling relative to the x =1.5 structure is due to a novel spiral slab-stacking sequence of the *ABCDABCD* type, which involves four different symmetric in-plane slab positions: *A*(0, 0), *B*(1/2, 0), *C*(1/2, 1/2), and *D*(0, 1/2).

Table 5.1. Crystal data and structure refinements for $Gd_5Si_{4-x}Bi_x$ at 293 K, Mo$K\alpha_1$ radiation, STOE IPDS II diffractometer

sample	$Gd_5Si_{3.5}Bi_{0.5}$	$Gd_5Si_{2.5}Bi_{1.5}$	$Gd_5Si_2Bi_2$	$Gd_5Si_{1.5}Bi_{2.5}$
composition	$Gd_5Si_{3.904(8)}Bi_{0.096(8)}$	$Gd_5Si_{2.416(8)}Bi_{1.584(8)}$	$Gd_5Si_{1.93(2)}Bi_{2.07(2)}$	$Gd_5Si_{1.58(1)}Bi_{2.42(1)}$
space group	*Pnma*	*Cmca*	$I4_1/acd$	$P4_2bc$
lattice parameters, Å	a = 7.4850(8) b = 14.776(1) c = 7.7700(7)	a = 15.246(4) b = 7.901(2) c = 7.898(2)	a = 7.9858(9) c = 30.700(6)	a = 8.0296(7) c = 30.883(4)
volume, Å^3	859.3(1)	951.3(4)	1957.8(5)	1991.2(4)
Z	4	4	8	8
density (calc), g/cm^3	7.082	8.276	8.649	8.860
θ range	2.96 to 29.19°	2.67 to 29.15°	2.65 to 29.16°	1.32 to 25.12°
index ranges	$-10 \le h \le 10$, $-20 \le k \le 17$, $-9 \le l \le 10$	$-20 \le h \le 19$, $-10 \le k \le 9$, $-10 \le l \le 10$	$-9 \le h \le 10$, $-10 \le k \le 10$, $-41 \le l \le 42$	$-9 \le h \le 9$, $-9 \le k \le 8$, $-36 \le l \le 36$
reflections collected	7954	3268	7461	9675
independent reflections	1195 [R_{int} = 0.1191]	660 [R_{int} = 0.1424]	646 [R_{int} = 0.1289]	1778 [R_{int} = 0.1776]
completeness to max 2θ	98.9 %	99.0 %	96.6 %	99.5 %
data / restraints / par.	1195/0/48	660/0/28	646/0/26	1778/1/88
goodness-of-fit on F^2	0.952	0.855	0.997	0.735
final R indices [$I>2\sigma(I)$]	R_1 = 0.0474, wR_2 =0.0557	R_1 = 0.0456, wR_2 =0.0437	R_1 = 0.0452, wR_2 = 0.0394	R_1 = 0.0531, wR_2 = 0.1224
R indices (all data)	R_1 = 0.0928, wR_2 = 0.0626	R_1 = 0.1338, wR_2 = 0.0553	R_1 = 0.1361, wR_2 = 0.0508	R_1 = 0.1936, wR_2 = 0.1666
absolute structure factor	n/a	n/a	n/a	0.0(2)
extinction coefficient	0.00046(7)	0.000059(15)	0.000037(6)	0.000048(12)
largest peak/ hole, e/Å^3	2.217/-3.448	2.289/-2.579	2.564/-1.948	2.622/-2.878
minority fraction	0	0.059(2)	0.025(2)	0.084(2)

Table 5.2. Atomic and isotropic temperature (U) parameters for $Gd_5Si_{4-x}Bi_x$ from single crystal diffraction data

atom	site	occupancy	x/a	y/b	z/c	U (Å^2)
			$Gd_5Si_{3.904(8)}Bi_{0.096(8)}$			
Gd(1)	8*d*	1	0.02582(9)	0.59735(4)	0.1826(1)	0.0121(2)
Gd(2)	8*d*	1	0.3190(1)	0.12269(4)	0.1793(1)	0.0105(2)
Gd(3)	4*c*	1	0.1479(1)	1/4	0.5110(1)	0.0100(2)
Si/Bi(1)	8*d*	0.952/0.048(4)	0.1551(6)	0.0389(2)	0.4698(4)	0.019(1)
Si(2)	4*c*	1	0.0249(8)	1/4	0.1007(7)	0.011(1)
Si(3)	4*c*	1	0.2656(8)	1/4	0.8717(7)	0.007(1)
			$Gd_5Si_{2.416(8)}Bi_{1.584(8)}$			
Gd(1)	16*g*	1	0.12840(6)	0.8295(1)	0.83011(1)	0.0177(2)
Gd(2)	4*b*	1	1/2	0	0	0.0120(4)
Bi/Si(1)	8*d*	0.792/0.206(4)	0.29187(8)	0	0	0.0125(4)
Si(2)	8*f*	1	0	0.8779(11)	0.1255(7)	0.014(2)
			$Gd_5Si_{1.93(1)}Bi_{2.07(1)}$			
Gd(1)	32*g*	1	0.3331(2)	0.9178(2)	0.06149(2)	0.0163(2)
Gd(2)	8*a*	1	0	1/4	3/8	0.0116(2)
Bi/Si(1)	16*d*	0.938/0.062(6)	0	1/4	0.97841(2)	0.0135(3)
Si/Bi(2)	16*f*	0.902/0.098(5)	0.3658(3)	x+1/4	1/8	0.011(1)
			$Gd_5Si_{1.58(1)}Bi_{2.42(1)}$[a]			
Gd(1A)	8*c*	1	0.6754(8)	0.1615(8)	0.06388(8)	0.043(2)
Gd(2A)	8*c*	1	0.6692(8)	0.1583(7)	0.93612(7)	0.046(2)
Gd(3A)	4*a*	1	0	0	09987(3)	0.034(2)
Gd(1B)	8*c*	1	0.1693(7)	0.1699(7)	0.3137(2)	0.026(1)
Gd(2B)	8*c*	1	0.1604(7)	0.1652(6)	0.1864(1)	0.026(1)
Gd(3B)	4*a*	1	0	1/2	0.2478(3)	0.024(1)
Bi(1)	4*a*	1	0	0	0.1033(2)	0.033(2)
Bi(2)	4*a*	1	0	0	0.8965(2)	0.035(2)
Bi(3)	4*b*	1	0	1/2	0.3511(2)	0.039(2)
Bi(4)	4*b*	1	0	1/2	0.1459(2)	0.024(1)
Si/Bi(5A)	8*c*	0.789/0.211(5)	0.6409(17)	0.8666(17)	0.9974(6)	0.037(3)
Si/Bi(5B)	8*c*	0.789/0.211(5)	0.1422(12)	0.8647(11)	0.2470(5)	0.025(2)

[a] For $Gd_5Si_{1.58(1)}Bi_{2.42(1)}$, the A and B labels in the atomic names designate the *A* and *B* slabs to which the atoms belong

Stacking faults present in $Gd_5Si_{4-x}Bi_x$ structures interrupt the $\propto^2[RE_5T_4]$ slab-stacking sequence, effectively replacing every *A* slab with a *C* slab and every *B* slab with a *D* slab (and vice versa) on one side of the fault plane. In structural refinements, this faulting is manifested as a small residual electron density within the slabs at positions that are shifted in-plane by (1/2, 1/2) relative to normal heavy atom positions. This density is most noticeable at fault-shifted Gd positions within the 3^2434 nets. In the $x = 2.5$ sample, however, which had the highest concentration of stacking faults, the more weakly scattering Si-rich *T* site inside the trigonal prism also produced some fault-shifted residual electron density. The extra fault-shifted electron density was treated as a split site during the refinement, such that the occupancies of all fault-shifted atoms were constrained to be the same. The resulting occupancy is referred to as the "minority fraction" in Table 5.1 and is explained in the detailed description of the refinement contained in the Supporting Information. The atomic parameters of the unshifted structure are shown in Table 5.2, while the constraints that tie the fault-shifted and unshifted atoms together are also described in the Chapter 8.

5.4.2 The $x = 2.5$ structure

The $x = 2.5$ case was comparatively complicated and will be discussed separately below. While the conventional cell shape ($a = 8.0296(7)$, $c = 30.883(4)$ Å) of the $x = 2.5$ crystal was essentially the same as that of the $x = 2.0$ crystal, there were many moderately weak reflections that violated the *I*-centering selection rule ($h + k + l = 2n$), but which were consistent with a primitive lattice (Figure 5.3). Oddly, these weaker *I*-center-

violating reflections only appear within the diffuse streaks with $h + k = 2n + 1$ lines and never at the $h + k = 2n$ positions. Such a pattern is not consistent with any standard set of systematic absences. Careful examination revealed that all of the peaks along the $h + k = 2n + 1$ lines (whether or not they violate the I centering) are somewhat diffuse along the c^* direction and that their diffuse tails actually give rise to the observed diffuse streaks.

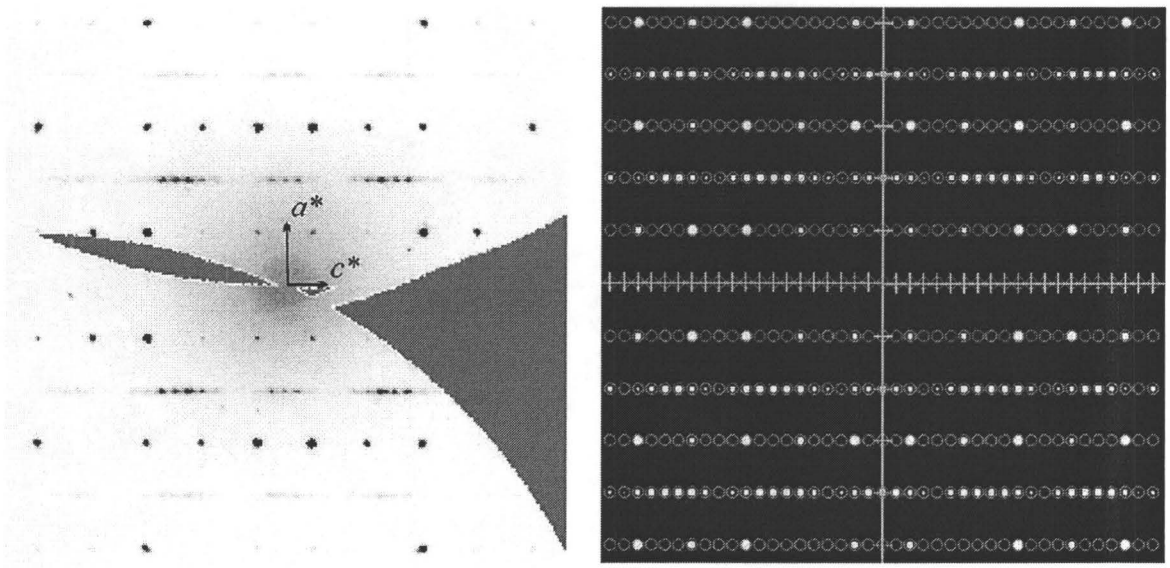

Figure 5.4. Comparison between the experimental (left) and simulated reciprocal (right) $h1l$ layers for the $Gd_5Si_{1.5}Bi_{2.5}$ crystal. The *ABAD* slab sequence ($P4_2bc$ space group) was used for the simulation

By neglecting the "primitive" reflections along the $h + k = 2n + 1$ lines, the structure was solved in space group $I4_1/acd$, which produced a structure similar to that of $x = 2.0$, except that significant residual density was found around the Gd and Si/Bi sites. While the $I4_1/acd$ solution demonstrated that the structure is built from the $\propto^2[Gd_5T_4]$ slabs, the presence of additional "primitive" reflections suggested a different slab-

stacking sequence. Various slab-stacking models based on $\propto^2[Gd_5T_4]$ slabs were constructed, and their diffraction patterns were simulated using the ISODISPLACE software[16] and compared against the experimental diffraction data from the $x = 2.5$ crystal. The *ABADABAD* slab stacking, which has the $P4_2bc$ symmetry, yielded an excellent match between the simulated and experimental patterns (Figure 5.4) and was subsequently subjected to a successful structural refinement.

5.4.3 Structure of and interactions between the $\propto^2[RE_5T_4]$ slabs

At this point, we will briefly discuss the structure of the $\propto^2[RE_5T_4]$ slabs and the interslab *T-T* interactions directing their stacking. The Gd_5Si_4, Pu_5Rh_4, Sm_5Ge_4 (*Pnma*), $Gd_5Si_2Ge_2$ ($P2_1/a$), and $U_2Mo_3Si_4$-type ($P2_1/c$) structures of RE_5T_4 (see Figure 5.1) are built from nearly identical pseudotetragonal 3^2434 nets of *RE* atoms. Two such nets are stacked over one another to form $\propto^2[RE_5T_4]$ slabs with *RE* atoms located in pseudocubes and half of the *T* atoms in trigonal prismatic voids. Since the trigonal prisms in these slabs share a face, the separation between the *T* atoms is small enough to allow the formation of the intraslab dimers. The *RE* pseudocubes are capped top and bottom by exterior *T* atoms, which we refer to as the interslab *T* atoms. In all RE_5T_4 structures, the symmetry of the $\propto^2[RE_5T_4]$ slabs is either tetragonal or pseudotetragonal.

As mentioned in the Introduction, the difference between different RE_5T_4 structures lies in how the $\propto^2[RE_5T_4]$ slabs are interconnected through the interslab *T-T* dimers. If the dimers are short ($d'_{T\text{-}T} < 2.7$ Å), Gd_5Si_4-type structures form. If the dimers

are stretched ($d'_{T\text{-}T}$ = ca. 2.9 Å) or broken ($d'_{T\text{-}T}$ > 3.2 Å), Pu_5Rh_4, Sm_5Ge_4, or $U_2Mo_3Si_4$-type structures result. And if only half of the dimers are broken, $Gd_5Si_2Ge_2$-type structures appear (Figure 5.1). Changes in the dimer length are accompanied by movement of the $\propto^2[RE_5T_4]$ slab primarily along the direction of the dimer stretching/cleavage. Regardless of whether or not the dimers are broken, the *T*···*T* interslab contacts are not uniform along the dimer direction, i.e. there are two distinct sets of *T*···*T* distances ($d'_{T\text{-}T}$ and $d''_{T\text{-}T}$ in Figure 5.1). For example, $Gd_5Si_{2.75}P_{1.25}$ which has the largest reported *T*···*T* distances, still has short and long interslab *TT* contacts ($d'_{T\text{-}T}$ = 3.74 Å vs $d''_{T\text{-}T}$ = 4.38 Å).[10] Depending on the arrangement of the *T*···*T* contacts between the slabs, two slab-stacking sequences can be formed: the *ABAB* sequence with its herringbone pattern of shorter *T*···*T* contacts and the *AAAA* sequence with its ascending pattern of shorter *T*···*T* contacts (Figure 5.1). In both cases, it is the presence of shorter and longer *T*···*T* contacts that provides directionality to the slab stacking. The question can be asked, "What will happen to the slab-stacking sequence in general if the interslab *T*···*T* contacts become uniform?". The $Gd_5Si_{4-x}Bi_x$ system provides some answers to this question.

5.4.4 Interslab dimer cleavage

There are three structural transitions in the $Gd_5Si_{4-x}Bi_x$ system as a function of the Bi concentration (Figure 5.5): the *Pnma* → *Cmca* transition for x = 0.10-1.58, *Cmca* → $I4_1/acd$ for x = 1.58-2.07, and $I4_1/acd$ → $P4_2bc$ for x = 2.07-2.42 (x is the refined Bi amount). The *Pnma* → *Cmca* transition in the $Gd_5Si_{4-x}Bi_x$ system (x = 0.10-1.58) features

complete cleavage of the interslab *T*-*T* dimers ($d'_{T\text{-}T}$ = 2.63 → 4.15 Å) so that the *T*···*T* contacts all become identical. This dimer cleavage is the consequence of electronic and size effects associated with Bi substitution and mirrors the transitions observed in $Gd_5Si_{4-x}P_x$ and $Gd_5Si_{4-x}Sn_x$.[10,11] In $Gd_5Si_{4-x}P_x$, an increase in the valence electron count achieved through P substitution was used to break the interslab dimers in $Gd_5Si_{2.75}P_{1.25}$ ($d'_{T\text{-}T}$ = 2.49 → 3.74 Å).[10] In the $Gd_5Si_{4-x}Sn_x$ system, the larger size of the Sn atoms was employed to stretch the dimers ($d'_{T\text{-}T}$ = 2.49 → 3.04 Å).[11] Similar to $Gd_5Si_{2.75}P_{1.25}$, the electronic contribution to the dimer cleavage in $Gd_5Si_{2.42}Bi_{1.58}$ is related to the population of the antibonding states within the *T*-*T* dimers. Also, the larger size of Bi atoms promotes dimer cleavage. The two effects can be already seen in $Gd_5Si_{3.90}Bi_{0.10}$ which shows considerable dimer stretching compared to Gd_5Si_4 ($d'_{T\text{-}T}$ = 2.49 → 2.63 Å).

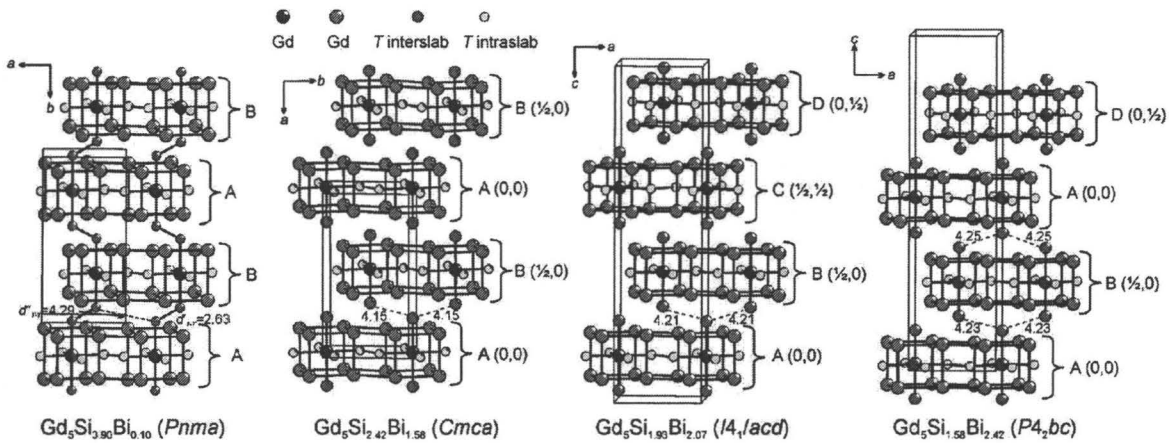

Figure 5.5. Structures of and slab stacking in the $Gd_5Si_{4-x}Bi_x$ phases

In $Gd_5Si_{2.42}Bi_{1.58}$, both the electronic and size effects act in parallel and lead to the full cleavage of the interslab dimers. The resulting uniformity of the *T*···*T* contacts creates an additional translational symmetry element of 1/2***a*** + 1/2***b***, which leads to the *Cmca*

space group symmetry. The full dimer cleavage also allows the slabs to relax into a pseudotetragonal state that is very near to their ideal tetragonal state, so the that *b* and *c* cell parameters become highly similar. In fact, it is only the influence of the nontetragonal stacking arrangement that prevents the slabs from becoming perfectly tetragonal. Because the ideal $\propto^2[Gd_5T_4]$ slab has tetragonal point symmetry, it seems natural that slab-stacking sequences that are compatible with tetragonal symmetry should exist. Yet in $Gd_5Si_{2.42}Bi_{1.58}$, we continue to see a preference for the *ABAB* stacking sequence associated with unbroken dimers.

5.4.5 Stacking rules and interslab correlations

A further increase in the Bi concentration finally yields two new and fully tetragonal slab-stacking sequences (and symmetries): *ABCDABCD* ($I4_1/acd$) for $Gd_5Si_{1.93}Bi_{2.07}$ and *ABADABAD* ($P4_2bc$) for $Gd_5Si_{1.58}Bi_{2.42}$. Consider the four in-plane slab origins permitted by uniform $T\cdots T$ contact distances: *A*(0, 0), *B*(1/2, 0), *C*(1/2, 1/2), and *D*(0, 1/2). If we label all of the slabs in the crystal with sequential integers, assuming that the zeroth slab is of the *A* type, any stacking sequence built from these four slab origins will have the following properties: (1) even-integer slabs will either be of the *A* or *C* type and (2) odd-integer slabs will either be of the *B* or *D* type. Thus, *AC*, *CA*, *BD*, and *DB* nearest-neighbor (1*NN*) pairs are never permitted.

Both the *ABCDABCD* and *ABADABAD* sequences involve four-slab stacking sequences, hence a $c \sim 30$ Å cell parameter. Unlike the *ABAB* sequence of $Gd_5Si_{2.42}Bi_{1.58}$, neither four-slab stacking sequence possesses an absolute preference for the direction of

nearest-neighbor slab correlations - the neighbor of an *A* slab is equally likely to be of the *B* or *D* varieties, and the neighbor of a *B* slab is equally likely to be of the *A* or *C* varieties. Yet both sequences show a perfect correlation among fourth-nearest- neighbor slabs (4*NN* slabs) which must be of the same type. The difference rests in the nature of their second-nearest-neighbor (2*NN*) interslab correlations. For *ABCDABCD*, all 2*NN* pairs are perfectly anticorrelated (i.e., *A* pairs with *C* and *B* pairs with *D*). In contrast, for *ABADABAD*, half the 2*NN* pairs are correlated (i.e., two slabs of the same type) and half are anticorrelated.

5.4.6 Systematic absences

The primary $h + k = 2n + 1$ selection rule for the diffuse streaks arises from a fault vector of (1/2, 1/2, 0), which corresponds to randomly replacing an *A*(0,0) slab with a *C*(1/2, 1/2) slab or a *B*(1/2, 0) slab with a *D*(0, 1/2) slab. The stacking disorder effectively steals intensity from the Bragg peaks along these lines and redistributes it into their diffuse tails along the ***c**** direction.

From Figures 5.2 and 5.3, we observe that the density of Bragg reflections along the $h + k = 2n + 1$ lines is four times higher than the corresponding density along the $h + k = 2n$ lines for the $x = 2.5$ crystal. A similar observation applies to the $x = 2.0$ crystal, where the Bragg peak density is two times higher along the $h + k = 2n + 1$ lines than along the $h + k = 2n$ lines. This is a strong evidence for the rigidity of the $\propto^2[Gd_5T_4]$ slabs. If the slabs were to substantially relax via all of the structural degrees of freedom provided by $P4_2bc$ (or $I4_1/acd$) symmetry, then additional peaks would also appear along

the $h + k = 2n$ lines consistent with the symmetry. But rigidity rather than symmetry prevents them from doing so. Thus, the unusual pattern of absences within the $h + k = 2n$ lines is due to the fact that all four slabs remain approximately identical even though they are permitted by symmetry to differ.

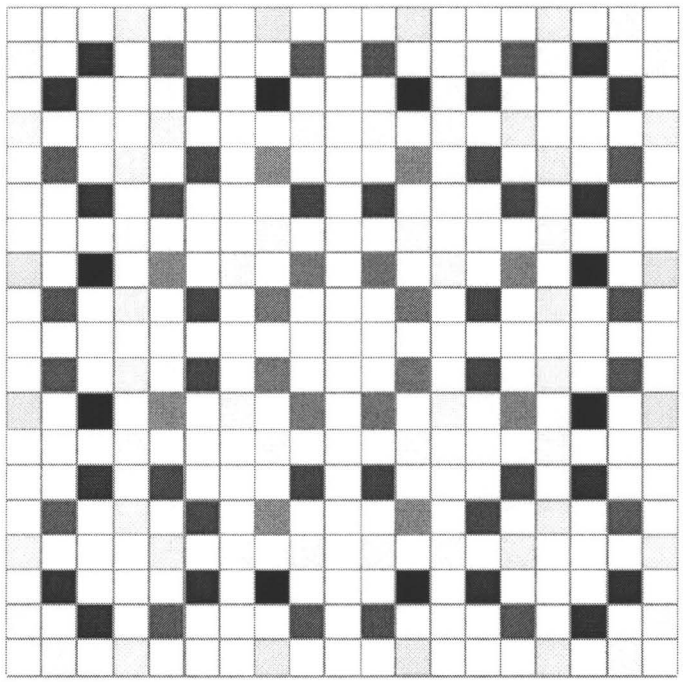

Figure 5.6. Distribution of $|F_{slab}|^2$ intensities for the $h + k = 2n + 1$ positions within the $l = 0$ plane of $Gd_5Si_{1.93}Bi_{2.07}$ for $-9 \leq h,k \leq 9$. The square at the center corresponds to $h = 0$ and $k = 0$. Darker squares indicate higher intensities. The $h + k = 2n$ squares are left empty - their intensities are not represented here

The unusual $h \neq 3n$ and $k \neq 3n$ diffuse-scattering selection rule observed in all of the $Gd_5Si_{4-x}Bi_x$ samples is more subtle but also less interesting. It originates in the X-ray structure factor of a single $\propto^2[Gd_5T_4]$ slab, which can be factored out to the front of the

overall diffuse scattering structure factor. Or more specifically, it originates in the positions of the Gd atoms within the slab. As an example, consider a single tetragonal $_{\infty}^{2}[RE_5T_4]$ slab, where the average a-axis separation between Gd atoms within the 3^2434 nets is approximately $\Delta x_{Gd} = 1/6$. It turns out that if we set $\Delta x_{Gd} = 1/6$ exactly, and neglect all non-Gd atoms, we compute $|F_{slab}|^2 = 0$ for any $h + k = 2n + 1$ position in which $h = 3n$ or $k = 3n$, and $|F_{slab}|^2 \approx (6N_{Gd})^2$ for each of the other $h + k = 2n + 1$ positions, where N_{Gd} is the atomic number of Gd. In Figure 5.6, which illustrates the distribution of $|F_{slab}|^2$ intensities for a single slab of $Gd_5Si_{1.93}Bi_{2.07}$, we see that the selection rule is only approximate since there are other atoms contributing to the structure factor.

In Figure 5.3, observe that the intensity of the diffuse streaks from the $x = 2.5$ crystal and also the intensities of the Bragg peaks along the same $h + k = 2n + 1$ lines are modulated along the c^* direction with a period roughly equal to 4 r.l.u. (relative to a short cell parameter corresponding to a two-slab stacking sequence). More generally, the diffuse scattering in all of the $Gd_5Si_{4-x}Bi_x$ samples was modulated along c^* (a^* for $x = 1.5$) with roughly the same period. This rather striking feature also has its origin in $|F_{slab}|^2$, which contains a multiplicative factor of $\cos^2(2\pi/\Delta z_{Gd})$, where Δz_{Gd} is the c-axis separation between the Gd2 atoms inside the tetragonal voids and the Gd1 atoms within the 3^2434 nets. Measured in r.l.u. relative to a two-slab cell parameter, this separation is approximately $\Delta z_{Gd} = 0.127$, which yields a period of $\Delta l = (2z_{Gd1})^{-1} = 3.94 \approx 4$ r.l.u., as observed.

5.5 Conclusions

The $Gd_5Si_{4-x}Bi_x$ system highlights the role of next-nearest-slab interactions in the structural assembly in the RE_5T_4 phases. Interslab *T-T* dimers or residual bonding left from these dimers (i.e., the $T\cdots T$ contacts are not equivalent) serves as a directional force for the $\propto^2[RE_5T_4]$ slab packing and leads to the *ABAB* and *AAAA* stacking sequences. The complete cleavage of the *T-T* dimers in $Gd_5Si_{4-x}Bi_x$ switches off this directionality and produces novel slab sequences. In cases when $T\cdots T$ interactions provide no directionality, the second-nearest-slab interactions become important. In particular when these interactions are strong and promote an origin shift, a four-slab *ABCDABCD* sequence results. If the second-nearest-neighbor interactions favor the same origin, the *ABAB* order persists, and the presence of the two types of interactions promotes the formation of *ABADABAD* stacking. Strong second-nearest-slab interactions promote long-range stacking order, while weaker interactions or competing interactions lead to stacking disorder and diffuse scattering. Currently, the physical nature of the second-nearest-slab interactions that produced the observed interslab correlations in $Gd_5Si_{4-x}Bi_x$ is being investigated.

5.6 Acknowledgment

This work was supported by a Discovery Grant from the Natural Sciences and Engineering Research Council of Canada and by an award from Research Corporation.

Supporting Information Available: Discussion of the relationship between the residual

electron and fault densities, refinement procedures and results for $Gd_5Si_{4-x}Bi_x$ with x = 1.58, 2.07, and 2.42, and X-ray crystallographic files for x = 1.58, 2.07, and 2.42 (CIF). This material is available free of charge via the Internet at http://pubs.acs.org.

References

[1] V. K. Pecharsky, K. A. Gschneidner Jr., *Phys. Rev. Lett.* **1997**, *78*, 4494–4497.

[2] V. K. Pecharsky, K. A. Gschneidner Jr., *J. Alloys Compd.* **1997**, *260*, 98–106.

[3] W. Choe, V. K. Pecharsky, A. O. Pecharsky, K. A. Gschneidner Jr., V. G. Young Jr., G. J. Miller, *Phys. Rev. Lett.* **2000**, *84*, 4617–4620.

[4] W. Choe, G. J. Miller, J. Meyers, S. Chumbley, A. O. Pecharsky, *Chem. Mater.* **2003**, *15*, 1413–1419.

[5] Y. Mozharivskyj, W. Choe, A. O. Pecharsky, G. J. Miller, *J. Am. Chem. Soc.* **2003**, *125*, 15183–15190.

[6] V. K. Pecharsky, A. O. Pecharsky, Y. Mozharivskyj, K. A. Gschneidner, G. J. Miller, *Phys. Rev. Lett.* **2003**, *91*, 207205/01-04.

[7] Y. Mozharivskyj, A. O. Pecharsky, V. K. Pecharsky, G. J. Miller, *J. Am. Chem. Soc.* **2005**, *127*, 317–324.

[8] L.-M. Wu, S.-H. Kim, D.-K. Seo, *J. Am. Chem. Soc.* **2005**, *127*, 15682–15683.

[9] S. Misra, G. J. Miller, *J. Am. Chem. Soc.* **2008**, *130*, 13900–13911.

[10] V. Svitlyk, G. J. Miller, Y. Mozharivskyj, *J. Am. Chem. Soc.* **2009**, *131*, 2367–2374.

[11] Y. Mozharivskyj, A. O. Tsokol, G. J. Miller, *Z. Kristallogr.* **2006**, *221*, 493–501.

[12] V. K. Pecharsky, K. A. Gschneidner Jr., *J. Alloys Compd.* **1997**, *260*, 98–106.

[13] K. A. Gschneidner Jr., V. K. Pecharsky, A. O. Pecharsky, V. V. Ivtchenko, E. M. Levin, *J. Alloys Compd.* **2000**, *303-304*, 214–222.

[14] *STOE*; Cie *X-SHAPE* Version 2.05 and *X-RED32* Version 1.10; *STOE & Cie GmbH*: Darmstadt, Germany, **2004**.

[15] G. M. Sheldrick, *SHELXL97 and SHELXS97*, University of Gottingen: Germany, **1997**.

[16] B. J. Campbell, H. T. Stokes, D. E. Tanner, D. M. Hatch, *J. Appl. Crystallogr.* **2006**, *39*, 607–614.

Chapter 6. Structural, magnetic and magnetocaloric properties of the $Gd_5Si_{4-x}Sb_x$ (x = 0.5-3.5) phases

This chapter contains the manuscript "Structural, magnetic and magnetocaloric properties of the $Gd_5Si_{4-x}Sb_x$ (x = 0.5-3.5) phases", published in the Journal of Magnetism and Magnetic Materials (*J. Magn. Magn. Mater.* **2010**, *322*, 2558–2566). The candidate completed the experimental synthesis, data collection, processing and interpretation and prepared the manuscript. An undergraduate summer student, Y. Y. J. Cheung, was involved in the experimental synthesis, data collection, processing and interpretation.

Structural, magnetic and magnetocaloric properties of the

$Gd_5Si_{4-x}Sb_x$ (x = 0.5-3.5) phases

Volodymyr Svitlyk, Yan Yin Janice Cheung and Yurij Mozharivskyj

Department of Chemistry, McMaster University, Hamilton, ON, L8S 4M1, Canada

6.1 Abstract

Substitution of Sb for Si in the Gd_5Si_4 phase results in the formation of ternary $Gd_5Si_{4-x}Sb_x$ phases with three different structure types. For $x \leq 0.38$ the Gd_5Si_4-type structure (*Pnma* space group) with all interslab *T*-*T* dimers intact exists (*T* is Si or Si/Sb mixture), in the x = 1.21-1.79 region the Sm_5Ge_4-type structure (*Pnma*) with all interslab dimers broken is found. A further increase in the Sb concentration (x = 2.27 - 3.1) leads to the appearance of the Eu_5As_4-type structure (*Cmca*) with broken but equivalent interslab *T*···*T* bonds. The $Gd_5Si_{4-x}Sb_x$ phases with $1.21 \leq x \leq 3.1$ undergo ferromagnetic transitions in the temperature range from 164 to 295 K. Magnetocaloric effect in terms of the isothermal entropy change, ΔS, reaches the maximum values of -3.7(4), -4.2(6) and -4.6(7) J/kg K for the $Gd_5Si_2Sb_2$, $Gd_5Si_{1.5}Sb_{2.5}$ and Gd_5SiSb_3 samples, respectively.

6.2 Introduction

Magnetocaloric materials became a subject of great scientific and industrial interest[1] as they can be utilized for magnetic refrigeration, which offers a potentially higher cooling efficiency than the conventional vapor-pressure technique. For instance, a Gd-based refrigerator is about 1.5 times more efficient than its classical counterpart.[2]

Cooling performance of magnetocaloric materials depends on the entropy change, ΔS, induced by a varying external magnetic field. In the Gd metal, this entropy change stems from a second-order ferromagnetic alignment of magnetic moments and, thus, is referred to as a magnetic entropy change, ΔS_{mag}. The entropy change can be enhanced significantly if a magnetic transition is coupled to a first-order structural transition. In this case the total entropy change has an additional, structural contribution: $\Delta S = \Delta S_{mag} + \Delta S_{str}$.[3] Such effect is called a giant magnetocaloric effect and was discovered originally in $Gd_5Si_2Ge_2$[4] and later in other RE_5T_4 phases (RE – rare-earth element, T – p-element).[5-8] Similar effects were also observed in the $MnFeP_{1-x}As_x$,[9] $LaFe_{13-x}Si_x$[10] and other materials.[11-13]

The RE_5T_4 phases, with $Gd_5Si_2Ge_2$ being one of their representatives, are very attractive both from the chemists' and physicists' perspectives. They display an intimate relation between a crystal structure, physical properties, valence electron count (VEC) and size effect[14-16] and thus afford a rational modification of their physico-chemical properties. The structure-VEC relationship was successfully utilized to control formation/breaking of the interslab T-T dimers and to induce desired structural transitions in the $Gd_5Ga_xGe_{4-x}$,[17] $Gd_5Si_{4-x}P_x$,[16] $La_{5-x}Ca_xGe_4$ and $Ce_{5-x}Ca_xGe_4$ systems.[18] The size effect associated with a larger p-element was used to stretch dimers in the $Gd_5Si_{4-x}Sn_x$ system.[19]

Combined VEC and size effects are expected to be even more consequential in breaking of the interslab T-T dimers. It has been reported that introduction of larger and electron richer Sb (r_{cov}(Sb) = 1.39 Å vs. r_{cov}(Si) = 1.17 Å)[20] into Gd_5Si_4 leads to the complete cleavage of the interslab dimers for the $Gd_5Si_2Sb_2$ composition.[21] $Gd_5Si_2Sb_2$ has

been characterized through the powder X-ray diffraction (XRD) and assigned a Sm_5Ge_4-type structure (*Pnma* space group). A related $Gd_5Si_{2.64}Sb_{1.36}$ phase has been reported to adopt the same Sm_5Ge_4-type structure.[22] Interestingly, previous research on the $RE_5X_2Sb_2$ phases (RE = Y, Gd, Tb, Dy, Ho, Er, Tm, Yb; X = Si or Ge) indicated formation of ternary phases with the Eu_5As_4-type structure (*Cmca*) for all RE metals except Gd and Yb.[23] Again, the structural analysis was done using the powder XRD methods. Since the Sm_5Ge_4- and Eu_5As_4-type structures are quite similar, i.e. they are built from structurally identical ${}_\infty^2[RE_5T_4]$ slabs with broken T-T dimers between them, they are expected to generate similar powder diffraction patterns, which can be difficult to distinguish. Additionally, characterization of the Gd-containing phases using the Cu radiation (the most common X-ray source on powder instruments) is rather challenging as the Gd fluorescence has an adverse affect on the resolution and background. This inconsistency regarding the Gd system was one of the impetuses for the detailed structural studies. In addition, combination of the geometric and electronic parameters can be very effective in achieving novel phases with unique physico-chemical properties. Here, we report structural, magnetic and magnetocaloric properties of the $Gd_5Si_{4-x}Sb_x$ phases.

6.3 Experimental

6.3.1 Synthesis and X-ray structure analysis

Starting materials were pieces of gadolinium (99.99 wt.%, distilled grade, Metall Rare Earth Limited, China), silicon (99.999 wt.%, Alfa Aesar) and Sb (99.999 wt.%, CERAC Inc.). The $Gd_5Si_{4-x}Sb_x$ samples with x = 0.5, 1.0, 1,5, 2.0, 2.5, 3.0 and 3.5 and a

total mass of 1 gram were arc-melted four times to achieve homogeneity. Extra 3 mg of Sb was added to all samples to compensate for anticipated Sb losses. The total losses were less than 0.5 wt. %. To improve crystallinity and homogeneity, the samples were annealed at 800°C for 2 weeks in evacuated silica tubes with subsequent quenching in cold water.

X-ray powder diffraction data for the annealed samples were obtained on a PANalytical X'Pert Pro diffractometer with a linear X'Celerator detector using the CoK_α radiation. Lattice parameters and phase analyses were derived from the Rietveld refinement using the FullProf software[24] (Table 6.1). Single crystal data were collected on a STOE IPDS II diffractometer with the MoKα radiation in the whole reciprocal sphere. Numerical absorption correction was based on the crystal shape obtained from optical face indexing with subsequent optimization against equivalent reflections using the STOE X-Shape software.[25] The structures were solved and refined using the SHELXS and SHELXL programs,[26] respectively (Table 6.2, 6.3).

More details on the crystal structures are available from the Fachinformationszentrum Karlsruhe, 76344 Eggenstein-Leopoldshafen, Germany, (fax: +49 7247 808 666; e-mail: crysdata@fiz-karlsruhe.de) on quoting the depository CSD number 421230 for $Gd_5Si_{2.79}Sb_{1.21}$, 421231 for $Gd_5Si_{2.27}Sb_{1.73}$, 421232 for $Gd_5Si_{1.73}Sb_{2.27}$, 421233 for $Gd_5Si_{1.72}Sb_{2.28}$ and 421234 for $Gd_5Si_{0.9}Sb_{3.1}$ and also from the Supporting information.

Table 6.1. Phase composition and lattice parameters for the $Gd_5Si_{4-x}Sb_x$ samples (x = 0.5-3) from the X-ray powder and single crystal diffraction

Sample	XRD method	Phase	Str. type (sp. gr)	*a/b/c*, Å
$Gd_5Si_{3.5}Sb_{0.5}$	powder	$Gd_5Si_{4-x}Sb_x$	Gd_5Si_4 (*Pnma*)	7.4725(5)/14.807(1)/7.7786(6)
		$Gd_5Si_{4-x}Sb_x$	Sm_5Ge_4 (*Pnma*)	7.7700(8)/14.910(1)/7.8012(8)
Gd_5Si_3Sb	single crystal	$Gd_5Si_{2.79}Sb_{1.21}$	Sm_5Ge_4 (*Pnma*)	7.7985(5)/14.9681(11)/7.8247(6)
	powder	$Gd_5Si_{4-x}Sb_x$	Sm_5Ge_4 (*Pnma*)	7.7879(5)/14.962(1)/7.8344(5)
		$Gd_5Si_{4-x}Sb_x$	Gd_5Si_4 (*Pnma*)	-[a]
$Gd_5Si_{2.5}Sb_{1.5}$	single crystal	$Gd_5Si_{2.27}Sb_{1.73}$	Sm_5Ge_4 (*Pnma*)	7.856(1)/15.105(2)/7.8769(8)
	powder	$Gd_5Si_{4-x}Sb_x$	Sm_5Ge_4 (*Pnma*)	7.8418(7)/15.064(1)/7.8852(7)
		$Gd_5Si_{4-x}Sb_x$	Gd_5Si_4 (*Pnma*)	-[a]
$Gd_5Si_2Sb_2$	single crystal	$Gd_5Si_{1.73}Sb_{2.27}$	Eu_5As_4 (*Cmca*)	15.211(2)/7.9382(8)/7.9376(7)
	powder	$Gd_5Si_{4-x}Sb_x$	Eu_5As_4 (*Cmca*)	15.196(2)/7.8923(9)/7.9542(9)
		Gd_5Si_3[b]	Mn_5Si_3 ($P6_3/mmc$)	8.453(7)/8.453(7)/6.322(9)
$Gd_5Si_{1.5}Sb_{2.5}$	single crystal	$Gd_5Si_{1.72}Sb_{2.28}$	Eu_5As_4 (*Cmca*)	15.246(6)/7.943(3)/7.972(3)
	powder	$Gd_5Si_{4-x}Sb_x$	Eu_5As_4 (*Cmca*)	15.216(1)/7.9352(8)/7.9772(8)
		GdSb[b]	NaCl ($Fm\bar{3}m$)	6.219(1)/6.219(1)/6.219(1)
Gd_5SiSb_3	single crystal	$Gd_5Si_{0.9}Sb_{3.1}$	Eu_5As_4 (*Cmca*)	15.283(6)/8.050(6)/8.042(4)
	powder	$Gd_5Si_{4-x}Sb_x$	Eu_5As_4 (*Cmca*)	15.209(2)/7.9942(9)/8.0352(9)

[a] the lattice parameters could not be refined reliably due to a small amount of the phase in the sample
[b] substitution, if any at all, by Sb or Si in Gd_5Si_3 and GdSb appears to be very small based on the lattice parameters, however it cannot be excluded

Table 6.2. Crystallographic parameters and refinement results for the $Gd_5Si_{4-x}Sb_x$ single crystals (MoK_α radiation, 2θ range = 5 - 59°[a], $z = 4$)

Sample	Gd_5Si_3Sb	$Gd_5Si_{2.5}Sb_{1.5}$	$Gd_5Si_2Sb_2$	$Gd_5Si_{1.5}Sb_{2.5}$	Gd_5SiSb_3
Refined composition	$Gd_5Si_{2.79(2)}Sb_{1.21(2)}$	$Gd_5Si_{2.27(3)}Sb_{1.73(3)}$	$Gd_5Si_{1.73(1)}Sb_{2.27(1)}$	$Gd_5Si_{1.72(2)}Sb_{2.28(2)}$	$Gd_5Si_{0.9(1)}Sb_{3.1(1)}$
Structure type	Sm_5Ge_4	Sm_5Ge_4	Eu_5As_4	Eu_5As_4	Eu_5As_4
Space group	*Pnma*	*Pnma*	*Cmca*	*Cmca*	*Cmca*
a (Å)	7.7985(5)	7.856(1)	15.211(2)	15.246(6)	15.283(6)
b (Å)	14.9681(11)	15.105(2)	7.9382(8)	7.943(3)	8.050(6)
c (Å)	7.8247(6)	7.8769(8)	7.9376(7)	7.972(3)	8.042(4)
Volume (Å^3)	913.4(1)	934.7(2)	958.5(2)	965.4(6)	989.4(1)
Index ranges	$-10 \le h \le 10$, $-20 \le k \le 17$, $-10 \le l \le 10$	$-10 \le h \le 9$, $-17 \le k \le 20$, $-10 \le l \le 10$	$-20 \le h \le 20$, $-10 \le k \le 10$, $-10 \le l \le 10$	$-20 \le h \le 20$, $-10 \le k \le 10$, $-8 \le l \le 10$	$-15 \le h \le 15$, $-8 \le k \le 8$, $-8 \le l \le 8$
Reflections collected	9064	9420	4874	4172	1732
Independent reflections	1277 [R_{int} = 0.0661]	1308 [R_{int} = 0.0737]	676 [R_{int} = 0.0735]	658 [R_{int} = 0.2004]	270 [R_{int} = 0.2823]
Completeness to max 2θ (%)	98.8	98.8	99.7	97.9	99.6
Data/restraints/parameters	1277/0/49	1308/0/50	676/0/29	658/0/29	270/0/27
Goodness-of-fit on F^2	1.183	1.162	1.084	0.995	0.747
Final R indices [$I>2\sigma(I)$]	R_1 = 0.0683, wR_2 = 0.1608	R_1 = 0.0737, wR_2 = 0.1817	R_1 = 0.0462, wR_2 = 0.1104	R_1 = 0.0709, wR_2 = 0.1696	R_1 = 0.0688, wR_2 = 0.1519
R indices (all data)	R_1 = 0.0895, wR_2 = 0.1684	R_1 = 0.0970, wR_2 = 0.1914	R_1 = 0.0664, wR_2 = 0.1188	R_1 = 0.1231, wR_2 = 0.2050	R_1 = 0.1668, wR_2 = 0.1888
Extinction coefficient	0.0007(2)	0.0027(3)	0.0004(1)	0.0006(2)	0.0001(2)
Largest diff. peak/hole (e/A^3)	6.192/-5.092	5.322/-6.404	4.322/-2.803	4.373/-4.530	2.170/-2.301
Minority fraction [b]	0	0	0.13	0.14	0

[a] 2θ range = 5 - 40° for the single crystal from the Gd_5SiSb_3 sample

[b] minority fraction is the fraction of the residual electron density resulting from the stacking faults. The relationship between the minority fraction and the faulting probability is discussed in Supporting Information

Table 6.3. Atomic and isotropic temperature (U) parameters for the $Gd_5Si_{4-x}Sb_x$ single crystals

Atom	Site	Occupancy	*x/a*	*y/b*	*z/c*	U (Å^2)
$Gd_5Si_{2.79}Sb_{1.21}$						
Gd1	8*d*	1	-0.0442(2)	0.6097(1)	0.1775(1)	0.018(1)
Gd3	8*d*	1	0.3937(2)	0.1217(1)	0.1667(1)	0.018(1)
Gd2	4*c*	1	0.2232(2)	1/4	0.5036(2)	0.014(1)
Sb/Si1	8*d*	0.58/0.42(1)	0.2296(3)	0.0417(2)	0.4781(2)	0.012(1)
Si/Sb2	4*c*	0.94/0.06(2)	0.0978(11)	1/4	0.1140(9)	0.016(3)
Si3	4*c*	1	0.3407(13)	1/4	0.8723(11)	0.014(2)
$Gd_5Si_{2.27}Sb_{1.73}$						
Gd1	8*d*	1	-0.0603(2)	0.6150(1)	0.1740(2)	0.026(1)
Gd3	8*d*	1	0.4051(2)	0.1223(1)	0.1675(1)	0.022(1)
Gd2	4*c*	1	0.2342(2)	1/4	0.5026(2)	0.020(1)
Sb/Si1	8*d*	0.82/0.18(1)	0.2391(2)	0.0431(1)	0.4883(2)	0.020(1)
Si/Sb2	4*c*	0.95/0.05(1)	0.1080(10)	1/4	0.1209(10)	0.019(3)
Si/Sb3	4*c*	0.96/0.04(1)	0.3594(12)	1/4	0.8709(10)	0.022(3)
$Gd_5Si_{1.73}Sb_{2.27}$						
Gd1	4*a*	1	0	0	0	0.018(1)
Gd2	16*g*	1	0.1308(1)	0.1683(1)	0.3323(1)	0.023(1)
Sb1/Si	8*d*	0.96/0.04(1)	0.2053(1)	0	0	0.020(1)
Si2/Sb	8*f*	0.83/0.17(1)	0	0.3663(4)	0.1327(4)	0.018(1)
$Gd_5Si_{1.72}Sb_{2.28}$						
Gd1	4*a*	1	0	0	0	0.032(1)
Gd2	16*g*	1	0.1312(1)	0.1678(2)	0.3326(2)	0.038(1)
Sb/Si1	8*d*	0.95/0.05(2)	0.2050(2)	0	0	0.033(1)
Si/Sb2	8*f*	0.81/0.19(2)	0	0.3648(8)	0.1332(7)	0.030(2)
$Gd_5Si_{0.9}Sb_{3.1}$						
Gd1	4*a*	1	0	0	0	0.030(3)
Gd2	16*g*	1	0.1325(3)	0.1656(7)	0.3356(5)	0.037(2)
Sb1	8*d*	1	0.2030(5)	0	0	0.035(3)
Sb/Si2	8*f*	0.55/0.45(5)	0	0.3630(20)	0.1364(15)	0.039(7)

6.3.2 Quantitative elemental analysis

Energy dispersive spectroscopic (EDS) elemental analysis was performed on the $Gd_5Si_{3.5}Sb_{0.5}$ sample using a JEOL JSM-7000F electron microscope with internal standards. The alloy annealed at 800°C was finely polished on a Struers automatic polishing machine with a colloidal silica suspension used during the final stage.

6.3.3 Electronic structure calculations

Tight-binding, linear-muffin-tin-orbital calculations using the atomic sphere approximation (TB-LMTO-ASA)[27] were performed for the Gd_5Si_4 phase and hypothetical Gd_5Si_3Sb using the Stuttgart program[28] (Figure 6.5). For Gd_5Si_3Sb, the atomic parameters were taken from the $Gd_5Si_{2.79}Sb_{1.21}$ single crystal structure (Sm_5Ge_4-type structure). By assuming a linear dependence of the lattice parameters on the Sb content, x, in $Gd_5Si_{4-x}Sb_x$, cell dimensions for hypothetical Gd_5Si_3Sb were obtained through the linear extrapolation of the structural parameters for the phases with the higher Sb content to the Gd_5Si_3Sb composition. More precisely, a mathematical expression for the dependence of the cell parameters on x was obtained through a linear least-square fit of the experimental data. The coefficients of determination, R^2, for the corresponding regressions had the values of 0.996, 0.995 and 0.937, and the resulting cell parameters for Gd_5Si_3Sb were a = 7.645, b = 14.810 and c = 7.680 Å. In order to populate the T-T dimers with the Sb/Si atoms, the symmetry was lowered from *Pnma* to $Pn2_1a$. Gd *f*-electrons were treated as core ones during the calculations. Structural parameters for the Gd_5Si_4 phase were taken from the single crystal refinement results.[16]

6.3.4 Magnetic measurements

Magnetization in a field-cooled (FC) mode for the polycrystalline $Gd_5Si_{4-x}Sb_x$ samples with x = 0.5, 1.0, 1,5, 2.0, 2.5, and 3.0 was measured on a Quantum Design SQUID magnetometer in the 100 Oe field. The magnetocaloric effect for $Gd_5Si_2Sb_2$, $Gd_5Si_{1.5}Sb_{2.5}$ and Gd_5SiSb_3 was evaluated from the magnetization vs. field (M vs. H) data

measured around the Curie temperatures with 5 or 6 K increments (Figure 6.8, supporting information). The magnetic field changed from 0 to 50 kOe in 2 kOe steps.

6.4 Results and discussion

6.4.1 Homogeneity regions for the $Gd_5Si_{4-x}Sb_x$ phases

Homogeneity regions for the $Gd_5Si_{4-x}Sb_x$ phases are summarized in Figure 6.1. From X-ray powder diffraction, the $Gd_5Si_{3.5}Sb_{0.5}$ and Gd_5Si_3Sb samples were found to contain both the Gd_5Si_4-type and Sm_5Ge_4-type phases, thus indicating that homogeneity region for the Gd_5Si_4-type phase ends at $x < 0.5$ and that for the Sm_5Ge_4-type phase starts at $x > 1.0$. The X-ray phase analysis of the $Gd_5Si_{3.5}Sb_{0.5}$ sample yielded the 85 wt. % presence for the Gd_5Si_4-type phase, which suggests that the composition of the Gd_5Si_4-type phase must be close to $Gd_5Si_{3.6}Sb_{0.4}$, based on the mixture rule. As no X-ray quality crystals of the Gd_5Si_4-type phase could be extracted from the two samples, the EDS analysis was performed on the $Gd_5Si_{3.5}Sb_{0.5}$ sample in order to establish the right compositional boundary of the Gd_5Si_4-type phase. The composition obtained was $Gd_{4.90(5)}Si_{3.72(4)}Sb_{0.38(5)}$ (when normalized to nine atoms) which agrees with the conclusions drawn from the X-ray analysis. Assuming the Sb amount to be $x = 0.38$, we can write the formula of this phase as $Gd_5Si_{3.62}Sb_{0.38}$ and we will use this formula during our discussion. While the formula may not represent the real composition, it is certainly close to the real one as the EDS composition embraces this formula within the three standard deviations. The left compositional boundary of the Sm_5Ge_4-type phase was

determined from the Gd_5Si_3Sb single crystal, whose composition was refined to $Gd_5Si_{2.79(2)}Sb_{1.21(2)}$ (Table 6.3).

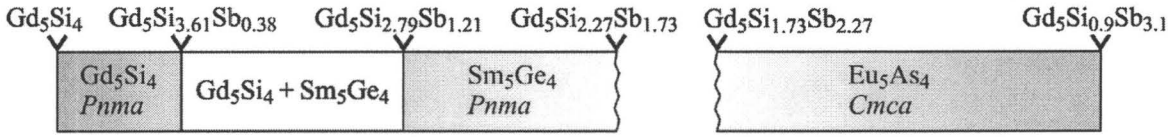

Figure 6.1. Homogeneity regions for the $Gd_5Si_{4-x}Sb_x$ phases. The wavy lines indicate that the homogeneity regions extend at least till the values given

A single crystal from the $Gd_5Si_{2.5}Sb_{1.5}$ sample yielded a Sm_5Ge_4-type structure with the $Gd_5Si_{2.27(3)}Sb_{1.73(3)}$ composition. Difference between the loaded and observed compositions is due to the presence of small amounts of a non-equilibrium Gd_5Si_4-type impurity (less than 5 wt. %), which was identified from the X-ray powder diffraction and also from the SEM analysis (not discussed here). We believe that formation of the congruently melting Gd_5Si_4-type impurity precedes the solidification of the Sm_5Ge_4-type phase, and thus shifts the effective composition of the main phase to the Sb-richer region. Annealing of the sample at 800°C for 2 weeks had no detectable effect on the ratio of the two phases. Based on the $Gd_5Si_{2.27(3)}Sb_{1.73(3)}$ composition, we can state that the right homogeneity boundary for the Sm_5Ge_4-type phase extends at least till $x = 1.73(3)$. The sample with a higher Sb concentration ($x = 2.0$) did not contained a Sm_5Ge_4-type phase, and thus could not be used to refine the right boundary of the Sm_5Ge_4-type phase.

Starting from $x = 2.0$, the major phase was found to adopt the Eu_5As_4-type (*Cmca* space group, Table 6.2) structure, with impurities being Gd_5Si_3 for $x = 2.0$ and GdSb for $x = 2.5$ at ca. 10 wt. %. A single crystal from the $Gd_5Si_2Sb_2$ sample was refined to the

$Gd_5Si_{1.73(1)}Sb_{2.27(1)}$ composition, and that from the $Gd_5Si_{1.5}Sb_{2.5}$ sample to $Gd_5Si_{1.72(2)}Sb_{2.28(2)}$ (Table 6.3). Although the refined compositions appear to be similar within one standard deviation, an increase in the Sb content is obvious from the expanded cell and is also reflected in the magnetization data (see below). Annealing of the samples did not produce any detectable change in the sample compositions. As in the case with $Gd_5Si_{2.5}Sb_{1.5}$, solidification of the congruently melting Gd_5Si_3 and GdSb binaries is believed to precede the formation of the phases of interest and, thus, to make them Sb-richer/poorer. Additionally, the single crystal compositions may not represent of the bulk compositions which may be closer to the loading compositions.

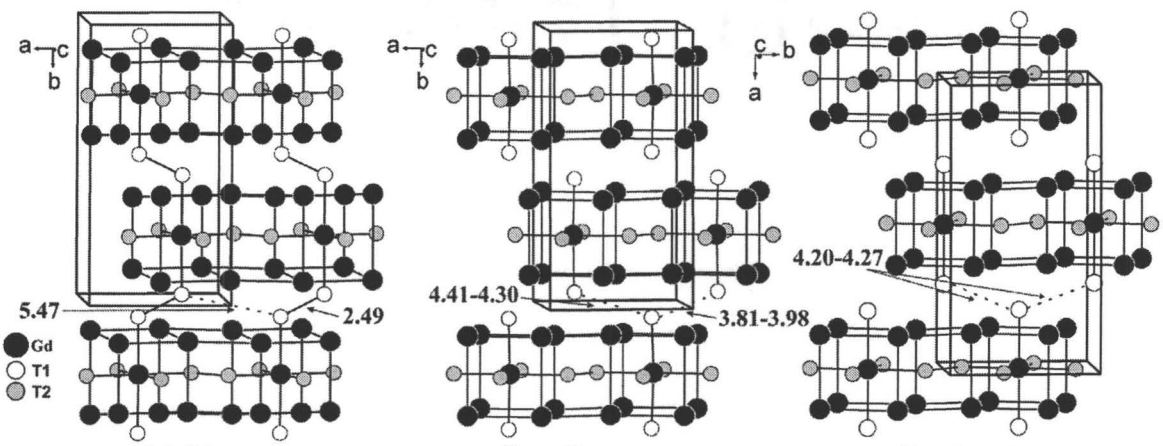

Figure 6.2. Three $Gd_5Si_{4-x}Sb_x$ structures with different interslab *T*1-*T*1 bonds. The intraslab *T*2 atoms represent two crystallographic sites, *T*2 and *T*3, for the Gd_5Si_4- and Sm_5Ge_4-type structures

A crystal extracted from the Gd_5SiSb_3 sample was refined to the $Gd_5Si_{0.9(1)}Sb_{3.1(1)}$ composition (Table 6.3). The data were collected only up to $2\theta = 40°$ since the high-angle

data consisted mainly of poorly defined and overlapped peaks. Poor crystallinity and multi-component nature (multi-twinning) of the crystal resulted in the low compositional accuracy. A multi-component approach during the integration and refinement did not improve the outcome. The $Gd_5Si_{0.5}Sb_{3.5}$ sample contained the Th_3P_4-type $Gd_4Si_xSb_{3-x}$ and NaCl-type $GdSi_xSb_{1-x}$ phases, as concluded from the powder X-ray diffraction. Absence of a RE_5X_4-type structure might be explained by the absence of the corresponding Gd_5Sb_4 binary, to which the targeted phase was close in composition.

6.4.2 Structural features of the $Gd_5Si_{4-x}Sb_x$ phases

Three structures are present in the $Gd_5Si_{4-x}Sb_x$ system (Figure 6.2): the Gd_5Si_4-type one for the low Sb concentration ($x \leq 0.38$), the Sm_5Ge_4-type one for the intermediate Sb amount ($1.21 \leq x \leq 1.73$) and the Eu_5As_4-type one for the Sb-richer phases ($2.27 \leq x \leq 3.1$). Detailed descriptions of the Gd_5Si_4- and Sm_5Ge_4-type structures (*Pnma* space group for both) can be found elsewhere,[15,29,30] therefore only a brief analysis of these two structures will be provided here. Both structures are built from the two-dimensional $_\infty^2[Gd_5T_4]$ slabs (T is Si or a Si/Sb mixture in $Gd_5Si_{4-x}Sb_x$). While in the Gd_5Si_4-type structures the slabs are connected through the interslab $T1$-$T1$ dimers ($d_{T\text{-}T} <$ 2.7 Å), these dimers are broken in the Sm_5Ge_4-type structures ($d_{T\text{-}T} >$ 3.4 Å). We will refer to the $T1$-$T1$ dimers as T-T. Regardless of where or not the interslab dimers are broken, there are two sets of the interslab $T\cdots T$ distances, shorter and longer ones, that yield a unique, herring-bone stacking of the $_\infty^2[Gd_5T_4]$ slabs and the *ABAB*-type slab sequence.[29]

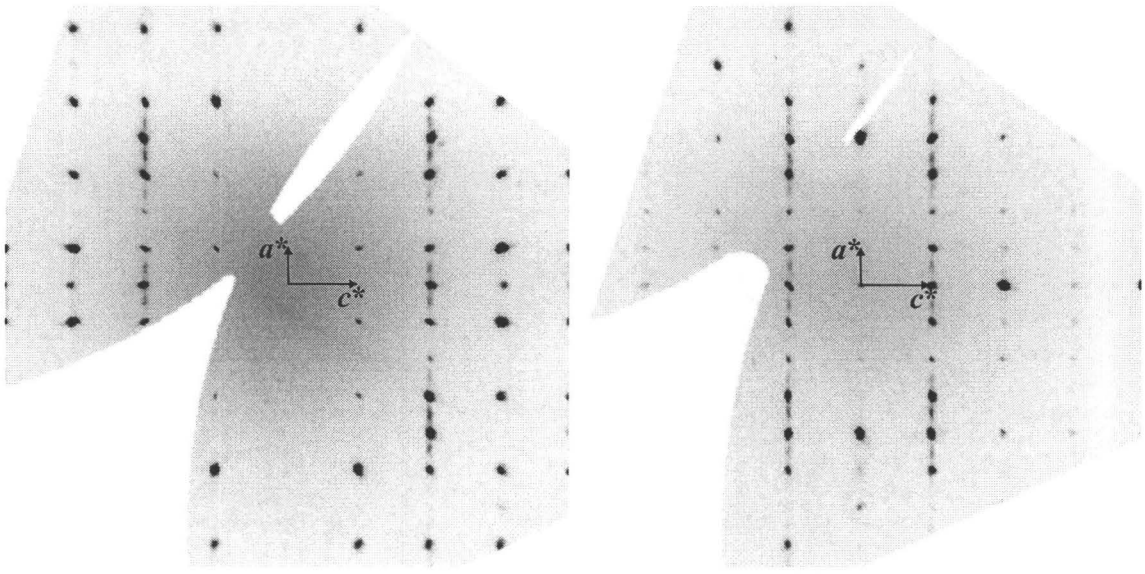

Figure 6.3. Reciprocal *h*1*l* (left) and *h*2*l* (right) layers for the $Gd_5Si_{1.73}Sb_{2.27}$ crystal

Increase in the Sb amount ($2.27 \leq x \leq 3.1$) yields a Eu_5As_4-type structure (*Cmca* space group, *ABAB* slab stacking, Figure 6.2), in which not only the interslab dimers are broken but also the interslab *T*···*T* distances are equivalent. Equivalency of the *T*···*T* distances allows for stacking faults with a fault vector of (0, 1/2, 1/2), which corresponds to randomly replacing an *A*(0,0) slab with a *C*(1/2, 1/2) slab or a *B*(1/2, 0) slab with a *D*(0, 1/2) slab (the numbers in parentheses are the coordinates within the *yz* fault plane, with the *A* slab being taken as an origin). The stacking faults result in (1) appearance of diffuse scattering lines along *a**, (2) presence of the $k + l = 2n + 1$ ($k \neq 3n$ and $l \neq 3n$) selection rule for diffuse lines (Figure 6.3), and (3) emergence of residual electron density in the $_{\infty}^{2}[RE_5T_4]$ slabs during the refinement. A comprehensive analysis of the scattering phenomena associated with such stacking faults was performed by the authors for the

$Gd_5Si_{4-x}Bi_x$ system and a reader is referred to the relevant article for more details.[31] The refinement procedures derived for the $Gd_5Si_{4-x}Bi_x$ system were applied to the refinement of the Eu_5As_4-type Sb-containing phases (see Chapter 8).

The structural transformations in the $Gd_5Si_{4-x}Sb_x$ system resemble transitions observed in other RE_5T_4 systems.[14, 16, 19] The two features, which are common among the RE_5T_4 phase and also present in our case, are the rigidity of the $_\infty^2[RE_5T_4]$ slabs and the flexibility of the interslab dimers. While the length of the interslab dimers can be tuned through the variety of parameters, we believe that the combination of both the size and electronic effects associated with the Sb substitution results in the dimer cleavage and phase transitions in $Gd_5Si_{4-x}Sb_x$. As shown for the $Gd_5Si_{4-x}Sn_x$ system, introduction of larger Sn atoms (r_{cov}(Si) = 1.17 Å vs. r_{cov}(Sn) = 1.42 Å)[20] leads to the pronounced dimer stretching: $d_{T\text{-}T}$ = 2.49 → 3.04 Å for x = 2. However in the $Gd_5Si_{4-x}Sb_x$ system, the geometric effects by themselves are not expected to break the dimers completely ($d_{T\text{-}T}$ = 3.81 Å for x = 1.21) since Sb is smaller than Sn (r_{cov}(Sb) = 1.39 Å vs. r_{cov}(Sn) = 1.42 Å).[20] Thus, electronic effects associated with a larger electron count must be more consequential for dimer breaking. Indeed, the valence electron count has been shown to be a very effective tool in controlling the dimer length, e.g. a full dimer cleavage, $d_{T\text{-}T}$ = 2.49 → 3.74 Å, was achieved in $Gd_5Si_{4-x}P_x$ for the relatively modest P amount of x = 1.25. Thus, both geometric and electronic effects (with electronic one being more consequential) are believed to drive the structural transitions in the $Gd_5Si_{4-x}Sb_x$ system.

6.4.3 Absence of a RE_5T_4-type structure for $x \approx 1$

While the *T*-*T* dimer cleavage drives the structural transitions in $Gd_5Si_{4-x}Sb_x$, it appears to be also the reason for absence of a RE_5T_4 phase for $x \approx 1$ (a two-phase region exist for $0.38 < x < 1.21$). Interestingly, it has been also reported that no RE_5T_4-type phase could be obtained in the $Gd_5Si_{4-x}Bi_x$ system for $x \approx 1$. We performed a structural analysis and electronic structure calculations on hypothetical Gd_5Si_3Sb structure to gain insights into this phenomenon. We start with the assumption that the combination of the geometric and electronic factors would render a Sm_5Ge_4-type structure with broken dimers for $x = 1$.

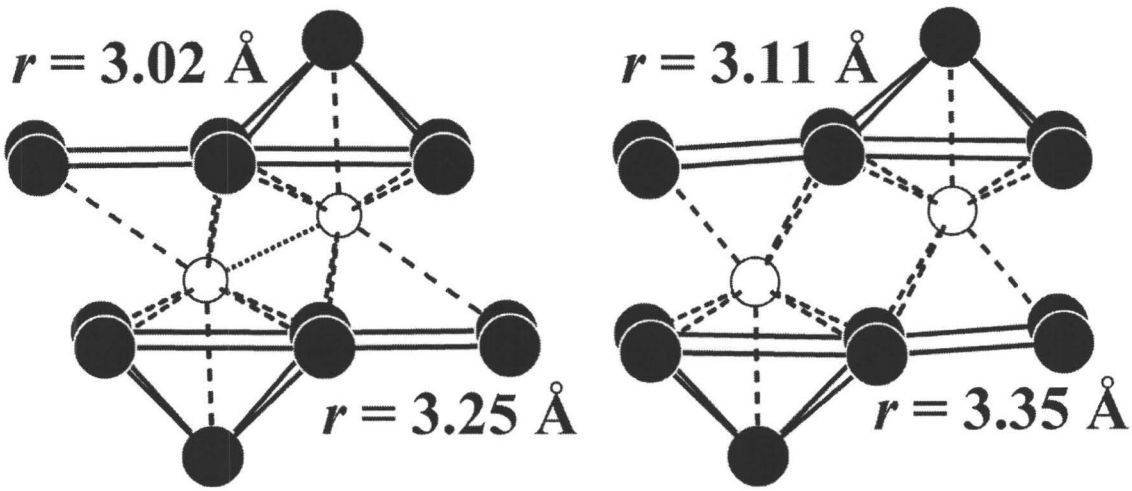

Figure 6.4. Average interslab *T*-Gd distances in Gd_5Si_4 (left) and $Gd_5Si_{2.79}Sb_{1.21}$ (right). The top values represent distances for the upper *T* atom to the upper, "its own" Gd layer, while the bottom values give distances for the same *T* atom to the lower, opposite Gd layer

We also assume that the two-dimensional $_{\infty}^{2}[RE_5T_4]$ slabs are rigid and the intraslab bonding is not perturbed when compared with the neighboring $Gd_5Si_{4-x}Sb_x$ phases. The

latter assumption is quite reasonable, as the intraslab atomic arrangements remain very similar except for the slightly larger interatomic distances induced by the lattice expansion upon the Sb substitution.

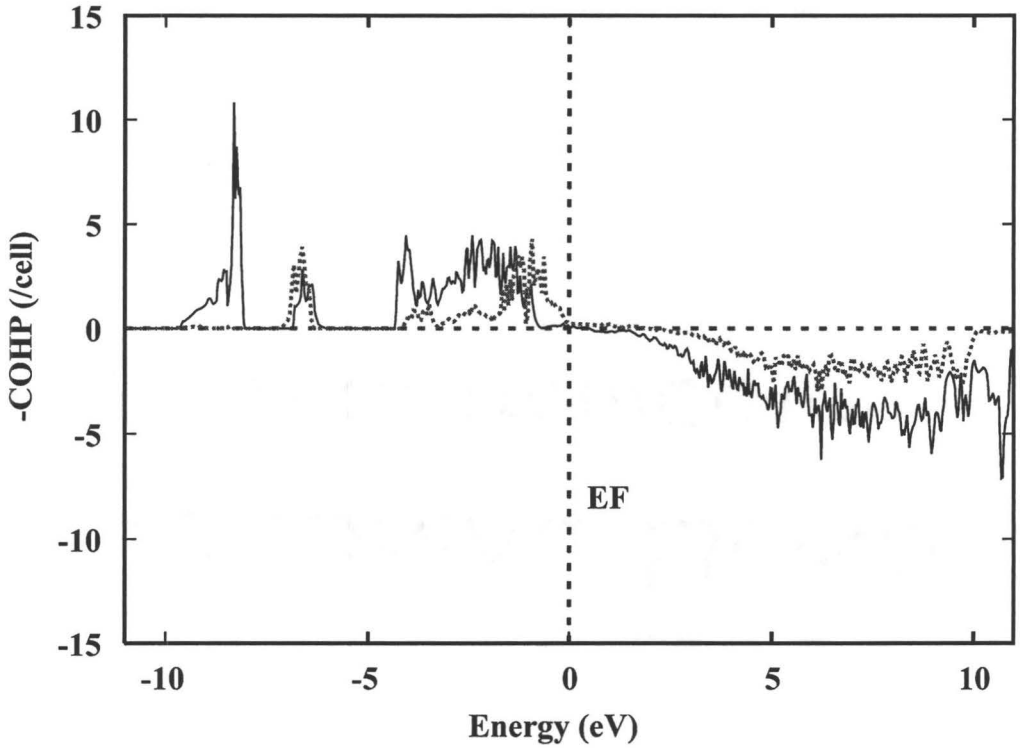

Figure 6.5. COHP curves for the interslab Si-Gd bonds in the hypothetical Gd_5Si_3Sb (dotted line) and real Gd_5Si_4 (solid line) structures

We want to see if the bonding interactions between the interslab *T* and neighboring Gd atoms are optimized. Based on the single crystal results for $Gd_5Si_{2.79}Sb_{1.21}$, we expect the interslab *T* site in hypothetical Gd_5Si_3Sb to be occupied by equi-atomic mixture of Si/Sb (i.e. all Sb atoms are on this site). The average *T*-Gd distances in Gd_5Si_3Sb are expected to be close to the ones observed in $Gd_5Si_{2.79}Sb_{1.21}$ (Figure 6.4, on the right). In $Gd_5Si_{2.79}Sb_{1.21}$, the average *T*-Gd to its "own, closer" Gd

layer is 3.11 Å, whereas to the "other" Gd layer is 3.35 Å. While these *T*-Gd distances in $Gd_5Si_{2.79}Sb_{1.21}$ appear to be reasonable for Sb-Gd bonds (the sum of the Sb and Gd atomic radii is 3.21 Å),[32] they are too large for the Si-Gd interactions (the sum of the Si and Gd atomic radii is 2.97 Å).[32] For comparison, the average Si-Gd distances in Gd_5Si_4 are 3.02 Å and 3.25 Å to the two Gd layers[16] (Figure 6.4, left). Thus in Gd_5Si_3Sb, the *T*-Gd interactions will not be optimized for the half of the interslab *T* atoms, namely the Si ones. The crystal orbital Hamilton population (COHP) calculations performed for the interslab Si-Gd bonds in the hypothetical Gd_5Si_3Sb and real Gd_5Si_4 structure support this argument (Figure 6.5). The integrated COHP (-ICOHP) values are much larger for the interslab Si-Gd interactions in Gd_5Si_4 than in Gd_5Si_3Sb (12.91 eV/cell vs. 5.94 eV/cell) even despite the lower valence electron concentration in Gd_5Si_4.

Thus, the matrix effect imposed by bigger Sb atoms precludes effective bonding for smaller interslab Si atoms and appears to make the Gd_5Si_3Sb phase unstable in comparison with the neighboring Sb-poorer and -richer phases. In order to stabilize a Sm_5Ge_4-type structure, extra Sb atoms have to be introduced into the interslab *T* sites. While this will optimize the interslab *T*-Gd interaction, it will also shift the composition to the Sb-richer side as observed experimentally. We believe that the same arguments can be applied to explain the absence of a RE_5T_4-type phase in the $Gd_5Si_{4-x}Bi_x$ system for $x \approx 1$.

6.4.4 Magnetic properties of $Gd_5Si_{4-x}Sb_x$

The $Gd_5Si_{3.5}Sb_{0.5}$ and Gd_5Si_3Sb samples show two ferromagnetic transitions at 164 K and 336 K (Figure 6.6), which is consistent with the two-phase composition of the samples. The transition at 336 K is attributed to the Gd_5Si_4-type phase and its temperature is equal to that of pure Gd_5Si_4.[33] The Sb substitution of x = 0.38(5) in the Gd_5Si_4-type phase appears to have a negligible effect on the magnetic interactions. A similar behavior was observed for the $Gd_5Si_{4-x}P_x$ phases in the P-poor region.[16] The 164 K transition is associated with the ferromagnetic ordering in the Sm_5Ge_4-type phase.

A ferromagnetic transition at 227 K in the $Gd_5Si_{2.5}Sb_{1.5}$ sample represents magnetic ordering in the Sm_5Ge_4-type phase. A small bump around 336 K corresponds to the Gd_5Si_4-type impurity, which was also identified from the powder diffraction. Weiss temperatures and effective magnetic moments of Gd atoms for the Gd_5Si_4- and Gd_5Ge_4-type phases in the $Gd_5Si_{3.5}Sb_{0.5}$, Gd_5Si_3Sb and $Gd_5Si_{2.5}Sb_{1.5}$ samples could not be determined reliably due to the multiphase nature of the samples.

Table 6.4. Magnetic parameters for the $Gd_5Si_{4-x}Sb_x$ samples

Sample	Major phase	T_c, K	θ, K	μ_{eff}(Gd), μ_B	$-\Delta S$, J/kg K
$Gd_5Si_{3.5}Sb_{0.5}$	Gd_5Si_4-type	336	–*	–*	N/A
Gd_5Si_3Sb	Sm_5Ge_4-type	164	–*	–*	N/A
$Gd_5Si_{2.5}Sb_{1.5}$	Sm_5Ge_4-type	227	–*	–*	N/A
$Gd_5Si_2Sb_2$	Eu_5As_4-type	254	255	7.76	3.7(4)
$Gd_5Si_{1.5}Sb_{2.5}$	Eu_5As_4-type	271	271	8.45	4.2(6)
Gd_5SiSb_3	Eu_5As_4-type	295	297	8.71	4.6(7)

* θ and μ_{eff}(Gd) could not be determined because of the multiphase nature of the samples

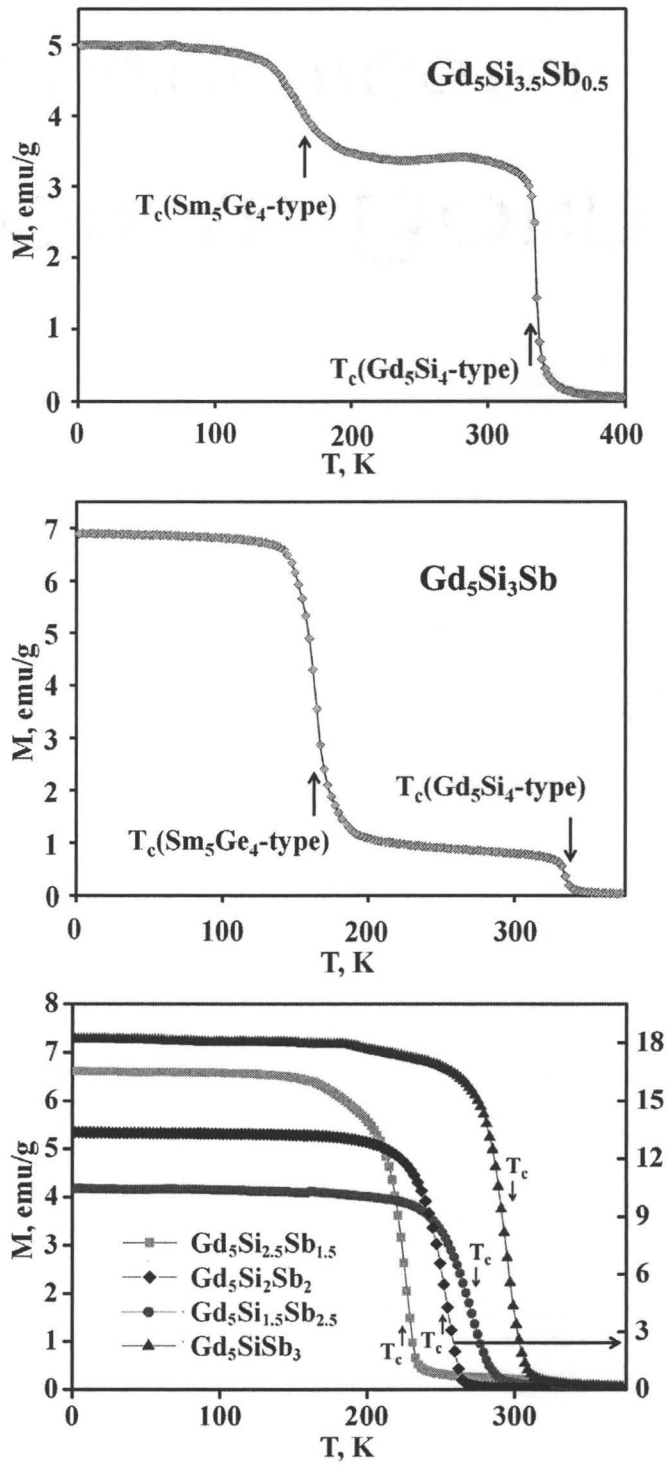

Figure 6.6. Magnetization versus temperature for the $Gd_5Si_{4-x}Sb_x$ samples

The $Gd_5Si_2Sb_2$, $Gd_5Si_{1.5}Sb_{2.5}$ and Gd_5SiSb_3 samples show single ferromagnetic transitions at 254, 271 and 295 K, respectively. Weiss temperatures extracted from the paramagnetic regions of the magnetization curves equal 255, 271 and 297 K, correspondingly, yielding the magnetic frustration indexes close to one as expected for the ferromagnetic transitions. Positive θ values confirm the ferromagnetic nature of interactions between the Gd atoms. Effective magnetic moments, μ_{eff}, for Gd atoms extracted from the paramagnetic regions for $Gd_5Si_2Sb_2$, $Gd_5Si_{1.5}Sb_{2.5}$ and Gd_5SiSb_3 are 7.76, 8.45 and 8.71 μ_B, respectively. While the Gd magnetic moment in $Gd_5Si_2Sb_2$ is close to the theoretical value of 7.94 μ_B[34] expected for Gd^{3+}, the $Gd_5Si_{1.5}Sb_{2.5}$ and especially Gd_5SiSb_3 samples yield larger values. Such phenomenon is often observed in the ferromagnetic Gd-containing metallic phases and is attributed to the polarization of conduction electrons, mainly Gd 5*d*, through the 4*f*-5*d* exchange interactions.[34-37]

6.4.5 Curie temperature versus Sb amount

In $Gd_5Si_{4-x}Sb_x$, the initial Gd_5Si_4-to-Sm_5Ge_4 transition accompanied by the cleavage of the interslab *T*-*T* dimers significantly lowers the Curie temperature from 336 K to 164 K as seen both for the $Gd_5Si_{3.5}Sb_{0.5}$ and Gd_5Si_3Sb samples (Table 6.4). Analogues behavior was observed in the $Gd_5Si_{4-x}P_x$ system during a similar Gd_5Si_4-to-Sm_5Ge_4 transition.[38] A further increase in the Sb amount promotes larger *T*···*T* separations ($d_{T\text{-}T}$ = 3.81 → 4.27 Å for x = 1.21 → 3.1), but surprisingly the Curie temperature goes up and reaches 295 K for Gd_5SiSb_3. Such behavior is rather remarkable and suggests that a different factor, not the interatomic distances, is more consequential in governing the

magnetic interactions. Magnetic interactions between the rare-earth atoms (or ions) are best described within the RKKY theory[39-41] according to which a Curie temperature depends both on the Fermi energy, E_F, and interatomic separations. Variations in the Gd-Gd distances during the Gd_5Si_4-to-Sm_5Ge_4 and Sm_5Ge_4-to-Eu_5As_4 transitions and also as a function of x for a given structure type are rather small and do not correlate well with the trend in Curie temperatures (analysis of the interatomic distances is provided in Supporting Information). On the other hand, changes in the concentration of the conduction electrons, N, which depends on E_F (within the free electron model E_F is proportional to $N^{2/3}$), mirrors relatively well the trend in the Curie temperatures (Figure 6.7).

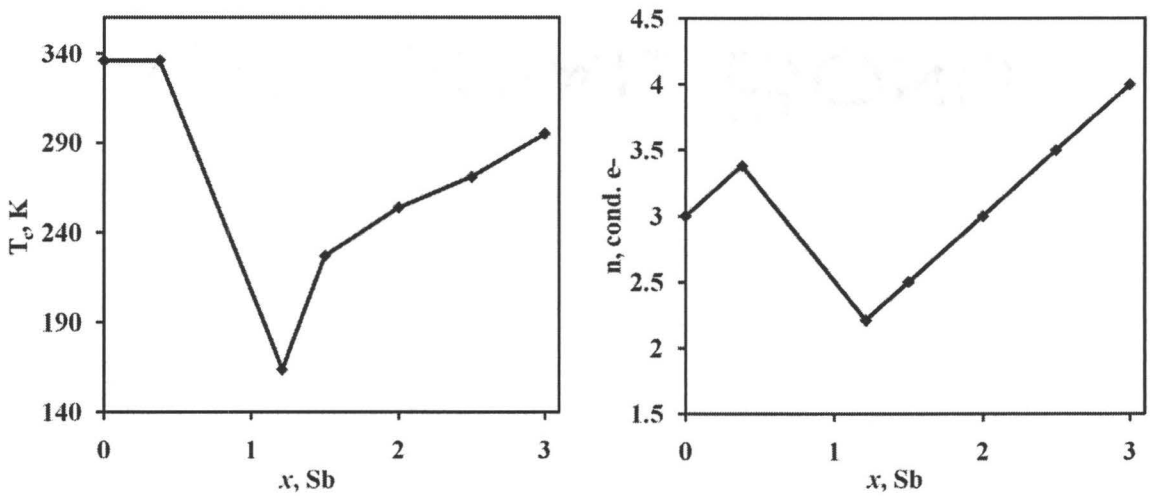

Figure 6.7. Curie temperature (left) and number of conduction electrons (right) as a function of antimony content in the $Gd_5Si_{4-x}Sb_x$ system

The concentration of conduction electrons can be estimated from the chemical formulas of the $Gd_5Si_{4-x}Sb_x$ phases. Considering that both the interslab and intraslab

dimers are intact in the Gd_5Si_4-type phases, the chemical formula of $Gd_5Si_{3.62}Sb_{0.38}$ (idealized EDS composition) can be written as $(Gd^{3+})_5(T_2^{6-})_2(3.38e^-)$, where $3.38e^-$ is the number of conduction electrons. In the Sm_5Ge_4- and Eu_5As_4-type phases half of the *T*-*T* dimers, namely the interslab ones, is broken, and their formulas can be given as $(Gd^{3+})_5(T_{(intra)2}^{6-})(T_{(inter)}^{4-})_2(\{1+x\}e^-)$, with x being the Sb amount (here x is the refined Sb amount). Thus, the number of conduction electrons in $Gd_5Si_{2.79}Sb_{1.21}$, $Gd_5Si_{2.27}Sb_{1.73}$, and $Gd_5Si_{0.9}Sb_{3.1}$ will be 2.21, 2.73 and 4.31, respectively. An increase in the Sb amount from $x = 0.38$ to 1.21 induces the initial Gd_5Si_4-to-Sm_5Ge_4 transition and significantly reduces the number of conduction electrons from 3.38 to 2.21 (Figure 6.7) even despite an increase in the total valence electron count associated with the Sb substitution (VEC = 31.38 → 32.21). However, further Sb substitution raises the conduction electron count and leads to higher Curie temperatures.

On going from Gd_5Si_4 to $Gd_5Si_{3.62}Sb_{0.38}$ (both adopt the Gd_5Si_4-type structure), the Curie temperature stays constant while the number of conduction electrons increases. We believe that in $Gd_5Si_{3.62}Sb_{0.38}$ an expected increase in the Curie temperature induced by a larger conduction electron concentration is offset by larger Gd-Gd distances. While there are no atomic parameters for $Gd_5Si_{3.62}Sb_{0.38}$, a larger volume of the Gd_5Si_4-type phase in $Gd_5Si_{3.62}Sb_{0.38}$ as compared with pure Gd_5Si_4 (861 vs. 855 $Å^3$)[16] suggests increased Gd-Gd distances.

6.4.6 Magnetocaloric effect in $Gd_5Si_2Sb_2$, $Gd_5Si_{1.5}Sb_{2.5}$ and Gd_5SiSb_3

MCE in terms of the isothermal entropy change, ΔS, was calculated from the magnetization data (Figure 6.8, on the left, data for the Gd_5SiSb_3 sample is shown) through the numerical integration of the Maxwell equation.[42,38]

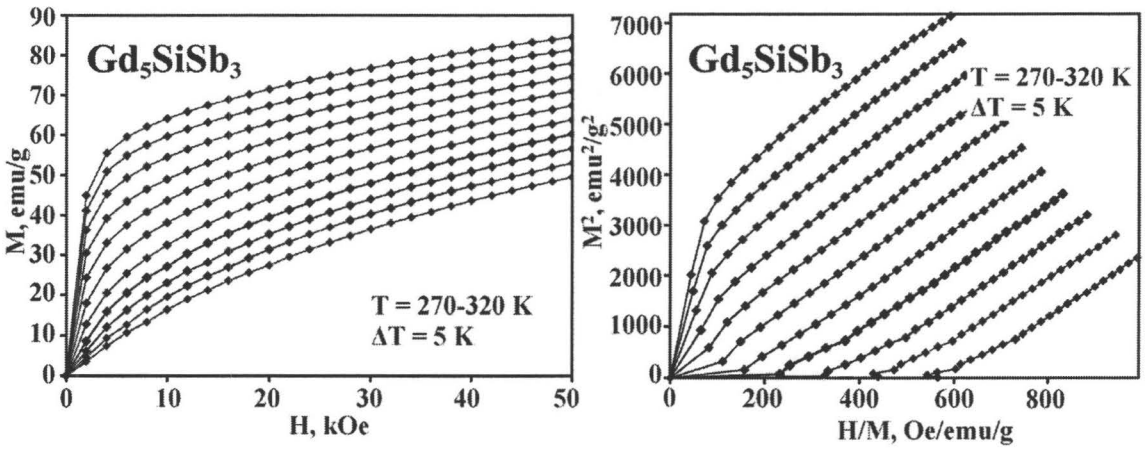

Figure 6.8. Saturation magnetization (left) and corresponding Arrott plot (right) for the Gd_5SiSb_3 sample

The maximum observed values of ΔS for the $Gd_5Si_2Sb_2$, $Gd_5Si_{1.5}Sb_{2.5}$ and Gd_5SiSb_3 samples are -3.7(4), -4.2(6) and -4.6(7) J/kg K around their Curie temperatures, respectively (Figure 6.9). The standard deviations were calculated using the method described in Ref. [43]. The ΔS values are low when compared to –36 J/kg K for $Gd_5Si_2Ge_2$[44] and point to the presence of the conventional MCE only, i.e. the magnetic ordering is not coupled to a first-order structural transition. This conclusion is supported by the behavior of Arrott plots (M^2 vs. H/M) for $Gd_5Si_2Sb_2$, $Gd_5Si_{1.5}Sb_{2.5}$ and Gd_5SiSb_3 (Figure 6.8, on the right). Absence of S-shape curves indicates second-order magnetic

transitions for all three phases. Also, the broad maxima in the ΔS vs. T curves may imply the

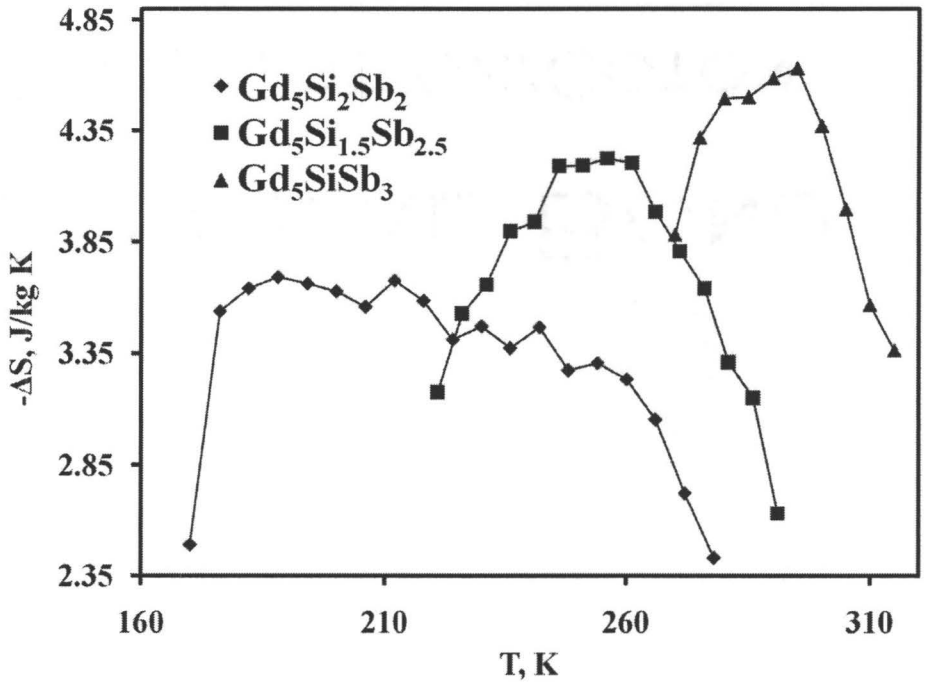

Figure 6.9. Entropy change for the $Gd_5Si_2Sb_2$, $Gd_5Si_{1.5}Sb_{2.5}$ and Gd_5SiSb_3 samples around their Curie temperatures

presence of second-order transitions only, but other factors (such as sample crystallinity and compositional homogeneity) can contribute to the broadening as well.

6.5 Conclusions

The $Gd_5Si_{4-x}Sb_x$ phases with a low Sb amount ($x \leq 0.38$) crystallizes in the Gd_5Si_4-type structure. Higher Sb levels ($1.21 \leq x \leq 3.1$) result in the cleavage of the interslab *T*-*T* dimers and appearance of the Sm_5Ge_4- and Eu_5As_4-types structures. While a larger size of the Sb atoms contributes to the dimer stretching, the main driving force for

the structural transitions is an increase in the valence electron count and a larger population of the antibonding states within the interslab *T*-*T* dimers. The $Gd_5Si_{4-x}Sb_x$ phases order ferromagnetically in the 164-336 K temperature region. While the Curie temperatures show no clear dependence on the Sb amount, it correlates well with the conduction electron concentration which is a function both of the interslab *T*-*T* bonding and Sb amount. From the Arrott plots, the magnetic transitions for the $Gd_5Si_2Sb_2$, $Gd_5Si_{1.5}Sb_{2.5}$ and Gd_5SiSb_3 samples were found to be second order. The respective ΔS values of -3.7(4), -4.2(6) and -4.6(7) J/kg K are relatively small and indicative of conventional magnetocaloric effects.

6.6 Acknowledgements

This work was supported by a Discovery Grant from the Natural Sciences and Engineering Research Council of Canada and by an Early Research Award from the Ontario Ministry of Research and Innovation.

References

[1] M. McCoy, *Chem. Eng. News* **2009**, *87*, 24-25.

[2] C. Zimm e. al., *Adv. Cryog. Eng.* **1998**, *43*, 1759-1766.

[3] V. K. Pecharsky, K. A. Gschneidner Jr., A. O. Pecharsky, A. M. Tishin, *Phys. Rev. B: Condens. Matter Mater. Phys.* **2001**, *64*, 144406/1-144406/13.

[4] V. K. Pecharsky, K. A. Gschneidner Jr., *Phys. Rev. Lett.* **1997**, *78*, 4494-4497.

[5] V. K. Pecharsky, K. A. Gschneidner Jr., *J. Magn. Magn. Mater.* **1997**, *167*, L179-L184.

[6] V. K. Pecharsky, K. A. Gschneidner Jr., *Appl. Phys. Lett.* **1997**, *70*, 3299-3301.

[7] A. O. Pecharsky, K. A. Gschneidner, V. K. Pecharsky, *J. Magn. Magn. Mater.* **2003**, *267*, 60-68.

[8] V. K. Pecharsky, K. A. Gschneidner Jr., *Adv. Cryog. Eng.* **1998**, *43*, 1729-1736.

[9] O. Tegus, E. Brick, K. H. J. Buschow, F. R. de Boer, *Nature* (London, U. K.) **2002**, *415*, 150-152.

[10] M.-K. Han, G. J. Miller, *Inorg. Chem.* **2008**, *47*, 515-528.

[11] E. Brueck, O. Tegus, D. T. Cam Thanh, N. T. Trung, K. H. J. Buschow, *Int. J. Refrig.* **2008**, *31*, 763-770.

[12] N. K. Singh, K.G. Suresh, A.K. Nigam, S.K. Malik, A.A. Coelho, S. Gama, *J. Magn. Magn. Mater.* **2007**, *317*, 68-79.

[13] J. Herrero-Albillos, F. Bartolomé, L. M. García, F. Casanova, A. Labarta, X. Batlle, *Phys. Rev. B* **2006**, *73*, 134410.

[14] W. Choe, V. K. Pecharsky, A. O. Pecharsky, K. A. Gschneidner, Jr.; V. G. Young Jr., G. J. Miller, *Phys. Rev. Lett.* **2000**, *84*, 4617-4620.

[15] V. K. Pecharsky, K. A. Gschneidner, *J. Alloys Compd.* **1997**, *260*, 98–106.

[16] V. Svitlyk, G. J. Miller, Y. Mozharivskyj, *J. Am. Chem. Soc.* **2009**, *131*, 2367-2374.

[17] Y. Mozharivskyj, W. Choe, A. O. Pecharsky, G. J. Miller, *J. Am. Chem. Soc.* **2003**, *125*, 15183-15190.

[18] L. -M. Wu, S. -H. Kim, D. -K. Seo, *J Am. Chem. Soc.* **2005**, *127*, 15682-3.

[19] Y. Mozharivskyj, A. O. Tsokol, G. J. Miller, *Z. Kristallogr.* **2006**, *221*, 493-501.

[20] R. T. Sanderson, *J. Am. Chem. Soc.* **1983**, *105*, 2259-61.

[21] R. Nirmala, A. V. Morozkin, S. K. Malik, *Europhys. Lett.* **2005**, *72*, 652-657.

[22] A. V. Morozkin, *J. Alloys Compd.* **2003**, *358*, L6-L8.

[23] A. Y. Kozlov, V. V. Pavlyuk, V. M. Davydov, *Intermetallics* **2004**, *12*, 151-155.

[24] J. Rodriguez-Carvajal, *IUCr Newsletter* **2001**, *26*, 12-19.

[25] *STOE & Cie GmbH*, Darmstadt: Germany. **2004**.

[26] G. M. Sheldrick, *SHELXL97 and SHELXS97*; University of Gottingen: Germany, **1997**.

[27] O. K. Anderson, *Phys. Rev. B* **1986**, *34*, 2439.

[28] O. Jepsen, A. Burkhardt, O. K. Anderson, *The TB-LMTO-ASA Program, Version 4.7, Max-Planck-Institut für Festkörperforschung*; Stuttgart: Germany, **1999**.

[29] J. Le Roy, J. M. Moreau, D. Paccard, E. Parthe, *Acta Crystallogr. B* **1978**, *B34*, 3315–3318.

[30] F. Holtzberg, R. J. Gambino, T. R. McGuire, *J. Phys. Chem. Solids* **1967**, *28*, 2283–2289.

[31] V. Svitlyk, B. J. Campbell, Y. Mozharivskyj, *Inorg. Chem.* (Washington, DC, U. S.) **2009**, *48*, 10364-10370.

[32] L. Pauling, *J. Am. Chem. Soc.* **2002**, *69*, 542-553.

[33] F. Holtzberg, R. J. Gambino, T. R. McGuire, *J. Phys. Chem. Solids* **1967**, *28*, 2283-9.

[34] V. Svitlyk, F. Fei, Y. Mozharivskyj, *J. Solid State Chem.* **2008**, *181*, 1080-1086.

[35] B. N. Harmon, A. J. Freeman, *Phys. Rev. B* **1974**, *10*, 1979-93.

[36] G. Czjzek, V. Oestreich, H. Schmidt, K. Latka; K. Tomala, *J. Magn. Magn. Mater.* **1989**, *79*, 42-56.

[37] L. W. Roeland, G. J. Cock, F. A. Muller, A. C. Moleman, K. A. McEwen, R. G. Jordan, D. W. Jones, *J. Phys. F* **1975**, *5*, L233-L237.

[38] V. Svitlyk, Y. Mozharivskyj, *Solid State Sci.* **2009**, *11*, 1941–1944.

[39] T. Kasuya, *Prog. Theor. Phys.* **1956**, *16*, 45.

[40] M. A. Ruderman, C. Kittel, *Phys. Rev.* **1954**, *96*, 99-102.

[41] K. Yosida, *Phys. Rev.* **1957**, *106*, 893-898.

[42] A. M. Tishin; Y. L. Spichkin, *The Magnetocaloric Effect and Its Applications, Institute of Physics Publishing, Bristol and Philadelphia.* **2003** 480 p.

[43] V. K. Pecharsky, K. A. Gschneidner Jr., *J. Appl. Phys.* **1999**, *86*, 565-575.

[44] A. O. Pecharsky, K. A. Gschneidner, V. K. Pecharsky, *J. Appl. Phys.* **2003**, *93*, 4722-4728.

Chapter 7. Appendix

7.1 $Gd_5Ni_{0.96}Sb_{2.04}$ and $Gd_5Ni_{0.71}Bi_{2.29}$: Crystal structure, magnetic properties and magnetocaloric effect. Structural transformation and magnetic properties of hexagonal Gd_5Bi_3

This section contains the manuscript "$Gd_5Ni_{0.96}Sb_{2.04}$ and $Gd_5Ni_{0.71}Bi_{2.29}$: Crystal structure, magnetic properties and magnetocaloric effect. Structural transformation and magnetic properties of hexagonal Gd_5Bi_3", published in the Journal of Solid State Chemistry (*J. Solid State Chem.* **2008**, *181*, 1080-1086). The candidate completed the experimental synthesis, data collection, processing and interpretation and prepared the manuscript. An undergraduate summer student, F. Fei, was involved in the experimental synthesis, data collection, processing and interpretation.

$Gd_5Ni_{0.96}Sb_{2.04}$ and $Gd_5Ni_{0.71}Bi_{2.29}$: Crystal structure, magnetic properties and magnetocaloric effect. Structural transformation and magnetic properties of hexagonal Gd_5Bi_3

Volodymyr Svitlyk, Fan Fei, Yurij Mozharivskyj

Department of Chemistry, McMaster University, ABB 423, 1280 Main Street west, Hamilton, Ontario, Canada, L8S 4M1

7.1.1 Abstract

Nickel was successfully introduced into the Gd_5Sb_3 and Gd_5Bi_3 binaries to yield the $Gd_5Ni_{0.96(1)}Sb_{2.04(1)}$ and $Gd_5Ni_{0.71(1)}Bi_{2.29(1)}$ phases. Both Ni-substituted compounds adopt the orthorhombic Yb_5Sb_3-type structure. While the $Gd_5Ni_{0.71}Bi_{2.29}$ phase is thermodynamically stable at 800 °C and decomposes at lower temperatures upon annealing, it can be easily quenched to room temperature by rapid cooling from 800 °C. The $Gd_5Ni_{0.96}Sb_{2.04}$ phase is found to be thermodynamically stable till room temperature. Through annealing at different temperatures, Gd_5Bi_3 was proven to undergo the Mn_5Si_3-type (LT) ↔ Yb_5Sb_3-type (HT) transformation reversibly, whereas Gd_5Sb_3 was found to adopt only the hexagonal Mn_5Si_3-type structure. Orthorhombic $Gd_5Ni_{0.96}Sb_{2.04}$ and $Gd_5Ni_{0.71}Bi_{2.29}$ and low-temperature hexagonal Gd_5Bi_3 order ferromagnetically at 115, 162 and 112 K, respectively. In Gd_5Bi_3, the ferromagnetic ordering is followed by spin reorientation below 64 K. Magnetocaloric effect in terms of ΔS was evaluated from the magnetization data and found to reach the maximum values of -7.7 J/kgK for $Gd_5Ni_{0.96}Sb_{2.04}$ and - 5.6 J/kgK for $Gd_5Ni_{0.71}Bi_{2.29}$ around their Curie temperatures.

7.1.2 Introduction

Discovery of the giant magnetocaloric effect in $Gd_5Si_2Ge_2$ and related phases[1,2] showed that cooling efficiency of a ferromagnetic material increases significantly if a ferromagnetic ordering is coupled to a first-order structural transition. For such materials, the total entropy change, ΔS, can be divided in two parts: ΔS_{mag} and ΔS_{str} associated with the magnetic and structural transitions, respectively. While it is difficult to introduce and control structural transformations and associated with them ΔS_{str} in inorganic solid-state materials, it is possible to optimize the magnetic entropy part, ΔS_{mag}. In general, large ΔS_{mag} is associated with metal-rich phases, consisting of magnetically active 3*d*- or 4*f*-elements. Besides, the 4*f*-elements are likely to yield a larger ΔS_{mag} as the maximum entropy change during the ferromagnetic ordering depends on the total quantum number through $\Delta S_{mag} = R\ln(2J+1)$.[3] Driven by this argument, we initiated exploration of structural and magnetic properties of the Ni-substituted Gd_5Sb_3 and Gd_5Bi_3 phases. The study was also inspired, in part, by the fact that the structurally related Y_5Sb_3 phase and its derivative $Y_5Ni_xSb_{3-x}$ were found to undergo a first-order orthorhombic-to-hexagonal structural transition at elevated temperatures.[4]

Similar to Y_5Sb_3, Gd_5Bi_3 was found to adopt two structural modifications.[5] The stoichiometric Gd_5Bi_3 phase was believed to adopt a hexagonal Mn_5Si_3-type structure, while a Gd-richer phase, $Gd_{5+x}Bi_3$, was suggested for the orthorhombic Yb_5Sb_3-type polymorph.[5] No other literature data were found to substantiate existence of $Gd_{5+x}Bi_3$, instead recent results by Szade and Drzyzga[6] indicated that a Yb_5Sb_3-type structure is adopted by stoichiometric Gd_5Bi_3 at higher temperatures. This high-temperature

modification was found to exhibit a ferromagnetic-like transition at 110 K, followed by spin reorientation or freezing below 60 K.[6] The magnetic behavior of the low-temperature hexagonal Gd_5Bi_3 polymorph was not studied. In contrast to Gd_5Bi_3, only a hexagonal Mn_5Si_3-type phase has been reported for Gd_5Sb_3.[7] This hexagonal Gd_5Sb_3 phase orders ferromagnetically at 187 K and then undergoes a possible ferrimagnetic transition below 50 K.[8] Presence of structural and/or magnetic transitions in Gd_5Sb_3 and Gd_5Bi_3 was another motivation for us to explore the properties of the Ni-substituted phases. Here we report on the structural features and magnetocaloric effect of these phases.

7.1.3 Experimental

7.1.3.1 Synthesis and X-ray structure analysis

The starting materials were Gd (99.9%, CERAC Incorporation), Ni (99.93% Alfa Aesar), Bi (99.9999%, CERAC Incorporation) and antimony (99.999%, CERAC Incorporation). The samples with initial compositions Gd_5Sb_3, Gd_5Bi_3, Gd_5NiSb_2 and Gd_5NiBi_2 and a total mass of 1 g were arc melted in argon atmosphere, then turned over and remelted to achieve homogeneity. Two milligrams of Sb or Bi was added extra to the samples to compensate for losses during melting. For annealing at 800 °C and lower temperatures, the samples were sealed in evacuated silica tubes, kept at the required temperature for 1 or 2 weeks and then quenched in cold water. For annealing at 1350 °C, the samples were sealed in tantalum tubes with argon inside and heated in dynamic vacuum (10^{-6} Torr) in an induction furnace.

Phase composition and lattice constants of the prepared samples (Table 7.1.1) were determined from the X-ray powder diffraction patterns recorded on a Huber image plate Guinier camera with the Cu$K\alpha_1$ radiation. The lattice constants were derived through a full-profile Rietveld analysis using the Rietica software.[9]

Table 7.1.1. Crystal data for the phases annealed at 800 and 1350 °C

Phase	Annealing temperature (°C)	Structure. type	Space group	Lattice constants, Å
Gd_5Sb_3	800°C	Mn_5Si_3	*P6₃/mcm*	$a = 9.0243(1)$, $c = 6.3241(1)$
$Gd_5Ni_{0.96}Sb_{2.04}$	800°C	Yb_5Sb_3	*Pnma*	$a = 12.133(1)$, $b = 8.9528(8)$, $c = 7.9561(8)$
Gd_5Bi_3	800°C	Mn_5Si_3	*P6₃/mcm*	$a = 9.1842(7)$, $c = 6.4177(8)$
Gd_5Bi_3	1350°C	Yb_5Sb_3	*Pnma*	$a = 12.106(1)$, $b = 9.549(1)$, $c = 8.261(1)$
$Gd_5Ni_{0.71}Bi_{2.29}$	800°C	Yb_5Sb_3	*Pnma*	$a = 12.230(1)$, $b = 9.222(1)$, $c = 8.102(1)$

Single crystal studies were performed on a STOE IPDS II diffractometer with the Mo$K\alpha$ radiation. Small crystals with a shape of rectangular plates and silver luster were picked up from the Gd_5NiSb_2 and Gd_5NiBi_2 samples annealed at 800 °C for 2 weeks. The diffraction data were collected in the whole reciprocal sphere. Using the SHELXL program,[10] the compositions were refined to $Gd_5Ni_{0.96(1)}Sb_{2.04(1)}$ and $Gd_5Ni_{0.71(1)}Bi_{2.29(1)}$ for the Gd_5NiSb_2 and Gd_5NiBi_2 samples, respectively (Tables 7.1.2 and 7.1.3). While during the refinements Ni was found to occupy the 4*c* site, we also check for the Ni presence on the 8*d* Sb1 or Bi1 site by refining their occupancies (Ni presence would lead to a lower electron density and thus lower occupancies for the pure Sb1/Bi sites). The refined occupancies were 0.993(3) for the 8*d* Sb1 site in $Gd_5Ni_{0.96(1)}Sb_{2.04(1)}$ and 0.995(6)

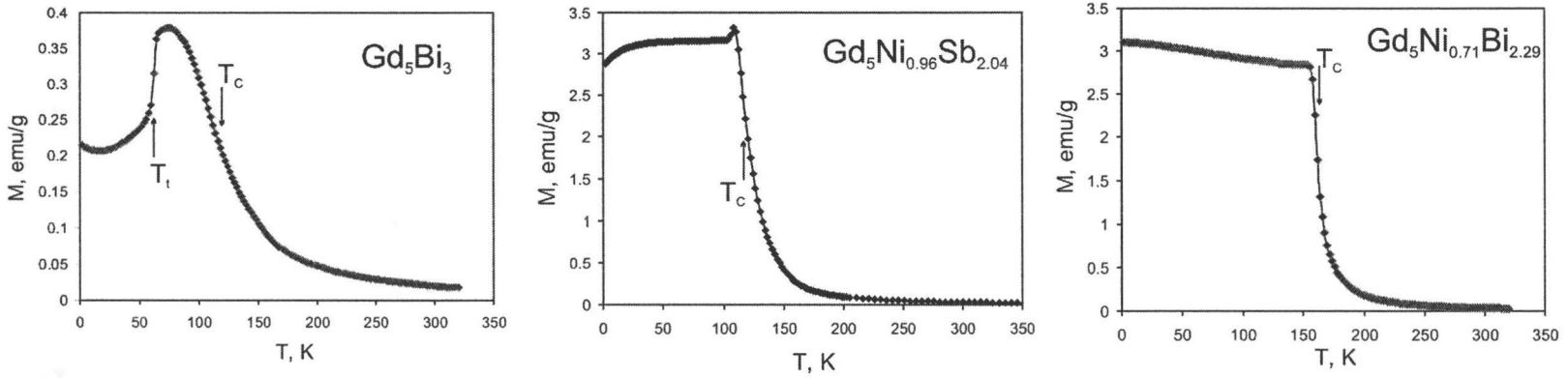

Figure 7.1.1. Magnetization as a function of temperature at $H = 100$ Oe for hexagonal Gd_5Bi_3 and orthorhombic $Gd_5Ni_{0.96}Sb_{2.04}$ and $Gd_5Ni_{0.71}Bi_{2.29}$

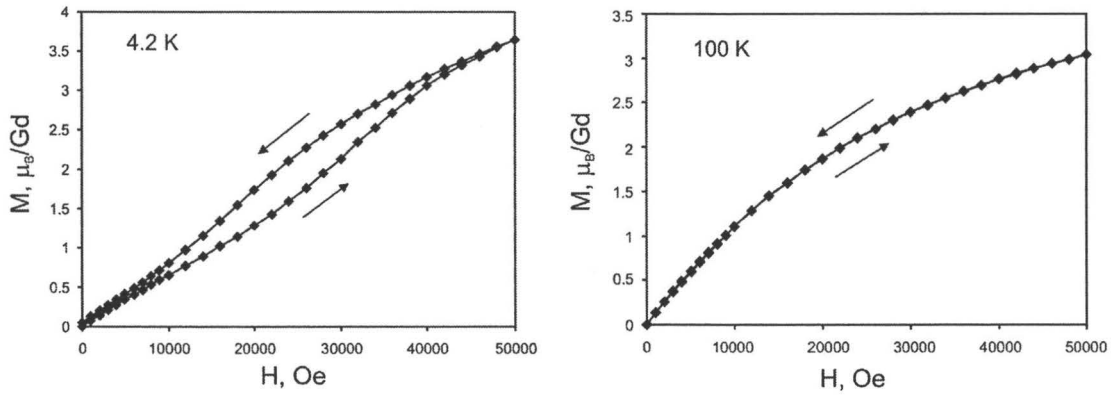

Figure 7.1.2. Magnetization as a function of field for hexagonal Gd_5Bi_3 at 4.2 K and 100 K

for the 8*d* Bi1 site $Gd_5Ni_{0.71(1)}Bi_{2.29(1)}$. The occupancies are close to one within three standard deviations and thus the corresponding 8*d* site can be assumed to be fully occupied by Sb or Bi.

Table 7.1.2. Crystal data and structure refinements for $Gd_5Ni_{0.96(1)}Sb_{2.04(1)}$ and $Gd_5Ni_{0.71(1)}Bi_{2.29(1)}$ at 293 K, Mo$K\alpha_1$ radiation, STOE IPDS II diffractometer

Composition	$Gd_5Ni_{0.96(1)}Sb_{2.04(1)}$	$Gd_5Ni_{0.71(1)}Bi_{2.29(1)}$
Space group	*Pnma*	*Pnma*
Lattice parameters (Å)	a = 12.136(1)	a = 12.228(2)
	b = 8.9472(7)	b = 9.241(1)
	c = 7.9546(7)	c = 8.137(1)
Volume (Å^3)	863.7(3)	919.5(3)
Z	4	4
Density (calculated) (g/cm^3)	8.389	9.665
Crystal size (mm^3)	0.017 x 0.054 x 0.079	0.009 x 0.046 x 0.065
2θ range for data collection	6.12-58.22°	6.02-58.28°
Index ranges	$-16 \le h \le 16$, $-12 \le k \le 11$,	$-16 \le h \le 16$, $-12 \le k \le 12$,
	$-0 \le l \le 10$	$-11 \le l \le 11$
Reflections collected	8646	8898
Independent reflections	1227 [R_{int} = 0.0603]	1306 [R_{int} = 0.2325]
Completness to max 2θ (%)	99.5	99.5
Data/restrains/parameters	1227/0/45	1306/0/45
Goodness-of-fit on F^2	0.812	0.699
Final R indices	R_1 = 0.0286	R_1 = 0.0479
[$I>2\sigma(I)$]	wR_2 = 0.0335	wR_2 = 0.0547
R indices	R_1 = 0.0375	R_1 = 0.0727
(all data)	wR_2 = 0.0522	wR_2 = 0.1345
Extinction coefficient	0.00054(3)	0.00013(2)
Largest diff. peak/hole, (e/Å^3)	1.60/-2.18	2.93/-4.30

Further details of the crystal structure investigations can be obtained from the Fachinformationszentrum Karlsruhe, 76344 Eggenstein-Leopoldshafen, Germany, (fax: +49 7247 808 666; e-mail: crysdata@fiz.karlsruhe.de) on quoting the depository CSD

number 418769 for $Gd_5Ni_{0.96(1)}Sb_{2.04(1)}$ and 418770 for $Gd_5Ni_{0.71(1)}Bi_{2.29(1)}$ and also from the supporting information.

7.1.3.2 Magnetic measurements

Magnetization for the field cooled (FC) polycrystalline pieces of hexagonal Gd_5Bi_3, orthorhombic $Gd_5Ni_{0.96}Sb_{2.04}$ and $Gd_5Ni_{0.71}Bi_{2.29}$ phases (all annealed at 800 °C) was measured at 100 Oe field between 2 and 320 K (350 K for $Gd_5Ni_{0.96}Sb_{2.04}$ compound) on a Quantum Design SQUID magnetometer (Fig. 7.1.1).

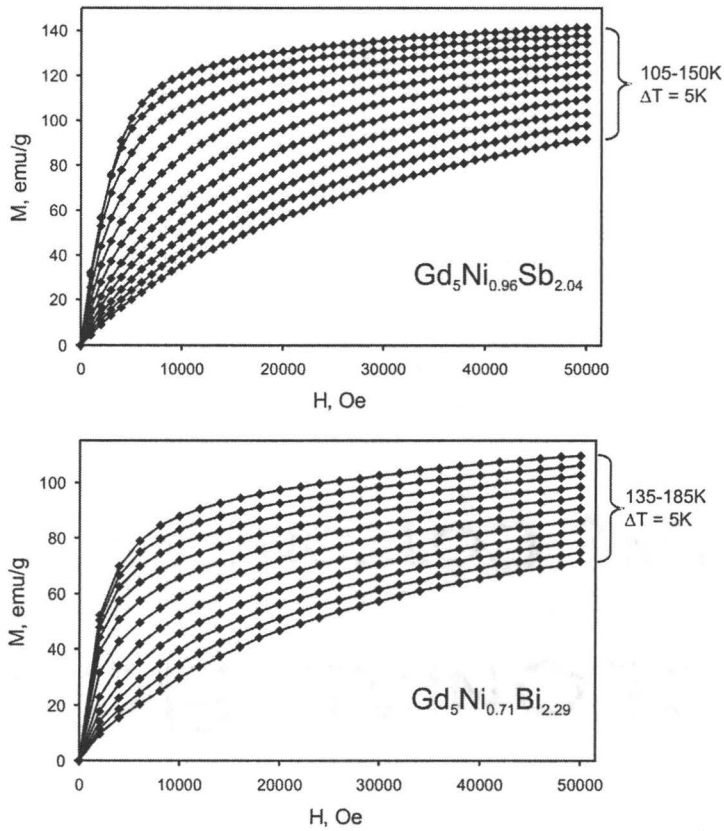

Figure 7.1.3. Magnetization versus field curves for orthorhombic $Gd_5Ni_{0.96}Sb_{2.04}$ and $Gd_5Ni_{0.71}Bi_{2.29}$

The transition temperatures were derived from the $\delta M/\delta T$ vs. T plots and correspond to the maxima in these plots. To explore the nature of the magnetic ordering in hexagonal Gd_5Bi_3, magnetization curves were measured at 4.2 and 100 K in increasing and decreasing magnetic fields (Fig. 7.1.2).

Magnetocaloric effect for $Gd_5Ni_{0.96}Sb_{2.04}$ and $Gd_5Ni_{0.71}Bi_{2.29}$ was evaluated from the magnetization data. For this purpose, a series of magnetization versus magnetic field (M vs. H) measurements was done around the ordering temperature with 5 K increments (Fig. 7.1.3). The magnetic field changed from 0 to 50,000 Oe with a 1000 and 2000 Oe step for $Gd_5Ni_{0.96}Sb_{2.04}$ and $Gd_5Ni_{0.71}Bi_{2.29}$, respectively.

7.1.4 Results and discussion

7.1.4.1 Thermal stability and structures of Gd_5Sb_3, Gd_5Bi_3, $Gd_5Ni_{0.96}Sb_{2.04}$ and $Gd_5Ni_{0.71}Bi_{2.29}$

Temperature stability of Gd_5Sb_3, Gd_5Bi_3, $Gd_5Ni_{0.96}Sb_{2.04}$ and $Gd_5Ni_{0.71}Bi_{2.29}$ is summarized in Fig. 7.1.4 (see also Table 7.1.1). From the initial annealing at 800 °C, both Gd_5Sb_3 and Gd_5Bi_3 were found to adopt the hexagonal Mn_5Si_3-type structure at 800 °C, while $Gd_5Ni_{0.96}Sb_{2.04}$ and $Gd_5Ni_{0.71}Bi_{2.29}$ were found to crystallize in the orthorhombic Yb_5Sb_3-type structure at 800 °C. Since hexagonal Mn_5Si_3-type and orthorhombic Yb_5Sb_3-type structures have been identified as low-temperature (LT) and high-temperature (HT) forms, respectively, for Y_5Sb_3,[4] the same could be assumed for Gd_5Sb_3 and Gd_5Bi_3. Also based on the literature data for Gd_5Bi_3,[5,6] it could be hypothesized that the same structural sequence is followed by Gd_5Bi_3, but this was never rigorously proven. To check for the

existence of the HT Yb_5Sb_3-type polymorphs, the two binaries Gd_5Sb_3 and Gd_5Bi_3, annealed at 800 °C, were sealed in tantalum tubes and annealed at 1350 °C in dynamic vacuum. After annealing at 1350 °C for 1.5 h, Gd_5Bi_3 showed complete transformation from the Mn_5Si_3- type polymorph into the Yb_5Sb_3-type one. If Gd_5Bi_3 treated at 1350 °C is annealed again at 800 °C for 2 weeks, it transforms back into the hexagonal polymorphs, proving that the Mn_5Si_3-type ↔ Yb_5Sb_3-type transformation is fully reversible. On the other hand, Gd_5Sb_3 showed no signs of structural rearrangements even after 6 h at 1350 °C, thus indicating that the orthorhombic structure is not accessible for Gd_5Sb_3 at least at this temperature. Annealing of the Gd_5Sb_3 and Gd_5Bi_3 samples at 600 and 400 °C produced the same phases as annealing at 800 °C.

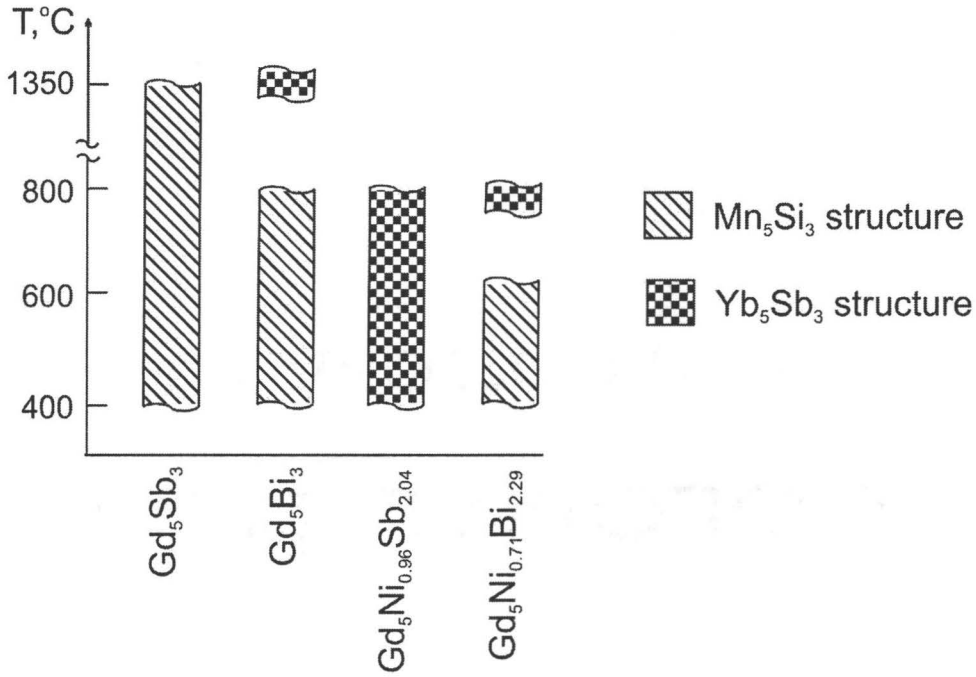

Figure 7.1.4. Schematic phase diagram for Gd_5Sb_3, Gd_5Bi_3, $Gd_5Ni_{0.96}Sb_{2.04}$ and $Gd_5Ni_{0.71}Bi_{2.29}$

The "A_5Pn_3" pnictides (A = a divalent electropositive atom such as Ca, Sr, Ba, Sm, Eu, Yb, Pn = Sb, Bi) with the Yb_5Sb_3-type structure have been shown to be, in reality, hydrogen-stabilized A_5Pn_3H phases, with hydrogen coming from the commercial A metals.[11,12] As Ta becomes relatively transparent to H_2 above 550 °C, annealing under the dynamic vacuum at higher temperatures dehydrogenates the samples and results in the formation of the hexagonal A_5Pn_3 phases (the Mn_5Si_3-type).[11]

Table 7.1.3. Atomic and isotropic temperature (U) parameters for $Gd_5Ni_{0.96(1)}Sb_{2.04(1)}$ and $Gd_5Ni_{0.71(1)}Bi_{2.29(1)}$ from single crystal diffraction data

Atom		Occupancy	*x/a*	*y/b*	*z/c*	U (Å^2)
$Gd_5Ni_{0.96(1)}Sb_{2.04(1)}$						
Gd1	4*c*	1	0.2907(1)	1/4	0.6576(1)	0.010(1)
Gd2	4*c*	1	0.1991(1)	1/4	0.1299(1)	0.010(1)
Gd3	4*c*	1	0.5005(1)	1/4	0.9609(1)	0.010(1)
Gd4	8*d*	1	0.4338(1)	0.0390(1)	0.3156(1)	0.011(1)
Sb1	8*d*	1	0.3269(1)	0.9926(1)	0.9277(1)	0.009(1)
Sb2/Ni	4*c*	0.04/0.96(1)	0.5148(1)	1/4	0.5775(2)	0.012(1)
$Gd_5Ni_{0.71(1)}Bi_{2.29(1)}$						
Gd1	4*c*	1	0.2880(2)	1/4	0.6622(2)	0.019(1)
Gd2	4*c*	1	0.2025(2)	1/4	0.1331(3)	0.021(1)
Gd3	4*c*	1	0.4986(2)	1/4	0.9646(2)	0.016(1)
Gd4	8*d*	1	0.4352(1)	0.0446(2)	0.3165(2)	0.025(1)
Bi1	8*d*	1	0.3264(1)	0.9906(1)	0.9274(1)	0.014(1)
Bi2/Ni	4*c*	0.29/0.71(1)	0.0215(2)	1/4	0.9119(3)	0.015(1)

While hydrogen presence is proven to be an important factor in the chemistry of pnictides with a divalent metal, A, its role in the stability of analogous pnictides with a trivalent rare-earth elements, RE, is not fully understood. Even if hydrogen tends to stabilize the

RE_5Pn_3 pnictides, the conditions of our experiment (1350 °C and dynamic vacuum) are expected to dehydrogenate and, thus, preclude hydrogen stabilization of the high-temperature form of Gd_5Bi_3 and also of the hexagonal Gd_5Sb_3 phase.

The compositions $Gd_5Ni_{0.96(1)}Sb_{2.04(1)}$ and $Gd_5Ni_{0.71(1)}Bi_{2.29(1)}$ obtained from the single crystal refinements were Ni poorer than the initial ones used for the synthesis, therefore it was assumed that the Ni amounts in these phases were the largest ones accessible under our experimental conditions. Thermal stability of the $Gd_5Ni_{0.96}Sb_{2.04}$ and $Gd_5Ni_{0.71}Bi_{2.29}$ phases was studied through annealing at 600 °C for 1 week, followed by annealing at 400 °C for 2 weeks. At 600 and 400 °C, $Gd_5Ni_{0.71}Bi_{2.29}$ was found to decompose into the hexagonal binary Gd_5Bi_3 and an unidentified Ni-containing phase. The lattice constants of the obtained Gd_5Bi_3 binary were in good agreement with those of the pristine Gd_5Bi_3 sample, thus indicating that there was no nickel left in the resulting Gd_5Bi_3 binary. We could not find suitable single crystals of hexagonal Gd_5Bi_3 to confirm that no nickel is present. In contrast, $Gd_5Ni_{0.96}Sb_{2.04}$ showed no signs of a structural transformation/decomposition at either 600 °C or 400 °C. While $Gd_5Ni_{0.96}Sb_{2.04}$ may still undergo a phase transition at lower temperatures, this could require a very long annealing time as the atomic rearrangements associated with this transition are very significant (see the discussion below).

In addition to $Gd_5Ni_{0.96}Sb_{2.04}$, and $Gd_5Ni_{0.71}Bi_{2.29}$ reported here, the orthorhombic Yb_5Sb_3-type structure is observed for other transition-metal substituted $RE_5T_xSb_{3-x}$ and $RE_5T_xBi_{3-x}$ phases annealed at 830 °C (RE is a rare earth and T = Fe–Cu).[4,13] Out of all possible $RE_5T_xSb_{3-x}$ and $RE_5T_xBi_{3-x}$ phases, only few representatives and only those

without gadolinium were prepared. Besides, the thermal stability of these phases was not investigated. Based on our current studies and the literature data,[4] it can be concluded that the substitution of a late 3*d*-metal for Sb or Bi tends to stabilize the orthorhombic polymorphs of the corresponding binaries at high temperatures (exception is $Gd_5Ni_{0.96}Sb_{2.04}$). But this substitution by the transition metal is limited. The limited amount of Ni and the stability of the corresponding Ni substituted orthorhombic phase were analyzed in details for $Y_5Ni_xSb_{3-x}$.[4] It has been concluded that Ni incorporation reduces the strength of the Y–Sb interactions, which in turn limits the maximum amount of Ni in the structure. The structure can be stabilized only at high temperatures due to the entropy contribution stemming from the Ni/Sb statistical mixture. We can argue that the same is true for $Gd_5Ni_{0.96}Sb_{2.04}$ and $Gd_5Ni_{0.71}Bi_{2.29}$.

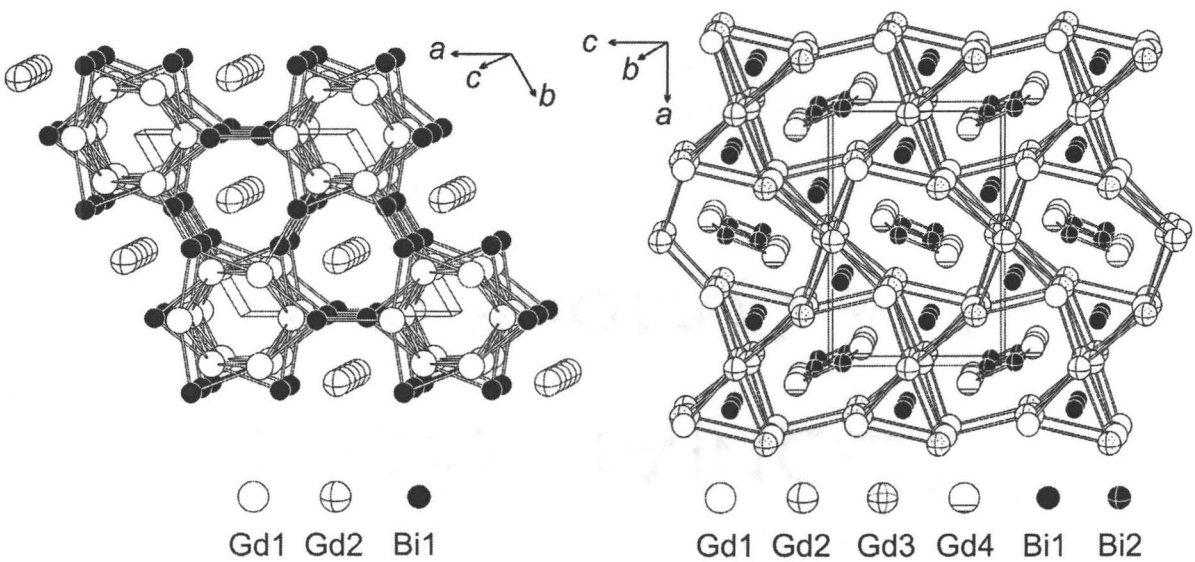

Figure 7.1.5. Structures of the hexagonal Mn_5Si_3-type (left) and orthorhombic Yb_5Sb_3-type (right) polymorphs of Gd_5Bi_3

The two structural polymorphs, the Mn_5Si_3 and Yb_5Sb_3 ones, differ significantly in terms of atomic arrangements (Fig. 7.1.5), and as pointed by Brunton and Steinfink[14] who first discovered the Yb_5Sb_3 phase, there is little resemblance between the two structure types. In the ''classical'' presentation by Guloy et al.,[15] the Mn_5Si_3-type structure of Gd_5Bi_3 is constructed from the Gd1 octahedra that are fused along the c direction to form hexagonal columns. The columns are interconnected through the Bi atoms, which in turn form channels filled with Gd2 chains. While hexagonal channels can be also identified in the Yb_5Sb_3-type structure of Gd_5Bi_3, they are irregular and filled with both Gd and Bi atoms (Fig. 7.1.5). There are also the trigonal channels filled with the Bi atoms and attached to the hexagonal ones. No simple atomic rearrangement is found to transform one structure into the other, besides the space groups of the two structures are not in a group–subgroup relationship. Such different atomic arrangements may explain the fact that the HT orthorhombic polymorphs could be easily quenched into room temperature and that a long annealing time is required to obtain a LT hexagonal polymorph.

7.1.4.2 Magnetic properties and magnetocaloric effect

The LT hexagonal polymorph of Gd_5Bi_3 exhibits a complex magnetic behavior (Fig. 7.1.1) which is analogous to that found in hexagonal Gd_5Sb_3.[8] While the overall shape of the curve may be representative of an antiferromagnetic ordering, the Weiss temperature derived from the paramagnetic region clearly indicates that interactions at higher temperatures are ferromagnetic in nature. These ferromagnetic interactions yield a

ferromagnetic ordering at 112 K, followed by a significant decrease in magnetization below 64 K which is indicative of spin reorientation. A step-like change in M vs. H at 4.2 K also points at spin reorientation at low temperatures (Fig. 7.1.2).

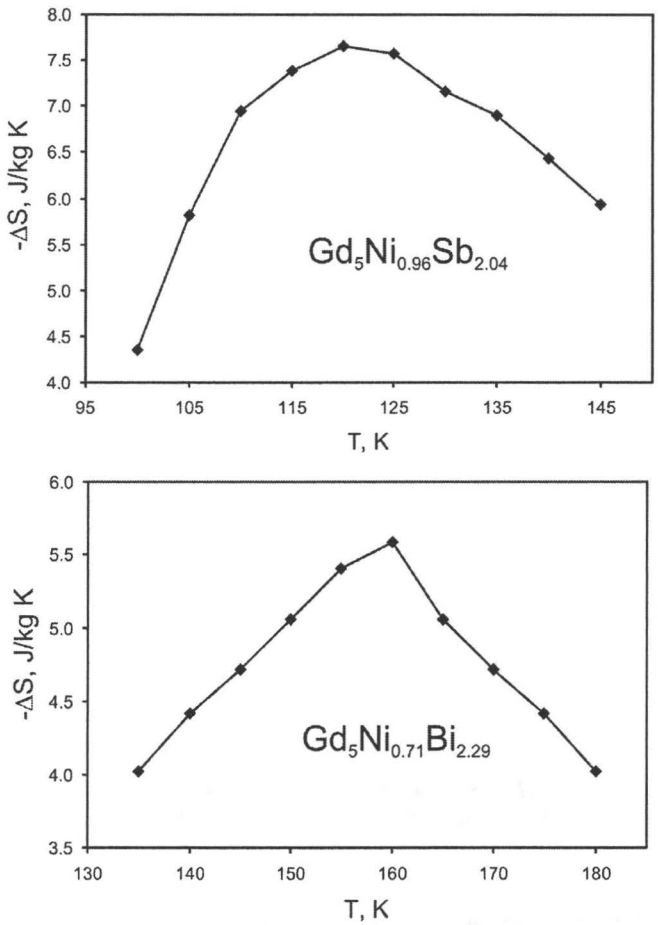

Figure 7.1.6. Entropy change for $Gd_5Ni_{0.96}Sb_{2.04}$ and $Gd_5Ni_{0.71}Bi_{2.29}$ as a function of temperature for ΔH = 0-50,000 Oe

This step-like feature is expected to be absent above 64 K, and this is verified by a M vs. H scan at 100 K. At both temperatures 4.2 and 100 K, magnetization in 50 kOe did not reach the gJ value of 7.00 μ_B expected for a Gd^{3+} free ion. Above 200 K, Gd_5Bi_3

follows the Curie–Weiss law with θ_p = 137 K and μ_{eff}/Gd = 8.57 μ_B (Table 7.1.4). For comparison, at the paramagnetic region the HT orthorhombic form of Gd_5Bi_3 obeys the Curie–Weiss law with θ_p = 120 K and μ_{eff}/Gd = 8.43 μ_B,[6] while hexagonal Gd_5Sb_3 follows the Currie–Weiss law with much larger θ_p = 267 K and μ_{eff}/Gd = 10.9 μ_B.[8]

The orthorhombic $Gd_5Ni_{0.96}Sb_{2.04}$ and $Gd_5Ni_{0.71}Bi_{2.29}$ compounds undergo ferromagnetic orderings at 115 and 162 K, respectively. Interestingly, the Currie temperature for the Ni-substituted $Gd_5Ni_{0.71}Bi_{2.29}$ is 50 K higher than that of the pure orthorhombic Gd_5Bi_3 binary. At higher temperatures, both Ni-substituted phases obey the Curie–Weiss relationship with θ_p = 161 K and μ_{eff}/Gd = 8.48 μ_B for $Gd_5Ni_{0.96}Sb_{2.04}$ and θ_p = 182 K and μ_{eff}/Gd = 9.61 μ_B $Gd_5Ni_{0.71}Bi_{2.29}$. The calculated magnetic moment for Gd in $Gd_5Ni_{0.96}Sb_{2.04}$ is similar to those observed in orthorhombic and hexagonal Gd_5Bi_3, thus suggesting that magnetic contribution of Ni atoms is small. Even if assumed otherwise, the Ni contribution would be insufficient to yield large magnetic moments observed in $Gd_5Ni_{0.96}Sb_{2.04}$ and especially in $Gd_5Ni_{0.71}Bi_{2.29}$.

Table 7.1.4. Magnetic parameters for Gd_5Sb_3, Gd_5Bi_3, $Gd_5Ni_{0.96}Sb_{2.04}$ and $Gd_5Ni_{0.71}Bi_{2.29}$

Compound	Space group	Magnetic behavior	T_C, K	$\mu_{eff/Gd}$, μ_B	Θ_p, K	$-\Delta S$, J/kg K	Ref.
Gd_5Sb_3	*P6₃/mcm*	Ferromagnetic	187	10.9	266.8		8
$Gd_5Ni_{0.96}Sb_{2.04}$	*Pnma*	Ferromagnetic	115	8.48	161	7.7[a]	this work
Gd_5Bi_3	*P6₃/mcm*	Ferromagnetic	112	8.57	137		this work
Gd_5Bi_3	*Pnma*	Ferromagnetic	110	8.43	120		6
$Gd_5Ni_{0.71}Bi_{2.29}$	*Pnma*	Ferromagnetic	162	9.61	182	5.6[a]	this work

[a] ΔS is the maximum entropy change for a magnetic field change ΔH = 0-50,000 Oe

It is also difficult to say whether the Ni presence influences the Gd moment since the phases with the same structure have to be compared. However only two Gd-containing phases, Gd_5Bi_3 and $Gd_5Ni_{0.71}Bi_{2.29}$, with the same Yb_5Sb_3-type structure are known, and thus no general conclusions can be drawn.

Magnetic moments larger than $\mu_{eff} = g[J(J+1)]^{1/2}\mu_B = 7.94\ \mu_B$ expected for a free Gd^{3+} ion are found not only in Gd_5Bi_3, Gd_5Sb_3 and their Ni derivatives, but also in other Gd-containing phases: e.g. 8.32 μ_B in $Gd_4Pd_{10}In_{21}$.[16] Even elemental Gd shows a ~9% increase for its measured magnetic moment.[17] Generally, increase in μ_{eff} /Gd is attributed to the polarization of conduction electrons, predominantly the Gd 5*d* ones, through the 4*f*–5*d* exchange interactions.[18,19]

Magnetocaloric effect in terms of entropy change, ΔS, for the Ni-substituted materials was evaluated from the magnetization data (Fig. 7.1.3) using the Maxwell relationships:[3]

$$\left(\frac{\partial S(T,H)}{\partial H}\right)_T = \left(\frac{\partial M(T,H)}{\partial T}\right)_H, \tag{7.1}$$

which after the integration yields

$$\Delta S(T)_{\Delta H} = \int_{H_1}^{H_2}\left(\frac{\partial M(T,H)}{\partial T}\right)_{H,P} dH. \tag{7.2}$$

In practice, a numerical integration is performed using the following formula:

$$\Delta S(T)_{\Delta H} = \sum_i \frac{M_i - M_{i+1}}{T_{i+1} - T_i}\delta H, \tag{7.3}$$

where δH is a magnetic field step and M_i and M_{i+1} are the values of magnetization at temperatures T_i and T_{i+1}, respectively. The magnetic entropy change, ΔS, for ΔH = 0–

50,000 Oe is plotted in Fig. 7.1.6. As expected, ΔS peaks around the Curie temperatures and has the maximum value of -7.7 J/kgK for $Gd_5Ni_{0.96}Sb_{2.04}$ and -5.6 J/kgK for $Gd_5Ni_{0.71}Bi_{2.29}$. While these values of ΔS are substantial, they are smaller (by absolute values) than -9.8 J/kgK measured for pure gadolinium or -18.5 J/kgK found for $Gd_5Si_2Ge_2$.[1]

7.1.5. Conclusion

The two binaries Gd_5Sb_3 and Gd_5Bi_3 exhibit different structural behavior with temperature. Gd_5Bi_3 adopts two polymorphs: a LT Mn_5Si_3-type one below 800 °C and a HT orthorhombic Yb_5Sb_3-type one at 1350 °C. In contrast, Gd_5Sb_3 crystallizes only with a hexagonal Mn_5Si_3-type structure and is not found to undergo any structural transition up to 1350 °C. Ni substitution leads to the formation of the orthorhombic structure for $Gd_5Ni_{0.96}Sb_{2.04}$ and stabilizes the orthorhombic bismuthide $Gd_5Ni_{0.71}Bi_{2.29}$ to lower temperatures. The magnetic behavior of orthorhombic $Gd_5Ni_{0.96}Sb_{2.04}$ and $Gd_5Ni_{0.71}Bi_{2.29}$ is similar as both phases order ferromagnetically at low temperatures. Hexagonal Gd_5Bi_3 shows a more complex magnetic behavior as the ferromagnetic ordering is followed by spin reorientation.

7.1.6. Acknowledgements

This work was supported by a Discovery Grant from the Natural Sciences and Engineering Research Council of Canada.

References

[1] V. K. Pecharsky, K. A. Gschneidner Jr., *Phys. Rev. Lett.* **1997**, *78*, 4494–4497.

[2] V. K. Pecharsky, K. A. Gschneidner Jr., *Springer Series in Materials Science* **2005**, *79*, 199–222 (Magnetism and Structure in Functional Materials).

[3] A. M. Tishin, Y. I. Spichkin, *The Magnetocaloric Effect and its Application*, Institute of Physics Publishing, Bristol and Philadelphia, **2003**.

[4] Y. Mozharivskyj, H. F. Franzen, *J. Alloys Compd.* **2001**, *319*, 100–107.

[5] K. Yoshihara, J. B. Taylor, L. D. Calvert, J. G. Despault, *J. Less-Common Metals* **1975**, *41*, 329–337.

[6] J. Szade, M. Drzyzga, *J. Alloys Compd.* **2000**, *299*, 72–78.

[7] W. Rieger, E. Parthe, *Acta Crystallogr. B* **1968**, *24*, 456–458.

[8] M. Nagai, A. Tanaka, Y. Haga, T. Tsutaoka, *J.Magn. Magn. Mater.* **2007**, *310*, 1775–1777.

[9] B. A. Hunter, C. J. Howard, *Rietica, Australian Nuclear Science and Technology Organization,* Menai, Austalia, **2000**.

[10] G. M. Sheldrick, *SHELXL97 and SHELXS97*, University of Gottingen, Germany, **1997**.

[11] E. A. Leon-Escamilla, J. D. Corbett, *J. Alloys Compd.* **1998**, *265*, 104–114.

[12] E. A. Leon-Escamilla, J. D. Corbett, *Chem. Mater.* **2006**, *18*, 4782–4792.

[13] A. V. Morozkin, R. Nirmala, S. K. Malik, *J. Alloys Compd.* **2005**, *394*, L9–L11.

[14] G. D. Brunton, H. Steinfink, *Inorg. Chem.* **1971**, *10*, 2301–2303.

[15] A. M. Guloy, A. -V. Mudring, J. D. Corbett, *Inorg. Chem.* **2003**, *42*, 6673–6681.

[16] Y. Verbovytsky, K. Latka, A. W. Pacyna, *J. Alloys Compd.* **2007**, *442*, 337–340.

[17] L. W. Roeland, G. J. Cock, F. A. Muller, A. C. Moleman, K. A. McEwen, R. G. Jordan, D. W. Jones, *J. of Phy. F: Metal Phy.* **1975**, *5*, L233–L237.

[18] B. N. Harmon, A. J. Freeman, *Phy. Rev. B: Solid State* **1974**, *10*, 1979–1993.

[19] G. Czjzek, V. Oestreich, H. Schmidt, K. Latka, K. Tomala, *J. Magn. Magn. Mater.* **1989**, *79*, 42–56.

7.2 $Dy_5Ni_{0.66}Bi_{2.34}$ and $Lu_5Ni_{0.56}Sb_{2.44}$ – Substitution derivatives with the orthorhombic Yb_5Sb_3-type structure. Magnetocaloric effect of $Dy_5Ni_{0.66}Bi_{2.34}$

This chapter contains the manuscript "$Dy_5Ni_{0.66}Bi_{2.34}$ and $Lu_5Ni_{0.56}Sb_{2.44}$ – Substitution derivatives with the orthorhombic Yb_5Sb_3-type structure. Magnetocaloric effect of $Dy_5Ni_{0.66}Bi_{2.34}$", published in the Solid State Sciences (*Solid State Sci.* **2009**, *11*, 1700–1702). The candidate completed all of the experimental synthesis, data collection, processing and interpretation and prepared the manuscript. An undergraduate summer student, F. Fei, was involved in the experimental synthesis, data collection, processing and interpretation.

$Dy_5Ni_{0.66}Bi_{2.34}$ and $Lu_5Ni_{0.56}Sb_{2.44}$ – Substitution derivatives with the orthorhombic Yb_5Sb_3-type structure. Magnetocaloric effect of $Dy_5Ni_{0.66}Bi_{2.34}$

Volodymyr Svitlyk, Fan Fei, Yurij Mozharivskyj

Department of Chemistry, McMaster University, 1280 Main Street West, Hamilton, Ontario, Canada L8S 4M1

7.2.1 Abstract

$Dy_5Ni_{0.66}Bi_{2.34}$ and $Lu_5Ni_{0.56}Sb_{2.44}$ were synthesized by arc-melting and were found to adopt an orthorhombic Yb_5Sb_3-type structure. Cell parameters are a = 12.075(2), b = 9.165(2), c = 8.072(1) Å for $Dy_5Ni_{0.66}Bi_{2.34}$ and a = 11.6187(9), b = 8.933(1) and c = 7.8377(6) Å for $Lu_5Ni_{0.56}Sb_{2.44}$. $Dy_5Ni_{0.66}Bi_{2.34}$ undergoes a step-like ferromagnetic transition around 66 K. Magnetocaloric effect in terms of the magnetic entropy change, ΔS, reaches -3.73 J/kg K at 75 K for $Dy_5Ni_{0.66}Bi_{2.34}$.

7.2.2 Introduction

Research activities related to the magnetocaloric effect (MCE) and magnetocaloric phases increased dramatically after the discovery of the giant MCE in $Gd_5Si_2Ge_2$.[1] In this[2] and other phases (e.g. $LaFe_{13-x}Si_x$[3]), coupling between first-order structural and ferromagnetic transitions significantly increases the entropy change and, thus, enhances the MCE.

Chemical modification of known metal-rich, *p*-element containing phases can be used to influence electronic and magnetic interactions and can lead to structurally and/or

magnetically novel phases. Partial substitution of Ni for Sb and Bi in the Gd_5Sb_3 and Gd_5Bi_3 binary phases, which adopt the hexagonal Mn_5Si_3-type structure at 800 °C, yields orthorhombic Yb_5Sb_3-type structures for $Gd_5Ni_{0.96}Sb_{2.04}$ and $Gd_5Ni_{0.71}Bi_{2.29}$ at the same 800 °C, with a ferromagnetic ordering at 115 and 162 K, respectively.[4] A structural transition induced through a compositional variation may enhance material's magnetocaloric properties provided the transition is a temperature dependant and concomitant with the magnetic ordering. Magnetocaloric effect evaluated around Curie temperatures equals to -7.7 J/kg K for $Gd_5Ni_{0.96}Sb_{2.04}$ and -5.6 J/kg K for $Gd_5Ni_{0.71}Bi_{2.29}$ and these values are indicative of a conventional MCE.

Originally, nickel substitution was performed for the high-temperature orthorhombic modification of Y_5Sb_3 and the resulting $Y_5Ni_{0.38}Sb_{2.62}$ phase was found to be a Pauli paramagnet.[5] Similar structures were later reported for the $Gd_5Ni_xSb_{3-x}$, $Gd_5Ni_xBi_{3-x}$, $Ho_5Ni_xSb_{3-x}$ and $Ho_5Ni_xBi_{3-x}$ systems.[4,6] Ni was found to fully occupy the original Sb/Bi 4*c* sites in the Ho-containing phases, while a partial Ni substitution was established in the Gd-containing phases. Here we present structural and magnetic studies on $Dy_5Ni_{0.66}Bi_{2.34}$ and $Lu_5Ni_{0.56}Sb_{2.44}$, another two members of this series.

7.2.3 Experimental

7.2.3.1 Synthesis and X-ray structure analysis

The starting materials were Dy (99.9 wt.%, CERAC Inc.), Lu (99.9 wt.%, CERAC Inc.), Sb (99.999 wt.%, CERAC Inc.), Bi (99.9999 wt.%, CERAC Inc.) and Ni (99.9+ wt.%, Alfa Aesar). Samples with the Dy_5NiBi_2 and Lu_5NiSb_2 compositions were

arc-melted and annealed at 1350 °C for 3 h. Based on the single crystal X-ray diffraction results for the crystal extracted from annealed Dy_5NiBi_2, a sample with the $Dy_5Ni_{0.66}Bi_{2.34}$ composition was prepared by arc-melting. One half of the cast $Dy_5Ni_{0.66}Bi_{2.34}$ alloy was annealed at 1350 °C for 1.5 h, the other half was annealed at 800 °C for 2 weeks. By means of powder X-ray diffraction both samples were found to be a single phase with statistically the same lattice constants. During arc-melting, the samples were remelted four times to improve homogeneity. Two milligrams of Sb and Bi were added extra to compensate for losses.

Table 7.2.1. Crystal data and structure refinement for $Dy_5Ni_{0.66(1)}Bi_{2.34(1)}$ and $Lu_5Ni_{0.56(2)}Sb_{2.44(2)}$

Composition	$Dy_5Ni_{0.66(1)}Bi_{2.34(1)}$	$Lu_5Ni_{0.56(2)}Sb_{2.44(2)}$
Space group	*Pnma*	*Pnma*
Lattice parameters (Å)	a = 12.075(2)	a = 11.6187(9)
	b = 9.165(2)	b = 8.933(1)
	c = 8.072(1)	c = 7.8377(6)
Volume (Å^3)	893.3(2)	813.45(13)
Z	4	4
Density (calculated) (g/cm^3)	10.145	9.869
Crystal size (mm^3)	0.009 x 0.030 x 0.038	0.009 x 0.022 x 0.051
2θ range for data collection	6.08-58.50°	6.28-58.64°
Index ranges	$-16 \le h \le 16$, $-12 \le k \le 12$, $-9 \le l \le 11$	$-15 \le h \le 15$, $-12 \le k \le 10$, $-10 \le l \le 10$
Reflections collected	9480	7301
Independent reflections	1275 [R_{int} = 0.2844]	1168 [R_{int} = 0.1690]
Completeness to max 2θ (%)	98.8	98.8
Data/restraints/parameters	1275 / 0 / 45	1168 / 0 / 45
Goodness-of-fit on F^2	0.782	0.794
Final R indices [$I>2\sigma(I)$]	R_1 = 0.0621, wR_2 = 0.0644	R_1 = 0.0531, wR_2 = 0.0483
R indices (all data)	R_1 = 0.1697, wR_2 = 0.0876	R_1 = 0.1173, wR_2 = 0.0581
Extinction coefficient	0.000066(16)	0.00033(3)
Largest diff. peak/hole, (e/A^3)	3.420/-3.461	2.664/-3.286

Single crystal data for the crystals extracted from the Dy_5NiBi_2 and Lu_5NiSb_2 alloys annealed at 1350 °C for 3 h were collected on an STOE IPDS II diffractometer with the MoKα radiation in the whole reciprocal sphere. Numerical absorption correction was based on the crystal shape obtained from optical face indexing and optimized against equivalent reflections using the STOE X-Shape software.[7] The structures were solved and refined using the SHELXS and SHELXL programs,[8] respectively (Tables 7.2.1 and 7.2.2).

Table 7.2.2. Atomic and isotropic temperature (*U*) parameters for $Dy_5Ni_{0.66(1)}Bi_{2.34(1)}$ and $Lu_5Ni_{0.56(2)}Sb_{2.44(2)}$ from single crystal diffraction data

Atom	Site	Occupancy	*x/a*	*y/b*	*z/c*	*U* (Å^2)
$Dy_5Ni_{0.66(1)}Bi_{2.34(1)}$						
Dy1	4*c*	1	0.2862(2)	1/4	0.6666(4)	0.021(1)
Dy2	4*c*	1	0.2035(2)	1/4	0.1334(4)	0.023(1)
Dy3	4*c*	1	0.4978(3)	1/4	0.9645(4)	0.016(1)
Dy4	8*d*	1	0.4346(2)	0.0473(2)	0.3180(3)	0.026(1)
Bi1	8*d*	1	0.3267(1)	0.9892(1)	0.9284(2)	0.015(1)
Bi2/Ni	4*c*	0.34(1)/0.66(1)	0.5220(3)	1/4	0.5918(6)	0.017(1)
$Lu_5Ni_{0.56(2)}Sb_{2.44(2)}$						
Lu1	4*c*	1	0.2816(1)	1/4	0.6697(2)	0.017(1)
Lu2	4*c*	1	0.2060(1)	1/4	0.1381(2)	0.016(1)
Lu3	4*c*	1	0.4965(1)	1/4	0.9652(2)	0.010(1)
Lu4	8*d*	1	0.4335(1)	0.0499(1)	0.3166(1)	0.018(1)
Sb1	8*d*	1	0.3275(1)	0.9884(2)	0.9300(2)	0.010(1)
Sb2/Ni	4*c*	0.44(2)/0.56(2)	0.5207(2)	1/4	0.5913(4)	0.007(1))

In analogy with the previous results for $Gd_5Ni_{0.96}Sb_{2.04}$, $Gd_5Ni_{0.71}Bi_{2.29}$[4] and $Y_5Ni_{0.38}Sb_{2.62}$[5], Ni was found to mix with Bi/Sb on the 4*c* site yielding the $Dy_5Ni_{0.66(1)}Bi_{2.34(1)}$ and $Lu_5Ni_{0.56(2)}Sb_{2.44(2)}$ compositions. X-ray powder diffraction patterns were collected on a PANalytical diffractometer with the $CuK\alpha_1$ radiation. More details on the crystal structures are available from the Fachinformationszentrum Karlsruhe, 76344 Eggenstein-Leopoldshafen, Germany (fax: +49 7247 808 666; e-mail: crysdata@fiz-karlsruhe.de) on quoting the depository CSD number 420519 for $Dy_5Ni_{0.66}Bi_{2.34}$ compound and 420520 for $Lu_5Ni_{0.56}Sb_{2.44}$ one and also from the Supporting information.

7.2.3.2 Magnetic measurements

Magnetization in a field-cooled (FC) mode for the polycrystalline $Dy_5Ni_{0.66}Bi_{2.34}$ sample annealed at 1350 °C and 800 °C was measured on a Quantum Design SQUID magnetometer at 100 Oe field between 320 and 2 K (Fig. 7.2.2, on the left, data for the sample annealed at 800 °C are shown). Magnetocaloric effect for $Dy_5Ni_{0.66}Bi_{2.34}$ in terms of magnetic entropy change was derived from the magnetization vs. field (*M* vs. *H*) curves measured around the ordering temperature with 5 K increments. The magnetic field changed from 0 to 50 kOe in 2 kOe steps. The entropy change (Fig. 7.2.2, on the right) was calculated using the following numerical integration:

$$\Delta S(T)_{\Delta H} = \sum_i \frac{M_i - M_{i+1}}{T_{i+1} - T_i} \delta H \qquad (8.1)$$

where δH is a magnetic field step and M_i and M_{i+1} are the values of magnetization at temperatures T_i and T_{i+1}, respectively.

7.2.4 Results and discussion

7.2.4.1 Structures of $Dy_5Ni_{0.66}Bi_{2.34}$ and $Lu_5Ni_{0.56}Sb_{2.44}$

The $Dy_5Ni_{0.66}Bi_{2.34}$ and $Lu_5Ni_{0.56}Sb_{2.44}$ compounds are isostructural to the orthorhombic Yb_5Sb_3-type structure (Tables 7.2.1 and 7.2.2). The structure of $Dy_5Ni_{0.66}Bi_{2.34}$ is shown in Fig. 7.2.1. It consists of trigonal and hexagonal channels of Dy atoms propagating along the b direction. While trigonal channels are filled with Bi atoms only, larger hexagonal ones accommodate both Dy and Bi/Ni atoms.

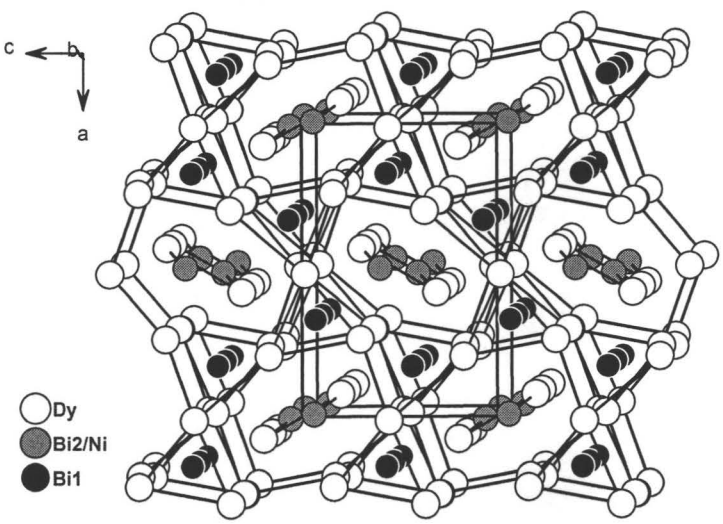

Figure 7.2.1. Structure of the $Dy_5Ni_{0.66}Bi_{2.34}$ phase

Since the refined compositions are Ni poorer than the loading compositions, it can be stated that the $Dy_5Ni_{0.66(1)}Bi_{2.34(1)}$ and $Lu_5Ni_{0.56(2)}Sb_{2.44(2)}$ formulas represent maximum possible Ni contents achievable under the employed synthesis conditions. As was shown

for the $Y_5Ni_xSb_{3-x}$ phase,[5] introduction of Ni reduces the strength of the Y–Sb interactions and this dictates the maximum possible degree of substitution. At the same time entropy contribution associated with the Sb/Ni solution lowers the total Gibbs free energy and favors the substitution in the limited concentration range. This argument can be also applied to the $Dy_5Ni_{0.66}Bi_{2.34}$ and $Lu_5Ni_{0.56}Sb_{2.44}$ compounds.

7.2.4.2 Magnetic properties and magnetocaloric effect of $Dy_5Ni_{0.66}Bi_{2.34}$

Polycrystalline $Dy_5Ni_{0.66}Bi_{2.34}$ annealed at 1350 °C for 1.5 h showed a ferromagnetic step-like transition around 66 K. A step-like feature can be indicative of a compositional and structural inhomogeneity of the sample. Therefore additional magnetization measurements under the same conditions were performed on the $Dy_5Ni_{0.66}Bi_{2.34}$ sample annealed at 800 °C for 2 weeks. The magnetization curve (Fig. 7.2.2, on the left) was analogous to the one obtained for $Dy_5Ni_{0.66}Bi_{2.34}$ annealed at 1350 °C.

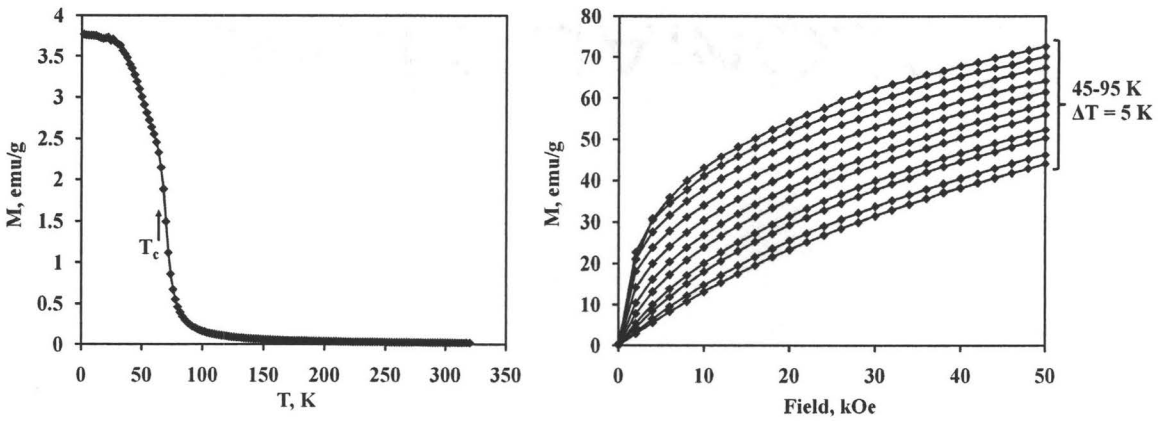

Figure 7.2.2. Magnetization as a function of temperature (on the left) and of field (on the right) for $Dy_5Ni_{0.66}Bi_{2.34}$

Presence of the step-like feature after the additional temperature treatment points to the intrinsic nature of this behavior. While indirectly, the compositional homogeneity of the sample established from the X-ray powder diffraction also supports the intrinsic nature of the magnetic ordering. This step-like transition may stem from spin reorientation or gradual ordering of magnetic moments on different Dy sites. In the future, we plan to perform a neutron diffraction experiment on the $Dy_5Ni_{0.66}Bi_{2.34}$ sample to establish the nature of this transition. Since routine neutron diffraction studies on bulk Dy-containing samples cannot be performed because of the large Dy absorption cross section of 994 (13) b (1 b = 10^{-24} cm^2, value for the 2200 m/s neutrons),[9] special sample mounting and collection procedures will be employed as described in Ref. 10.

A magnetic moment per Dy atom extracted from the Curie–Weiss fit in the paramagnetic region equals to $\mu_{eff/Dy}$ = 10.73 μ_B which is close to the theoretical value of 10.50 μ_B for a free Dy^{3+} ion. A positive value of a Weiss temperature θ = 67.8 K indicates a ferromagnetic nature of interactions between the magnetic moments.

The step-like feature of the ferromagnetic transition leads to a non-uniform separation between the magnetization curves during the saturation measurements (Fig. 7.2.2, on the right) and scattered values of the magnetic entropy change, ΔS, around the Curie temperature (Fig. 7.2.3). ΔS reaches the maximum value of -3.73 J/kg K at 75 K, which is indicative of the conventional MCE in the $Dy_5Ni_{0.66}Bi_{2.34}$ phase.

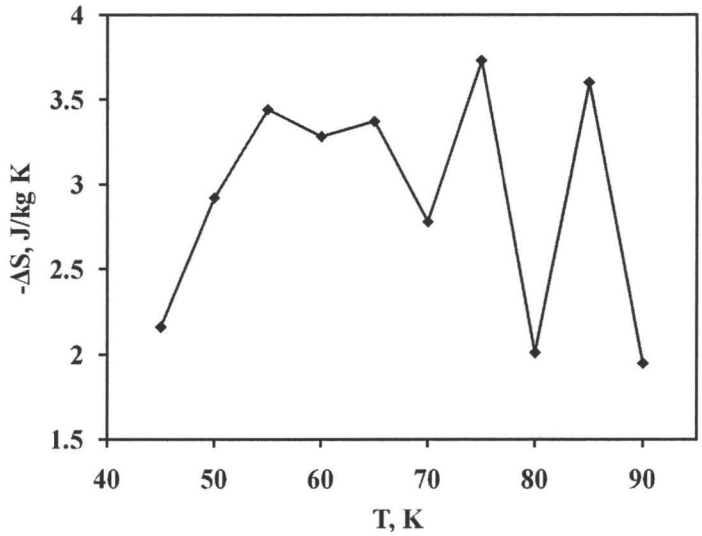

Figure 7.2.3. Magnetic entropy change for $Dy_5Ni_{0.66}Bi_{2.34}$ as a function of temperature for ΔH = 0–50 kOe

7.2.5 Conclusions

The $Dy_5Ni_{0.66}Bi_{2.34}$ and $Lu_5Ni_{0.56}Sb_{2.44}$ phases were found to adopt orthorhombic Yb_5Sb_3-type structure. $Dy_5Ni_{0.66}Bi_{2.34}$ shows a step-like ferromagnetic transition around 66 K and exhibits the magnetic entropy change, ΔS, of -3.73 J/kg K at 75 K. The small value of ΔS points to the presence of the conventional MCE in this phase.

7.2.6 Appendix. Supplementary data

Supplementary data associated with this article can be found in the online version, at doi:10.1016/j.solidstatesciences.2009.05.020.

References

[1] V. K. Pecharsky, K. A. Gschneidner Jr., *Phys. Rev. Lett.* **1997**, *78*, 4494.

[2] W. Choe, V. K. Pecharsky, A. O. Pecharsky, K. A. Gschneidner Jr., V. G. Young Jr., G. J. Miller, *Phys. Rev. Lett.* **2000**, *84*, 4617.

[3] M. -K. Han, G. J. Miller, *Inorg. Chem.* **2008**, *47*, 515.

[4] V. Svitlyk, F. Fei, Y. Mozharivskyj, *J. Solid State Chem.* **2008**, *181*, 1080.

[5] Y. Mozharivskyj, H. F. Franzen, *J. Alloys Compd.* **2001**, *319*, 100.

[6] A. V. Morozkin, R. Nirmala, S. K. Malik, *J. Alloys Compd.* **2005**, *394*, L9.

[7] *Stoe & Cie GmbH*, Darmstadt, Germany, **2004**.

[8] G. M. Sheldrick, *SHELXL97 and SHELXS97*, University of Gottingen, Germany, **1997**.

[9] *Neutron News* **1992**, *3*, 29.

[10] D. H. Ryan, L. M. D. Cranswick, *J. Appl. Crystallogr.* **2008**, *41*, 198.

Chapter 8. Supporting information

8.1 $Gd_5Si_{4-x}Bi_x$ structures: novel slab sequences achieved by turning off the directionality of nearest-slab interactions

Volodymyr Svitlyk,[a] Branton J. Campbell,[b] and Yurij Mozharivskyj[a]

[a]*Department of Chemistry, McMaster University, Hamilton, ON, L8S 4M1, Canada*

[b]*Department of Physics and Astronomy, Brigham Young University, Provo, Utah 84602*

8.1.1 Residual electron density

The diffuse streaks along $\boldsymbol{c}^*$ (or $\boldsymbol{a}^*$ for x = 1.5) are evidence of stacking-fault disorder, which was most severe at x = 2.5 and initially caused problems with the refinement. This is because, even when using the correct $P4_2bc$ symmetry, stacking disorder modifies the intensities along the diffuse $h + k = 2n + 1$ lines of reciprocal space. The (½, ½, 0) fault vector [or (0, ½, ½) for x = 1.5] lies within the plane of the $\propto^2[RE_5T_4]$ slabs, so that a stacking fault interrupts the slab stacking sequence, effectively replacing every A slab with a C slab and every B slab with a D slab on one side of the fault, and vise versa.

During the refinement, the fault-shifted structure manifested itself as a small residual electron density at fault-shifted Gd positions within the 3^2434 net (Figure 8.1.1), and to a lesser extent, at fault-shifted T-atom positions within the center-plane of the slab. Because the scattering power of a Gd atom is larger than that of an intraslab T atom, only

the residual electron density associated with fault-shifted Gd was observed at low fault-defect concentrations (e.g. for $x = 1.5$ and 2.0).

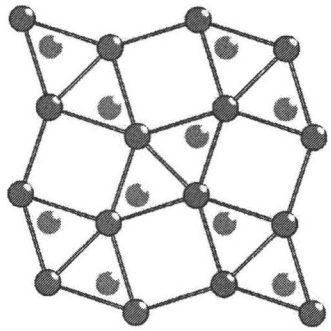

Figure 8.1.1. Presence of additional electron density (gray circles) in the Gd1 3^2434 net of the crystals with $x = 1.5$, 2.0 and 2.5

Note that a sufficiently high defect concentration would eventually broaden and diminish the Bragg reflections along the $h + k = 2n + 1$ lines to the point that they could no longer be viewed as peaks. Because this was clearly not the case in the samples studied here, we were still able integrate the diffuse peaks and refine an approximate stacking-fault model in which a fault-shifted copy of the entire structure was superimposed on top of the unshifted structure, so that the relative occupancies of the two copies were r and $1-r$, respectively. Thus, the extra electron density was treated using split sites, which are designated with a * in Tables 8.1.1 and 8.1.2.

8.1.2 Refinement of the structures with $x = 1.5$ (*Cmca*) and $x = 2.0$ ($I4_1/acd$)

The relationship between the atomic parameters of the unshifted atoms and the fault-shifted atoms (i.e. split positions) is given by the faulting vector (½, ½, 0) for $x = 2.0$

and (0, ½, ½) for x = 1.5. Only the Gd1 atoms of the fault-shifted structure could be reliably located on the residual electron density map. The residual density at the fault-shifted T2 position was small enough to be neglected. The Gd2 and T1 sites don't need fault-shifted partners because the space-group symmetry already places symmetry-equivalent atoms at their fault-shifted positions. Introduction of the fault-shifted Gd atoms into the structure significantly reduced the R values and yielded smoother residual electron density maps. E.g. without the fault-shifted Gd1 atoms, R_1 = 6.41% (vs. 4.56 %) and a residual density peak of 14.18 e/Å^3 (at 1.80 Å from Gd1) are obtained for x = 1.5, while R_1 = 4.99 % (vs. 4.52 %) and a peak of 4.88 e/Å^3 (at 1.91 Å from Gd1) present are for x = 2.0.

During the refinement the following constrains were used both for x = 1.5 and 2.0:

1) for the Gd1 atoms, the unshifted and fault-shifted occupancies were constrained to sum to 1;

2) the fault-shifted temperature factors were constrained to be equal to the unshifted temperature factors;

3) the fault-shifted coordinates (x^*, y^*, z^*) were constrained to follow the unshifted coordinates (x, y, z) as follows: for x = 1.5 (*Cmca*), $x^* = x$, $y^* = y + ½$, $z^* = z + ½$, or $x^* = x$, $y^* = y$ and $z^* = -z$, since under the symmetry operations of *Cmca*, x^*, y^*, z^* transforms into x^*, $y^* = ½ + y^*$, $z^* = ½ - z^*$; for x = 2.0 ($I4_1/acd$), $x^* = x + ½$, $y^* = y + ½$, $z^* = z$, or $x^* = -x$, $y^* = y$ and $z^* = z$, since under the symmetry operations of $I4_1/acd$, x^*, y^*, z^* transforms into $x^* = ½ - x^*$, $y^* = ½ + y^*$, z^*.

Table 8.1.1. Atomic and isotropic temperature (U) parameters for the x = 1.5 and 2.0 single crystals

Atom	Site	Occupancy	x/a	y/b	z/c	U (Å^2)
			$Gd_5Si_{2.416(8)}Bi_{1.584(8)}$ (x = 1.5)			
Gd(1)	16*g*	0.941(2)	0.12840(6)	0.8295(1)	0.83011(1)	0.0177(2)
Gd(1)*	16*g*	0.059(2)	0.12840(6)	0.8295(1)	0.16989(9)	0.0177(2)
Gd(2)	4*b*	1	1/2	0	0	0.0120(4)
Bi/Si(1)	8*d*	0.792/0.206(4)	0.29187(8)	0	0	0.0125(4)
Si(2)	8*f*	1	0	0.8779(11)	0.1255(7)	0.014(2)
			$Gd_5Si_{1.93(1)}Bi_{2.07(1)}$ (x = 2)			
Gd(1)	32*g*	0.975(2)	0.3331(2)	0.9178(2)	0.06149(2)	0.0163(2)
Gd(1)*	32*g*	0.025(2)	0.6669(2)	0.9178(2)	0.06149(2)	0.0163(2)
Gd(2)	8*a*	1	0	1/4	3/8	0.0116(2)
Bi/Si(1)	16*d*	0.938/0.062(6)	0	1/4	0.97841(2)	0.0135(3)
Si/Bi(2)	16*f*	0.902/0.098(5)	0.3658(3)	x + 1/4	1/8	0.011(1)

* designates a split, fault-shifted site

8.1.3 Refinement of the $Gd_5Si_{1.5}Bi_{2.5}$ structure ($P4_2bc$ space group)

The $Gd_5Si_{1.5}Bi_{2.5}$ structure has the *ABADABAD* slab sequence, and the atoms in Table 8.1.2 are labeled according to slabs where possible. The $P4_2bc$ symmetry relates the first *A* slab and the *B* slab to the second *A* slab and the *D* slab. A stacking fault then substitutes *C* slabs for *A* slabs and reverses the *B* and *D* slabs. In agreement with this model, fault-shifted copies of the Gd atoms within the 3^2434 nets (Gd1A, Gd2A, Gd1B and Gd2B) and the *T* atoms within the trigonal prisms (Si/Bi5A and Si/Bi5B) were be readily identified in the residual electron density map. The other Gd and T sites (Gd3A, Gd3B, and Bi1-4) don't need fault-shifted partners because the space-group symmetry already places symmetry-equivalent atoms at their fault-shifted positions.

The fault-shifted atoms (labeled "C" and "D" in Table 8.1.2) were treated as split sites in the refinement. Originally, the positional parameters of split, fault-shifted structure were treated independently from those of the unshifted structure; but this approach lead to severe correlations among the atomic parameters, besides the refinement was unstable. And even if the fit had been stable, it would not be a straightforward matter to interpret differences between the internal structures of fault-shifted and unshifted slabs (possibly related to structural relaxation near a fault interface). Therefore, the positional parameters of the fault-shifted atoms were constrained to follow those of the unshifted structure by (½, ½, 0). The occupancies and temperature factors of fault-shifted atoms were handled just they were for the x = 1.5 and 2.0 structures. The chemical compositions of each of the slabs were also assumed to be identical. In summary, the following constraints were used.

1) the positional coordinates of the fault−shifted (*) and the unshifted structures were constrained according to $x^* = x + ½$, $y^* = y + ½$, $z^* = z$, or $x^* = x$, $y^* = -y$ and $z^* = z$, since under the symmetry operations of $P4_2bc$, x^*, y^*, z^* transforms into $x^* = ½ + x^*$, $y^* = ½ - y^*$, z^*;

2) the occupancies of each pair of fault-shifted and unshifted atoms (*A*/*C* or *B*/*D*) were constrained so as to sum to 1;

3) the occupancies of all fault-shifted atoms were constrained to have the same value (*r*);

4) the temperature factors of each pair of fault-shifted and unshifted atoms (*A*/*C* or *B*/*D*) were constrained to be equal;

5) the Si/Bi ratios were constrained to be the same in each slab;

6) additionally, we constrained z(Gd1A) = $-z$(Gd2A) in order to center the A slab around the cell origin.

Table 8.1.2. Atomic and isotropic temperature (U) parameters from the x = 2.5 single crystal

Atom	Site	Occupancy	*x/a*	*y/b*	*z/c*	U (Å^2)
			$Gd_5Si_{1.58(1)}Bi_{2.42(1)}$			
Gd(1A)	8*c*	0.916(2)	0.6754(8)	0.1615(8)	0.06388(8)	0.043(2)
Gd(1C)*	8*c*	0.084(2)	0.6754(8)	0.8385(8)	0.06388(8)	0.043(2)
Gd(2A)	8*c*	0.916(2)	0.6692(8)	0.1583(7)	0.93612(7)	0.046(2)
Gd(2C)*	8*c*	0.084(2)	0.6692(8)	0.8417(7)	0.93612(7)	0.046(2)
Gd(3A)	4*a*	1	0	0	09987(3)	0.034(2)
Gd(1B)	8*c*	0.916(2)	0.1693(7)	0.1699(7)	0.3137(2)	0.026(1)
Gd(1D)*	8*c*	0.084(2)	0.1693(7)	0.8301(7)	0.3137(2)	0.026(1)
Gd(2B)	8*c*	0.916(2)	0.1604(7)	0.1652(6)	0.1864(1)	0.026(1)
Gd(2D)*	8*c*	0.084(2)	0.1604(7)	0.8348(6)	0.1864(1)	0.026(1)
Gd(3B)	4*a*	1	0	1/2	0.2478(3)	0.024(1)
Bi(1)	4*a*	1	0	0	0.1033(2)	0.033(2)
Bi(2)	4*a*	1	0	0	0.8965(2)	0.035(2)
Bi(3)	4*b*	1	0	1/2	0.3511(2)	0.039(2)
Bi(4)	4*b*	1	0	1/2	0.1459(2)	0.024(1)
Si/Bi(5A)	8*c*	0.722/0.193(5))	0.6409(17)	0.8666(17)	0.9974(6)	0.037(3)
Si/Bi(5C)*	8*c*	0.0667/0.0178(4)	0.6409(17)	0.1334(17)	0.9974(6)	0.037(3)
Si/Bi(5B)	8*c*	0.722/0.193(5)	0.1422(12)	0.8647(11)	0.2470(5)	0.025(2)
Si/Bi(5D)*	8*c*	0.0667/0.0178(4)	0.1422(12)	0.1353(11)	0.2470(5)	0.025(2)

8.1.4 Faulting probability

The residual electron density (r) that we refined as a low-occupancy fault-shifted copy of the structure should not be interpreted as the fraction of fault-shifted material, however unintuitive this may seem. Because the stacking faults are randomly placed

within the crystal, and each slab has one of two possible in-plane positions (A vs C or B vs D), there will be nearly equal amounts of shifted and unshifted material, so that it becomes irrelevant which position we refer to as "faulted". The refined r parameter should instead be interpreted as the average fraction of minority material (either fault-shifted or unshifted) within a volume that spans one X-ray coherence length. Depending on the crystal volume sampled by a given X-ray photon, the local minority fraction could be anywhere between zero and the 50% upper limit. But on average, it will have the value that we call r. The refined values of the minority fraction (see Table 5.1 of the manuscript) were r = 0.059, 0.025 and 0.084 for the respective x = 1.5, 2.0 and 2.5 samples. In the limit of low defect concentration, it is easy to show that $r \approx 0.25\ p$, where p is the average number of fault defects per coherence length. We then estimate that p = 0.24, 0.10 and 0.34 for the respective x = 1.5, 2.0 and 2.5 samples.

The faulting probability, α, is related to p according to $\alpha \approx (s/c)p$, where $s \approx 7.7$ Å is the interslab spacing (i.e the distance between the centers of two adjacent slabs), can also be determined if the X-ray coherence length (c) is known. Though the coherence properties of the instrument used have not been characterized, we note that a typical laboratory-diffractometer coherence length of 1000 Å would yield α = 0.18%, 0.077% and 0.26% for the respective x = 1.5, 2.0 and 2.5 samples.

8.2 Structural, magnetic and magnetocaloric properties of the $Gd_5Si_{4-x}Sb_x$ (x = 0.5-3.5) phases

Volodymyr Svitlyk, Yan Yin Janice Cheung and Yurij Mozharivskyj

Department of Chemistry, McMaster University, Hamilton, ON, L8S 4M1, Canada

8.2.1 Refinement of the fault shifted structures

The diffuse scattering along $\boldsymbol{a}^*$ for $Gd_5Si_2Sb_2$ and $Gd_5Si_{1.5}Sb_{2.5}$ resulted from the stacking-fault disorder. During the refinement, the fault-shifted structure appeared as a residual electron density at fault-shifted Gd positions. This extra electron density was treated as split sites and the following constrains were used for $Gd_5Si_2Sb_2$ and $Gd_5Si_{1.5}Sb_{2.5}$ during the refinement:

1) for the Gd2 atoms, the sum of unshifted and fault-shifted occupancies were constrained to 1;

2) the fault-shifted temperature factors were constrained to be equal to the unshifted temperature factors;

3) the fault-shifted coordinates (x^*, y^*, z^*) were constrained to follow the unshifted coordinates (x, y, z) as follows: $x^* = x$, $y^* = y + ½$, $z^* = z + ½$, or $x^* = x$, $y^* = y$ and $z^* = -z$, since under the symmetry operations of *Cmca*, x^*, y^*, z^* transforms into x^*, $y^* = ½ + y^*$, $z^* = ½ - z^*$;

Table 8.2.1. Atomic and isotropic temperature (U) parameters for $Gd_5Si_{1.73}Sb_{2.27}$ and $Gd_5Si_{1.72}Sb_{2.28}$ from single crystal diffraction data

Atom	Site	Occupancy	x/a	y/b	z/c	U (Å^2)
$Gd_5Si_{1.73}Sb_{2.27}$ (Eu_5As_4-type)						
Gd1	4*a*	1	0	0	0	0.018(1)
Gd2	16*g*	0.87(1)	0.1308(1)	0.1683(1)	0.3323(1)	0.023(1)
Gd21	16*g*	0.13(1)	0.1308(1)	0.1683(1)	0.6678 (1)	0.023(1)
Sb/Si1	8*d*	0.96/0.04(1)	0.2053(1)	0	0	0.020(1)
Si/Sb2	8*f*	0.83/0.17(1)	0	0.3663(4)	0.1327(4)	0.018(1)
$Gd_5Si_{1.72}Sb_{2.28}$ (Eu_5As_4-type)						
Gd1	4*a*	1	0	0	0	0.032(1)
Gd2	16*g*	0.86(2)	0.1312(1)	0.1678(2)	0.3326(2)	0.038(1)
Gd21	16*g*	0.14(2)	0.1312(1)	0.1678(2)	0.6674 (2)	0.038(1)
Sb/Si1	8*d*	0.95/0.05(2)	0.2050(2)	0	0	0.033(1)
Si/Sb2	8*f*	0.81/0.19(2)	0	0.3648(8)	0.1332(7)	0.030(2)

8.2.2 Faulting probability

The refined values of the minority fraction (see Table 6.2 of the manuscript) were $r = 0.13$ and 0.14 for the $x = 2.0$ and 2.5 samples. In the limit of low fault concentration, the minority fraction, r, is related to the average number, p, of fault defects per coherence length through $r \approx 0.25\ p$. We then estimate that $p = 0.52$, and 0.56 for the respective $x =$ 2.0 and 2.5 samples.

The faulting probability, α, is related to p according to $\alpha \approx (s/c)p$, where $s \approx 7.6$ Å is the interslab spacing (i.e the distance between the centers of two adjacent slabs), and it can be determined if the X-ray coherence length (c) is known. Though the coherence properties of the instrument used have not been characterized, we note that a typical laboratory-diffractometer coherence length of 1000 Å would yield $\alpha = 0.40\%$ and 0.43% for the respective $x = 2.0$ and 2.5 samples.

The Gd-Gd distances as a function of Sb concentration

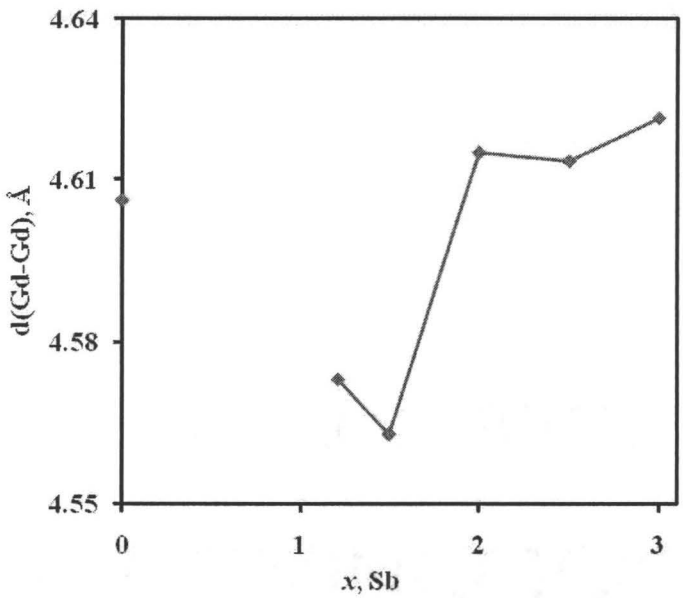

Figure 8.2.1. The average intraslab Gd-Gd distances between the $_{\infty}^{2}[Gd_5T_4]$ slabs as a function of the Sb content

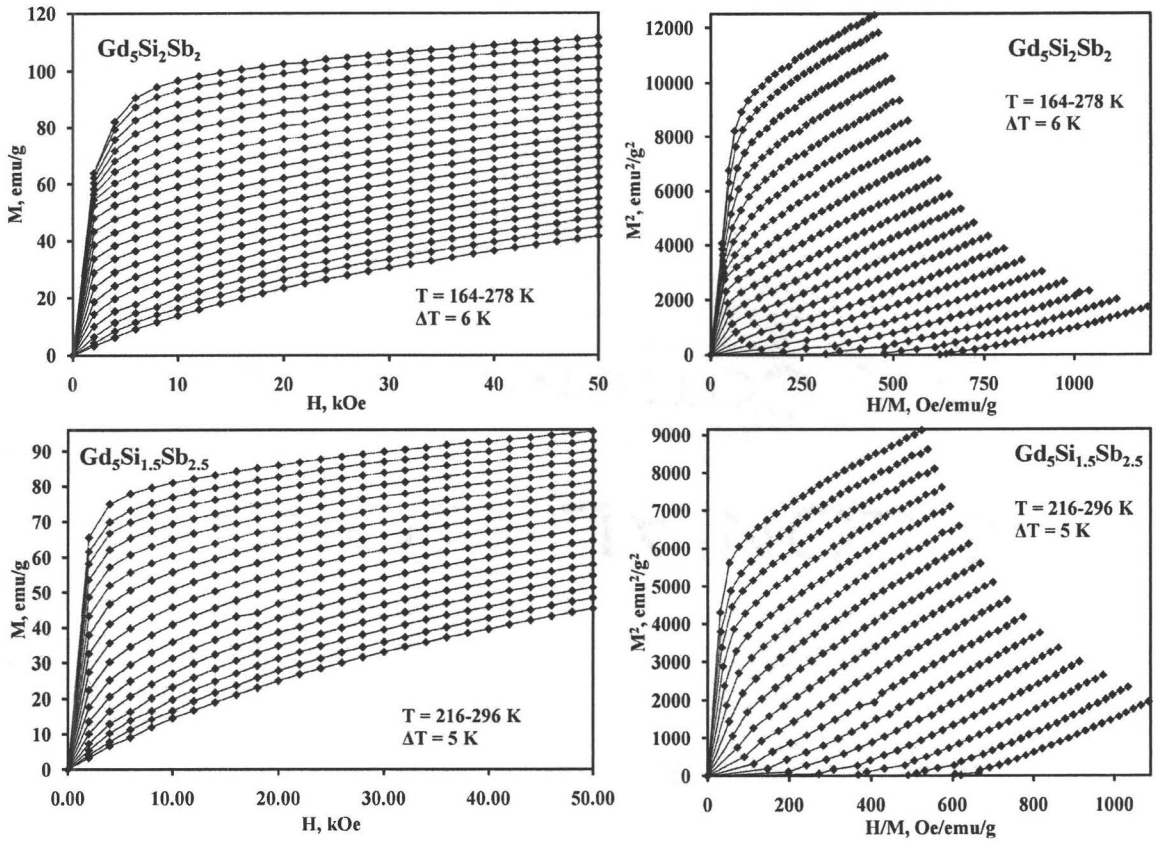

Figure 8.2.2. Saturation magnetization (left) and corresponding Arrott plot (right) for the $Gd_5Si_2Sb_2$ and $Gd_5Si_{1.5}Sb_{2.5}$ samples

Chapter 9. Conclusions

9.1 Development of the Gd_5T_4 phases

The RE_5T_4 (RE – rare-earth element, T – p-element) phases are known for their close relationship between the valence electron count, size effect, structure and physical properties. It has been shown that the broken interslab Ge-Ge dimers in the Gd_5Ge_4 phase can be reformed by substitution of Ge by Ga,[1] which has one less valence electron. The origin of this structural transition is an enhancement of the Ge-Ge interactions through depopulation of the antibonding levels within the Ge-Ge bonds.

For the first time we have shown that the Si-Si interslab dimers in the Gd_5Si_4 phase can be broken by an increase in the valence electron count. Substitution of Si in Gd_5Si_4 with size-equivalent but electron-richer P destabilizes and breaks the T-T bonds ($d_{Si\text{-}Si}$ = 2.49 Å) in $Gd_5Si_{2.75}P_{1.25}$ (Sm_5Ge_4-type, $d_{Si/P\text{-}Si/P}$ = 3.74 Å) due to the population of their antibonding levels.[2] Cleavage of the T-T bonds in the Gd_5Si_4-type phase is abrupt, the dimers break at the critical P content of 1.25/f.u. when the T-T bonding is no longer energetically favourable.

The motivation behind these targeted structural changes, despite the purely scientific interest, is to achieve a first-order temperature-dependant structural transition in new phases. If during cooling the broken Si/P-Si/P dimers were to reform and this structural transition was to be accompanied by a ferromagnetic ordering, this could yield a first-order coupled magnetostructural transition. As was discussed previously, a first-order coupled magneto-structural transition is at the origin of the giant MCE. Although

$Gd_5Si_{2.75}P_{1.25}$ orders ferromagnetically at 184 K, it does not undergo a structural transformation, and thus only a conventional MCE with the ΔS_{mag} value of -7.8 J/Kg K at 177 K is observed.[3] The absence of the structural transition was confirmed by low-temperature single crystal X-ray diffraction studies.

It can be speculated, whether a possible temperature-dependant reformation of the broken Si/P-Si/P dimers in $Gd_5Si_{2.75}P_{1.25}$ is hindered by impurities, which stabilize the Sm_5Ge_4-type structure. This phenomenon was observed in the giant magnetocaloric material $Gd_5Si_2Ge_2$[4] prepared from the commercial grade Gd metal, however it is not expected to exhibit itself in the studied $Gd_5Si_{4-x}P_x$ system due to the high purity of the initial elements (section 3.3.1). The absence of a temperature-dependant structural transition is likely due to the thermodynamic stability of the Sm_5Ge_4-type $Gd_5Si_{2.75}P_{1.25}$ structure throughout the studied temperature range.

In addition to the purely electronic mechanism, the size effect can be used for structural alterations in the RE_5T_4 systems. The method of breaking the interslab *T-T* dimers using the size effect was originally demonstrated in the $Gd_5Si_{4-x}Sn_x$ system,[5] where the dimers were gradually stretched and eventually broken due to the introduction of larger Sn atoms. Both valence electron count and sizes effects were employed to cleave the interslab dimers in the $Gd_5Si_{4-x}Bi_x$[6] and $Gd_5Si_{4-x}Sb_x$[7] systems. Incorporation of large Bi completely disrupted the interslab *T-T* bonding and resulted in slab stacking sequences never observed before in the RE_5T_4 systems. Additionally, uniformity of the *T-T* bonds caused severe stacking faults accompanied by diffuse scattering.

Incorporation of Sb atoms yielded a less diverse structural behaviour in the $Gd_5Si_{4-x}Sb_x$ system and a larger Gd_5Si_4-type homogeneity region. This is expected as Sb is smaller than Bi and this results in more gradual structural changes upon the substitution of Sb for Si. All phases in the $Gd_5Si_{4-x}Sb_x$ system undergo ferromagnetic transitions in a wide temperature range, including room temperature. However, magnetic orderings in the $Gd_5Si_{4-x}Sb_x$ system are not accompanied by reformations of the interslab dimers, and thus only the conventional magnetocaloric effect is observed. We believe that the broken dimers in the $Gd_5Si_{4-x}Sb_x$ phases do not reform upon cooling due to the thermodynamic stability of the corresponding phases, similarly to the $Gd_5Si_{4-x}P_x$ system.

9.2 Ni-substituted RE_5T_3 phases

The $RE_5Ni_xT_{3-x}$ phases with RE = Gd, Dy, Lu, T = Sb, Bi[8,9] represent an exploratory part of the research. Here, structural and physical properties of the parent RE_5T_3 phases were altered through the incorporation of Ni. At 800 °C, the Gd_5Sb_3 and Gd_5Bi_3 binaries adopt a hexagonal Mn_5Si_3-type structure. Limited substitution of Ni for Sb and Bi resulted in the stabilization of the orthorhombic Yb_5Sb_3-type structures at 800 °C due to the entropy contribution from the Ni/(Sb,Bi) mixtures. Structural diversity in the homologous series of phases is desired, since it can lead to polymorphous structural transformations in the system. Although the Yb_5Sb_3- and Mn_5Si_3-type structures are quite different and are not expected to easily transform into each other, the presence of intermediate structures is possible. Ferromagnetic $Gd_5Ni_{0.96}Sb_{2.04}$, $Gd_5Ni_{0.71}Bi_{2.29}$ and

$Dy_5Ni_{0.66}Bi_{2.34}$ exhibit the conventional magnetocaloric effects around their ordering temperatures which implies absence of coupled magneto-structural transitions.

The studied Gd_5T_4 and $RE_5Ni_xT_{3-x}$ phases provide important fundamental knowledge which will facilitate further development and design of the magnetocaloric phases.

References

[1] Y. Mozharivskyj, W. Choe, A. O. Pecharsky, G. J. Miller, *J. Am. Chem. Soc.* **2003,** *125*, 15183-15190.

[2] V. Svitlyk, G. J. Miller, Y. Mozharivskyj, *J. Am. Chem. Soc.* **2009**, *131*, 2367-2374.

[3] V. Svitlyk, Y. Mozharivskyj, *Solid State Sci.* **2009**, *11*, 1941-1944.

[4] K. A. Gschneidner Jr., V. K. Pecharsky, *J. Appl. Phys.* **1999**, *85*, 5365-5368.

[5] Y. Mozharivskyj, A. O. Tsokol, G. J. Miller, *Z. Kristallogr.* **2006**, *221*, 493-501.

[6] V. Svitlyk, B. J. Campbell, Y. Mozharivskyj, *Inorg. Chem.* **2009**, *48*, 10364-10370.

[7] V. Svitlyk, Y. Y. J. Cheung, Y. Mozharivskyj, *J. Magn. Magn. Mater.* **2010**.

[8] V. Svitlyk, F. Fei, Y. Mozharivskyj, *J. Solid State Chem.* **2008**, *181*, 1080-1086.

[9] V. Svitlyk, F. Fei, Y. Mozharivskyj, *Solid State Sci.* **2009**, *11*, 1700-1702.